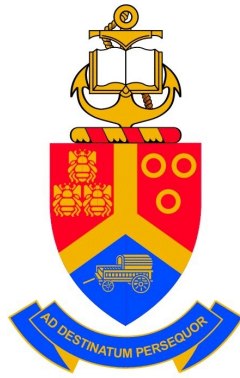


Van der Waals density functional studies of hydrogenated and lithiated bilayer graphene



by
Refilwe Edwin Mapasha

Submitted in partial fulfilment of the requirements
for the degree
Philosophiæ Doctor (PhD) in Physics
in the Faculty of Natural and Agricultural Sciences
University of Pretoria

Supervisor: Prof. Nithaya Chetty

February 20, 2014

UNIVERSITY OF PRETORIA

DECLARATION OF ORIGINALITY

This document must be signed and submitted with every essay, report, project, assignment, dissertation and/or thesis.

Full names of student: REFILWE EDWIN MAPASHA

Student number: s29685712

Personnel number: p04408705

Declaration

1. I understand what plagiarism is and am aware of the University's policy in this regard.
2. I declare that this thesis is my own original work. Where other people's work has been used (either from a printed source, Internet or any other source), this has been properly acknowledged and referenced in accordance with departmental requirements.
3. I have not used work previously produced by another student or any other person to hand in as my own.
4. I have not allowed, and will not allow, anyone to copy my work with the intention of passing it off as his or her own.

SIGNATURE STUDENT:.....

SIGNATURE SUPERVISOR:.....

SIGNATURE HEAD OF DEPARTMENT:.....

Summary

In this thesis, we use first principles density functional theory (DFT) to study the energetics, structural and electronic properties of hydrogenated and lithiated bilayer graphene material systems. The newly developed four variants of the non-local van der Waals (vdW) exchange-correlation functionals (vdW-DF, vdW-DF2, vdW-DF C09_x and vdW-DF2 C09_x) are employed to explore all the possible configurations of hydrogen adsorption at 50% and 100% coverage on a 1×1 unit cell. The results obtained are also compared with the GGA PBE functional.

For 50% hydrogen coverage, 16 unique configurations are identified in the unrelaxed state. Formation energy analysis reveals six possible energetically favourable configurations with three low-energy competing configurations. It is found that the properties of hydrogenated bilayer graphene greatly depend on the hydrogen configuration. For instance, the formation of a hydrogen dimer within the layers decouples the structure, whereas the dimer formation outside surfaces does not have a significant influence on the van der Waals forces; thus the bilayers remain coupled. In this coupled configuration, the vdW-DF C09_x functional predicts the lowest formation energy and shortest interlayer separation, whereas the GGA PBE functional gives the highest formation energy and largest interlayer distance. The reasons behind the variation of these functionals are discussed. Two of the three low-energy competing configurations exhibit semimetallic behaviour, whereas the remaining configuration is a wide band gap material. The wide band gap structure is found to undergo a hydrogen-induced spontaneous phase transformation from hexagonal to tetrahedral (diamond-like) geometry. We conclude that this wide band gap configuration represents a viable template for synthesizing nanodiamonds from graphene by hydrogenation. At 100% coverage, ten unique hydrogen configurations are identified from a 1×1 unit cell. All exchange-correlation functionals predict nine of the structures to have negative formation energies. From these nine structures, three low-energy competing structures are noted and found to

be wide band gap semiconductors, whereas the other configurations exhibit either a semimetallic or metallic character. Although a 1×1 unit-cell is able to present a clear picture for the interaction between hydrogen and graphene, our results reveal that it limits the occurrence of other interesting physics. The cell size was increased to 2×1 , to identify other low-energy configurations that are not possible in a 1×1 cell. The identified configurations have shown physically interesting hydrogen arrangements such as chair-like, zigzag-like and boat-like configurations. Furthermore, our results reveal that hydrogenation reduces the elastic properties of the pristine structures.

We further perform a systematic investigation of the effects of lithium (Li) on *AA* and *AB* stacking sequences of bilayer graphene. Two Li atoms are considered to examine the effects of the Li-Li interaction on bilayer graphene, and a total of 12 unique configurations for *AB* and 9 for *AA* stackings are identified. The vdW-DF consistently predicts the highest formation energies, whereas vdW-DF2 C09_x gives the lowest. Unlike in the case of the pristine structures, it is noted that for lithiated bilayer graphene, GGA PBE gives comparable results to the other functionals. One of the Li intercalated configurations undergoes a spontaneous translation from the *AB* to *AA* stacking, and is found to be the most energetically stable configuration. We therefore conclude that Li favours the *AA* stacking, and that configuration represents a feasible template for experimentally synthesizing and characterizing a Li-based anode material. We noticed that all identified Li configurations exhibit metallic behaviour. Lastly, we found that the intercalated Li dimer weakly interacts with the graphene layers, whereas the intercalated isolated Li atom exhibits strong interaction.

Dedication

This is dedicated to the whole family of Balaudzi and to my late grandmother Mankwana. To my mom and dad, this is for the love and support you have given me for the years of my studies.

Acknowledgements

I would like to acknowledge my supervisor Prof Nithaya Chetty for initiating this project, and unfailing support, guidance, discussion and encouragement throughout it. I would also like to acknowledge Prof Chris Theron for offering me a part-time lecturing position in the physics department. I am extremely grateful to the National Research Foundation (NRF) and University of Pretoria for financial assistance.

I would like to thank all members of the computational and solid state research group at the University of Pretoria for support, and particularly my collaborators Dr Richard Andrew and Dr Mahlaga Molepo for their fruitful, constructive, discussions.

I would like to thank all the family of Balaudzi ba Mapata a Senaba, especially my uncle Mohleiwana Mapasha for his academic and moral support throughout my studies. In particular, many thanks to my parents Mokadikwa and Mulambilu Mapasha for their financial support and patience throughout my studies. I would be punished if I didn't thank the Almighty God for protection.

Contents

List of Figures	iv
List of Tables	v
1 Introduction	1
1.1 Rationale	1
1.2 Objectives	9
1.3 Synopsis	11
Bibliography	12
2 Review of previous work	20
2.1 Adsorption of hydrogen on bilayer graphene	20
2.2 Adsorption of lithium on bilayer graphene	24
Bibliography	28
3 Electronic structure methods	30
3.1 Introduction	30
3.2 Density Functional Theory	35
3.3 Kohn-Sham (KS) equations	39
3.4 Exchange Correlation Energy Functional	42

3.4.1	Local Density Approximation	43
3.4.2	Generalized Gradient Approximation	45
3.4.3	The origin of van der Waals forces and derivation of the London dispersion energy term	47
3.4.4	Approaches to incorporate van der Waals interactions into DFT	54
3.4.5	Derivation of the kernel $\Phi(\mathbf{r}, \mathbf{r}')$	57
3.5	Plane waves formulation of the Kohn-Sham equations	63
3.5.1	Bloch's theorem	64
3.5.2	Plane wave kinetic energy cut-off	65
3.5.3	k-point sampling	66
3.6	The atomic pseudopotential approximation	68
3.6.1	Requirements for pseudopotential construction	69
3.6.2	The projector augmented wave (PAW) PPS method	71
3.7	Tests of convergence	75
	Bibliography	77
4	<i>Ab initio</i> studies of hydrogen adatoms on bilayer graphene	83
5	Van der Waals density-functional study of 100% hydrogen coverage on bilayer graphene	98
6	Comparative investigations of lithium adatoms on AA and AB stackings of bilayer graphene : a van der Waals density functional study	113
7	Summary and general conclusions	129
7.1	Test of exchange-correlation functionals on bulk bilayer graphene and graphite	130
7.2	Hydrogen adatoms on bilayer graphene at 50% coverage	131

7.3	Van der Waals density-functional study of 100% hydrogen coverage on bilayer graphene	133
7.4	Comparative investigations of lithium adatoms on AA and AB stackings of bilayer graphene : a van der Waals density functional study	135

List of Figures

3.1	Schematic illustration of all-electron (solid lines) and pseudo electron (dashed lines) potentials and their corresponding wavefunctions. The radius at which all-electron and pseudo electron values match is designated r_{cut} . Taken from Ref. [10]	69
3.2	Total energy versus energy cutoff for bilayer graphene structure.	75
3.3	Plot of total energies variations with respect to Monkhorst Pack grid sizes ($k_x \times k_y \times k_z$) for bilayer graphene structure. Note that for two dimensional systems, grid sizes are defined as $k_x=k_y$ and $k_z=1$	76

List of Tables

1.1	Various properties for carbon allotropes (Specific surface area A in m^2 / g , charge carriers mobility v_s in $\text{cm}^2 / \text{V s}$, thermal conductivity κ in $\text{W} / \text{m K}$, Young 's modulus Y in TPa and electrical conductivity σ in S / m).	2
-----	--	---

Chapter 1

Introduction

In this introductory chapter, we give a brief review of selected properties and applications of graphene and bilayer graphene materials. The realization of these material systems is discussed by reviewing the various synthesizing techniques used. We also introduce newly developed *ab initio* exchange-correlation functionals that are able to correctly describe the properties of these layered systems. Lastly, the objectives of this project are presented.

1.1 Rationale

Carbon is the element that is largely responsible for human development. It is an interesting material because of its ability to have different forms of bonding [1, 2, 3, 4], and has been widely studied. It is abundant in the universe, and exists in different allotropes such as diamond, graphite, fullerenes (buckyballs), nanotubes and graphene. These allotropes have differing bond hybridization ranging from sp to sp^3 under ambient conditions, and possess vastly differing properties (see Table 1.1), with graphene having extraordinary ones. Graphene is a monolayer of graphite, a single layer of carbon atoms tightly packed into a two-dimensional hexagonal lattice [2, 3, 4, 5, 6, 7, 8, 9,

10]. Graphene research is a rapidly growing field in the condensed matter physics and materials science fields.

Self or free standing few layered graphene (FLG) which contains either one (graphene), two (bilayer graphene) or three (trilayer graphene) layers was first peeled from graphite in 2004 by Novoselov and co-workers at Manchester University [5, 6, 7, 8, 9, 10]. In 2010, these researchers were awarded the Nobel prize in physics *for groundbreaking experiments regarding the two dimensional material graphene* [11]. Their experiments demonstrated that graphene has extraordinary (unusual) properties such as charge carriers that behave as massless Dirac fermions at the corners of the Brillouin zone, the observed anomalous quantum Hall effect and ballistic transport at room temperature [5]. They also reported that FLG is thermodynamically stable under ambient conditions, and is of relatively high quality [5].

Table 1.1: Various properties for carbon allotropes (Specific surface area A in m^2 / g , charge carriers mobility v_s in $\text{cm}^2 / \text{V s}$, thermal conductivity κ in $\text{W} / \text{m K}$, Young 's modulus Y in TPa and electrical conductivity σ in S / m).

Allotropes	A	v_s	κ	Y	σ
Graphene	2630.00^a	2.00×10^{5d}	5.00×10^{3h}	1.00^l	$1.3 \times 10^{5p,q}$
Graphite	10.00^b	1.30×10^{4e}	3.00×10^{3i}	1.06^m	25×10^{5r}
Fullerene	5.00^c	0.56^f	3.00×10^{3j}	0.01^n	1.7×10^{-7s}
Carbon nanotube	1315.30^a	1.00×10^{5g}	0.50^k	0.64^o	1.7×10^{6t}

^aReference [12]; ^bReference [13]; ^cReference [14]; ^dReference [9]; ^eReference [15];
^fReference [16]; ^gReference [17]; ^hReference [18]; ⁱReference [19]; ^jReference [20];
^kReference [21]; ^lReference [22]; ^mReference [23]; ⁿReference [24]; ^oReference [25];
^pReference [26]; ^qReference [27]; ^rReference [28]; ^sReference [29]; ^tReference [30].

Table 1.1 compares some of these remarkable properties of graphene with other allotropes of carbon. These outstanding properties make graphene a good candidate for various technological applications such as electronic devices, bio-applications, sensor

applications as well as for energy storage [31, 32, 33]. For instance, high intrinsic mobility enables graphene to be used as a logical transistor [31].

The local network structure of graphene, just as in graphite, consists of sp^2 -hybridized carbon bonds [34]. In the plane of the hexagonal lattice, each carbon atom is bonded to the three nearest neighbours by strong σ -bonds [2, 3, 5, 6, 7, 34]. In addition, there is a weak π bond localized on each carbon atom, presenting possible degrees of unsaturation on the graphene structure. The electronic signatures of the π bands are uniquely characterized by continuous linear dispersions forming a cone-like shape exactly at the K -point. These arise from orbitals located near the K - and K' -points on the opposite corners of the Brillouin zone. Since the valence and conduction bands meet at the K -point, graphene exhibits a zero band gap [2, 3, 5, 6, 7, 34].

Bilayer graphene consists of two layers of graphene weakly bound by van der Waals forces. It has two stacking sequences viz. AA (simple) and AB (Bernal). The degree of van der Waals interactions in these two stackings is significantly different, resulting in differing interlayer spacings and binding energies. Reference [35] reported that the Bernal stacking has a shorter interlayer spacing and is more energetically favourable than simple stacking. Bilayer graphene possesses interesting electronic properties, which are slightly different from those of single-layer graphene. In contrast to graphene, electrons in bilayer graphene behave as massive chiral fermions [36, 37]. The linear dispersion relation observed around the K -point in a graphene monolayer becomes parabolic in bilayer graphene due to the massive electrons coupling between the layers [36, 37]. This suggests that bilayer graphene may be a viable candidate for tunable transistors, taking the advantage of this electronic coupling [38]. However, the valence and conduction bands also meet at the K -point of the Brillouin zone, making bilayer graphene semimetallic [36, 37, 38].

Numerous techniques are already being used and developed for synthesizing FLG materials. The most easily accessible and widely used methods are the mechanical ex-

foliation of graphite, chemical vapor deposition (CVD), unzipping of carbon nanotubes and epitaxial growth over silicon carbide (SiC) substrates. In the micromechanical ex-foliation of graphite, the free standing graphene is obtained by repeatedly attaching and removing scotch-tape over the graphite crystal (peeling method or scotch-tape method) [5]. These tiny-peeled crystals are usually characterized by using either transmission electron microscopy (TEM) or Raman spectroscopy to examine the imaging and other various properties. All the unusual properties proposed in reference [5] were observed in simply peeled-off graphene. Despite the high quality of ex-foliated graphene, its usage in numerous technological applications is too limited due to its relatively small size [26]. It is almost impossible to obtain a very large thin layer using the scotch-tape technique without causing damage (creating some defects); thus this method is not easily controllable. Although ex-foliated graphene does not meet market requirements, it is widely used in research for comparison with other developed methods [31].

In the CVD method, relatively large-area uniform polycrystalline graphene films are grown on top of metal foils or surfaces [39]. However, CVD is more expensive than using ex-foliation as a large energy source is required. In their review paper, Novoselov *et al.* [31] suggested that the size of graphene films synthesized using the CVD method meets commercial market requirements for a variety of applications. For instance, CVD graphene films are ready to be used in transparent conductive coating applications such as touch screens [31]. The first growth of a large-area graphene layer on top of Cu foils was reported in 2009 by Li *et al.* [26]. Thereafter, several studies have also reported the growth of FLG films on various types of metals [40, 41, 42].

Novoselov *et al.* [5] reported that two dimensional FLG systems stand a good chance of replacing the widely used silicon in the microelectronic technological applications. However, the zero band gap (semi-metallic nature) in the band structure hinders the direct application of these materials. To resolve this problem, researchers have made concerted efforts in trying to generate a band gap. Various methods such as cutting

graphene into nanoribbons [43, 44, 45], rotating carbon dimer at an angle of 90° creating Stone-Wales defects [46, 47, 48, 49, 50] and chemical functionalizations [51, 52, 53, 54, 55, 56, 3, 58, 59, 60, 10, 62, 63, 11, 65, 66] were explored. In addition, Ohta *et al.* [38] proposed that applying an electric field along the z direction between the layers in bilayer graphene could also open a notable band gap. Amongst all these possibilities, experiments [51, 52, 53, 54, 55, 56, 3] and first principles investigations [58, 59, 60, 10, 62, 63, 11, 65, 66] have shown that chemical functionalization yields a relatively large band gap.

As a preferred candidate for hydrocarbon compounds, hydrogen was the first element to be used as a dopant on graphene and produce a wide band gap [3, 66]. It was reported that it significantly modifies the local network bonding structure of graphene. There exists a wavefunction overlap between hydrogen $1s$ and carbon $2p$ orbitals. At 100% hydrogen coverage, the local graphene structure, known as graphane [66], is completely transformed from sp^2 to sp^3 hybridized carbon bonds. Lately, hydrogenation was applied to bilayer and trilayer graphene structures, and a wide band gap was also obtained [3, 10, 11, 2, 5, 6, 13]. Studies are not only focused just on band gap generation but also on the fundamental understanding of the role hydrogen plays in the energetics and the various bonds in these FLG structures. A fundamental theoretical study for these hydrogenated materials is necessary to supplement scarce experimental data, in particular for bilayer and trilayer graphene.

As well as opening a band gap, hydrogen can also be stored on graphene. Hydrogen is one of those elements that stores or carries energy just like ordinary electricity. The advantage of hydrogen compared to other elements is that it is the lightest, cleanest, and most abundant element in the universe [71]. The overwhelming interest in hydrogen is also due to the fact that hydrogen-stored-energy (fuel-cells) is capable of producing electricity that is sustainable, and can be used in electrical household equipment and in newly developed transportation technologies (electric cars) [71]. The use of fuel-cells

in cars is clean and efficient because no greenhouse gases such as carbon monoxide or carbon dioxide are produced, and will also alleviate society from the high cost of petroleum (gasoline). Research continues to flourish in exploring low cost novel materials that can store hydrogen. Several studies have proposed FLG (specifically graphene and bilayer graphene) as the best candidates [5], for these applications, due to their remarkable high surface area and electrical conductivity. Several experiments [2, 5, 6] reported that hydrogen can adsorb or desorb from graphene substrates at a remarkably low temperature. It is necessary to understand the effect of hydrogen on the material properties and which energetically stable configurations are possible in these FLG material systems.

It is important to note that not all elements generate a band gap, for instance lithium (Li): which is just below hydrogen on the periodic table, yields a metallic structure [16, 19, 74, 75, 76, 77, 17]. Although failing to open a band gap, Li still has an opportunity of being combined with FLG structures to form an interesting compound that could be useful for other technological applications.

The peculiar surface area for graphene shown in Table 1.1 also makes graphene a viable candidate as an anode material in the Li ion batteries (LIB). LIB are state-of-the-art sources of electrical power for electric equipment such as electric cars and portable electronic devices, i.e. watches and cellphones. Most industries use graphite material as an anode in the LIB due to its ability to intercalate and deintercalate Li-ions within the layers [79, 80, 81, 82, 83, 84, 85]. Recently, however, the performance of graphite as an anode has reached its limits. For instance it is not capable of being used in electric vehicles because of its relatively low Li-ion storage capacity [86].

Recently, several authors have demonstrated that graphene is suitable for use in LIB technologies, and has a Li-ion storage capacity of nearly twice that for graphite [86, 87, 88]. Graphite has a Li-ion storage capacity of about 372 mAhg^{-1} [89]. A high Li-ion storage capacity is necessary to allow a LIB to charge and discharge within a

small volume. Chan *et al.* [90] suggested that the reason for the high Li-ion storage in graphene might be due to its ability to adsorb Li-ions above and below the surface. Another research group demonstrated that bilayer graphene exhibits a greater Li-ion storage capacity than graphene [91]. This is because the novel bilayer graphene also has interlayer spacing that allows for Li-ions intercalation between the layers, which graphene lacks. The processes of charging and discharging in a LIB is easily controlled by the intercalation and de-intercalation mechanism of Li-ion. Studies are required to examine various possible Li configurations, in order to establish the lowest energy competing configurations in bilayer graphene materials. Another study has reported that the presence of Li-ions greatly affects the vdW interactions, resulting in the significant repulsion of the layers [16]. It was also proposed that bilayer graphene has the capability of improving recharge cyclic performance for LIB technology [91].

In theoretical studies, various properties of the FLG systems mentioned earlier are usually computed using quantum mechanical approaches. Density functional theory (DFT) [92] is a quantum mechanical modeling technique widely used by physicists, chemists and material scientists to understand the properties of various materials. Although DFT is an exact method in principle, for practical calculations, approximations are made for the exchange-correlation interactions [93, 94]. The most widely used approximations are the local density approximation (LDA) [93] and the generalized gradient approximation (GGA) [94]. The LDA performs relatively well for homogeneous systems (simple metals) and GGA is effective in the description of inhomogeneous systems (transition metals, surfaces, compound metals etc) [95, 96]. Owing to this, various accurate properties of monolayer graphene are obtained using either LDA or GGA functionals. However, as in graphite, these functionals fail to describe the known properties of bilayer graphene. This is due to their failure to describe the intrinsic non-local correlation effects (van der Waals interactions) found in these systems.

To resolve these issues, scientists have made significant efforts in developing new

exchange-correlation functionals that are capable of taking into account the long-range effects of van der Waals forces [98, 99, 100, 101, 102, 103, 104]. It was ensured that these functionals are accurately incorporated within the Kohn-Sham equations [97]. One such functional was developed by Dion *et al.* [98] in 2004 and is known as the van der Waals density functional (vdW-DF). The correlation energy part of this functional is divided into two parts viz., local and non-local (*nl*) correlation energies. The local energy correlation employs LDA to account for short range (homogeneous electron gas) interactions, whereas the non-local (*nl*) correlation energy is expressed as a simple approximation for the dielectric function. The exchange energy is taken from a GGA functional (PBE [94] or revPBE [105]). vdW-DF shows its efficiency in describing a wide range of systems without too much computational cost. Calculations for graphite indicate that vdW-DF correctly predicts the weak binding energy between layers but overestimates the interlayer distance when compared to experimental results. This overestimation is due to the repulsive nature of the revPBE exchange term.

In 2010, Klimes *et al.* [106] and Cooper [107] constructed a new exchange functional (C09_{*x*}) to replace the strongly repulsive revPBE exchange term. The resulting vdW-DF-C09_{*x*} functional shows an improvement in the calculated interlayer distance but an overestimation in the binding energy for graphitic systems, i.e. graphite and bilayer graphene [108]. During the same period, Lee *et al.* [109] improved the non-local correlation term of vdW-DF to obtain better binding energies. This improved functional is called vdW-DF2 and contains a refitted Perdew-Wang PW86R exchange functional term [110]. They later combined vdW-DF2 with C09_{*x*} to develop the vdW-DF2-C09_{*x*} exchange-correlation functional, which addressed the overestimated interlayer distances and binding energies obtained with vdW-DF and vdW-DF-C09_{*x*}, respectively [109, 108]. The detailed formulation of these functionals is presented in chapter 3. There are already various test studies [98, 99, 100, 101, 102, 103, 104, 106, 107, 108, 110, 111, 112, 113, 114] of these newly developed exchange-correlations

functionals on pristine systems, but less on defective systems.

1.2 Objectives

In this thesis, we present a first principles density functional study of the adsorption of hydrogen (H) and lithium (Li) atoms on bilayer graphene. Previous DFT investigations of these materials have so far, not accurately included the effects of the van der Waals (vdW) forces. The data reported in this thesis will be calculated using exchange-correlation functionals that take the effects of vdW interactions into account. For hydrogenation, the study is motivated by the contradiction found in the literature on the electronic properties, whereby some studies revealed that hydrogenated bilayer graphene exhibits metallic, whereas others reported insulating behaviour. Therefore, extensive study is required to address the discrepancy between the previous studies.

In this thesis, we are interested in finding all the possible H configurations at 50 % and 100 % coverage on a 1×1 cell. Boukhvalov *et al.* [10] investigated the chemisorption of a single H atom, and a pair of H atoms on a 32-atom supercell. These two configurations correspond to H coverage of 3.1% and 6.3%, respectively. These two H coverages are low, and insufficient to capture the H-induced transformations of the bilayer graphene structure. Moreover, the more recent investigation of Leenaerts *et al.* [13] considered a single configuration for H adsorption at 50% coverage. Our main aim is to identify and predict the lowest energy competing configurations that may exist at 50 % and 100 % hydrogenation, based on the formation energies calculated using the four variants of the non-local van der Waals density functionals (vdW-DF, vdW-DF2, vdW-DF C09_x and vdW-DF2 C09_x). We compare these results with GGA-PBE and LDA.

Thereafter, we increase the size of the cell to 2×1 to show other energetically stable configurations at 100% that are not possible in a 1×1 cell, and to understand the

effects of the cell sizes. In a 2×1 supercell, several physically interesting configurations such as chair, zigzag and boat conformers are examined. Because previous studies only focused on hydrogenating the top and bottom external faces of bilayer graphene [13], we also consider the hydrogenation of the interlayer faces. To investigate the influence of H on the geometries of bilayer graphene and the effects of the exchange-correlation functionals, the interlayer distances, bond distances and angles are measured after each structural relaxation. The electronic behaviour of the predicted lowest energy competing configurations is examined by analyzing the electronic band structure plots. A comparison is then made with that of pristine bilayer graphene. Since an understanding of the effect of H on the strength of bilayer graphene is required, the mechanical and elastic properties of the lowest energy competing configurations are also calculated.

In the literature, it was reported that AB stacking is more energetically stable than AA stacking; however the opposite scenario is noted during the intercalation of Li atoms. Previous studies usually report only the energetics of the Li-ion intercalated structures obtained using the GGA and LDA functionals [16, 19, 74, 75, 76, 77, 17]. In this thesis, we perform a thorough systematic investigation of the adsorption of Li atoms on AA and AB stackings of bilayer graphene. The objective is to investigate and understand the effects of Li on the geometry, the interlayer spacing, energetics and electronic properties (density of states). All the possible configurations of single and pairs of Li adatoms are identified on 2×2 supercells, to find the lowest energy competing structures and also to discover the configuration that makes the translation from AB to AA stacking. To accurately describe the bonding that occurs in bilayer graphene, the four variants of the non-local van der Waals density functionals (vdW-DF, vdW-DF2, vdW-DF C09_x and vdW-DF2 C09_x) are used, and we also compare these results with GGA-PBE. The dependence of workfunction on the interlayer spacing predicted by various functionals is also investigated. Lastly, to quantify the effects of Li-ions on the local structure of bilayer graphene, the amount of charge transfer is calculated by

integrating the density of states plots.

1.3 Synopsis

This thesis is structured in the following manner: Chapter 2 reviews previous work carried out on the hydrogenated and lithiated bilayer graphene. In chapter 3, we cover the theoretical background of the various methods used for the electronic structure calculations. Firstly, the formulation of DFT and its standard exchange-correlation functionals (such as LDA and GGA) are given. Since it is known that these standard functionals fail to correctly describe the effects of van der Waals interactions in complex, sparse, layered materials, a detailed overview of the newly developed non-local functionals capable of capturing these effects is presented. Chapter 4 describes the studies on the adsorption of H on bilayer graphene at 50% coverage. All possible H configuration on a 1×1 unit-cell are identified, and a comparison with results from other studies is made where possible. Chapter 5 presents the studies on the adsorption of H on bilayer graphene at 100% coverage. A comparative investigation of all H configurations from 1×1 and 2×1 cells is made. Chapter 6 presents an *ab initio* studies on the adsorption of Li on bilayer graphene. A comparative investigation of the adsorption of Li atoms on *AA* and *AB* stacked bilayer graphene is performed. Finally, a summary, general conclusion and future work stemming from this study are provided in chapter 7.

Bibliography

- [1] J. C. Charlier, X. Blase and S. Roche, *Carbon* **79**, 677 (2007). [1]
- [2] A. H. Castro, F. Guinea, N. M. R. Peres, K. S. Novoselov, and A. K. Geim, *Rev. Mod. Phys.* **81**, 109 (2009). [1, 3]
- [3] P. R. Wallace, *Phys. Rev.* **71**, 622 (1947). [1, 3]
- [4] J. S. Park, A. Reina, R. Saito, J. Kong, G. Dresselhaus and M. S. Dresselhaus, *Carbon* **47**, 1303-1210 (2009). [1]
- [5] K. S. Novoselov, A. K. Geim, S. V. Morozov, D. Jiang, Y. Zhang, S. V. Dubonos, I. V. Grigorieva, and A. A. Firsov, *Sci.* **306**, 666 (2004). [1, 2, 3, 4]
- [6] K. S. Novoselov, D. Jiang, T. Booth, V. V. Khotkevich, S. M. Morozov and A. K. Geim, *PNA*, **102**, 10451 (2005). [1, 2, 3]
- [7] K. S. Novoselov, A. K. Geim, S. V. Morozov, D. Jiang, Y. Zhang, M. I. Katsnelson, S. V. Dubonos, I. V. Grigorieva, and A. A. Firsov, *Nature (London)* **438**, 197 (2005). [1, 2, 3]
- [8] A. K. Geim and K. S. Novoselov, *Nature Mater.* **6**, 183 (2007). [1, 2]
- [9] Y. Zhang, Y. W. Tan, H. L. Stormer, and P. Kim, *Nature (London)* **438**, 201 (2005). [1, 2]
- [10] F. Schedin, A. K. Geim, S. V. Morozov, E. W. Hill, P. Blake, M. I. Katsnelson, and K. S. Novoselov, *Nature Mater.* **6**, 652 (2007). [2]
- [11] [http://www.nobelprize.org/nobelprizes/physics/laureates/2010/press.html\(2013-07-19\)](http://www.nobelprize.org/nobelprizes/physics/laureates/2010/press.html(2013-07-19)). [2]

- [12] A. Peigney, C. Laurent, E. Flahaut, R. R. Bacsa, A. Rousset, *Carbon* **39** 507-514 (2001). [2]
- [13] J. B. Hou, Y. Y. Shao, M. W. Ellis, R. B. Moore, B. L. Yi, *Phys. Chem. Chem. Phys.* **13** 15384-15402 (2011). [2]
- [14] T. Braun, M. Wohlers, T. Belz, G. Nowitzke, G. Wortmann, Y. Uchida, N. Pfander, R. Schlogl, *Cat. Lett.* **43** 167-173 (1997). [2]
- [15] M. S. Dresselhaus, G. Dresselhaus, *Adv. Phys.* **30**,139-326 (1981). [2]
- [16] S. Kobayashi, T. Takenobu, S. Mori, A. Fujiwara, Y. Iwasa, *App. Phys. Lett.* **82** 45814583 (2003). [2]
- [17] T. Durkop, S. Getty, E. Cobas, M. Fuhrer, *Nano Lett.* **4**, 35-39 (2004). [2]
- [18] A. A. Balandin, S. Ghosh, W. Z. Bao, I. Calizo, D. Teweldebrhan, F. Miao, C. N. Lau, *Nano Lett.* **8**, 902-907 (2008). [2]
- [19] H. Fukushima, L. Drzal, B. Rook, M. Rich, *Journal of Thermal Analysis and Calorimetry* **85**, 235-238 (2006). [2]
- [20] P. Kim, L. Shi, A. Majumdar, P. McEuen, *Phys. Rev. Lett.* **87**, 215502-215505 (2001). [2]
- [21] Y. Hwang, J. Lee, C. Lee, Y. Jung, S. Cheong, C. Lee, B. Ku, S. Jang, *Thermochemica Acta* **455**, 70-74 (2007). [2]
- [22] C. Lee, X.D. Wei, J.W. Kysar, J. Hone, *Sci.* **321**, 385-388 (2008). [2]
- [23] L. Schadler, S. Giannaris, P. Ajayan, *App. Phys. Lett.* **73**,3842 (1998). [2]
- [24] R. H. Baughman, C. Cui, A. A. Zakhidov, Z. Iqbal, J. N. Barisci, G. M. Spinks, G. G. Wallace, A. Mazzoldi, D. De Rossi, A. G. Rinzler, *Sci.* **284**, 1340-1344 (1999). [2]
- [25] A. A. Kolomenskii, M. Szabadi, P. Hess, *App. Surf. Sci.* **86**, 591-596 (1995). [2]
- [26] X. Li, W. Cai, I. Jung, J. An, D. Yang, A. Velamakanni, R. Pinera, L. Colombo, and R. S. Ruoff, *ECS Trans.* **5** 41-52 (2009). [2, 4]

- [27] Blake *et al.*, Nano Lett. **8**, 1704 (2008). [2]
- [28] D. E. Soule, Phys. Rev. B **112**, 698 (1958). [2]
- [29] Y. Ryu, L. Yin and C. Yu, J. Mater. Chem. **22**, 6959-6964 (2012). [2]
- [30] B. P. Grady, Carbon Nanotube-Polymer Composites: Manufacture, Properties, and Applications, John Wiley & Sons Inc. (2011). [2]
- [31] K. S. Novoselov, V. I. Fal'ko, L. Colombo, P. R. Gellert, M. G. Schwab and K. Kim, Nat. **490**, 192 (2012). [3, 4]
- [32] H. J. Choi, S. M. Jung, J. M. Seo, D. W. Chang, L. Daic, and J. B. Baeka, Nano Energy **1** 534-551 (2012). [3]
- [33] N. G Sahoo, Y. Pan, L. Li, S. H. Chan, Mater. **30** 4203 (2012). [3]
- [34] M. Terrones, B. R. Botello-Mendez, J. Campos-Delgado, F. Lopez-Urias, Y. I. Vega-Cantu, F. J Rodriguez-Macias, A. L. Elias, E. Munoz-Sandoval, A. G. Cano-Marquez, J. C. Chalker, and H. Terrones, Nano Today **5**, 351 (2010). [3]
- [35] P. L. de Andres, R. Ramirez, and J. A. Verges, Phys. Rev. B **77**, 045403 (2008). [3]
- [36] H. Min and A. H. MacDonald, Phys. Rev. B **77**, 155416 (2008). [3]
- [37] W. Choi, I. Lahiri, R. Seelaboyina, and Y. S. Kang, Crit. Rev. Sol. Stat. and Mater. Sci. **35**, 52 (2010). [3]
- [38] T. Ohta, A. Bostwick, T. Seyller, K. Horn, and E. Rotenberg, Sci. **313**, 951 (2006). [3, 5]
- [39] Yoo. *et al.* Nano Lett. **9**, 2255-2259 (2008). [4]
- [40] J. Wu, M. Agrawal, H. A. Becerril, Z. Bao, Z. Liu, Y. Chen, P. Peumans, ACS Nano **4**, 43 2009. [4]
- [41] K. S. Kim, Y. Zhao, H. Jang, S. Y. Lee, J. M. Kim, K. S. Kim, J. H. Ahn, P. Kim, J. Y. Choi, B. H. Hong, Nature (London) **457**, 457 (2009). [4]

- [42] A. Reina, X. T. Jia, J. Ho, D. Nezich, H. B. Son, V. Bulovic, M. S. Dresselhaus, J. Kong, *Nano. Lett.* **9** 3087 (2009). [4]
- [43] L. Sun, Q. X. Li, H. Ren, H. B. Su, Q. W. Shi, and J. L. Yang, *J. Chem. Phys.* **129**, 074074 (2008). [5]
- [44] Y. W. Son, M. L. Cohen, and S. G. Louie, *Phys. Rev. Lett.* **97**, 216803 (2006). [5]
- [45] M. Y. Han, B. Ozyilmaz, Y. Zhang, and P. Kim, *Phys. Rev. Lett.* **98**, 206805 (2007). [5]
- [46] F. Ding, *Phys. Rev. B* **72**, 245409 (2005). [5]
- [47] G. D. Lee, C. Z. Wang, E. Yoon, N. M. Hwang, D. Y. Kim, and K. M. Ho, *Phys. Rev. Lett.* **95**, 205501 (2005). [5]
- [48] M. T. Lusk and L. D. Carr, *Phys. Rev. Lett.* **100**, 175503 (2008). [5]
- [49] S. C Pradhan and J. K. Phadikar, *Phys. Lett. A* **373**, 1062 (2009). [5]
- [50] P. Lu, Z. Zhang, and W. Guo, *Phys. Lett.* **373**, 3354 (2009). [5]
- [51] J. A. Yan, L. Xian, and M. Y. Chou, *Phys. Rev. Lett.* **103**, 086802 (2009). [5]
- [52] X. S. Wu, M. Sprinkle, X. B. Li, F. Ming, C. Berger, and W. A. de Heer, *Phys. Rev. Lett.* **101**, 026801 (2008). [5]
- [53] I. Jung, D. A. Dikin, R. D. Piner, and R. S. Ruoff, *Nano Lett.* **8**, 4283 (2008). [5]
- [54] Z. Luo, P. M. Vora, E. J. Mele, A. T. C. Johnson, and J. M. Kikkawa, *Appl. Phys. Lett.* **94**, 111909 (2009). [5]
- [55] R. Balog, B. Jorgensen, L. Nilsson, M. Andersen, E. Rienks, M. Bianchi, M. Fanetti, E. Laegsgaard, A. Baraldi, S. Lizzit, Z. Sljivancanin, F. Besenbacher, B. Hammer, T. G. Pedersen, P. Hofmann, and L. Hornekaer. *Nature Mater.* **9**, 315 (2010). [5]
- [56] A. Savchenko, *Sci.* **323**, 589 (2009). [5]
- [57] D. C. Elias, R. R. Nair, T. M. G. Mohiuddin, S. V. Morozov, P. Blake, M. P. Halsall, A. C. Ferrari, D. W Boukhvalov, M. I. Katsnelson, A. K. Geim, and K. S. Novoselov, *Sci.* **323**, 610 (2009). [5, 21]

- [58] Y. H. Lu, W. Chen, Y. P. Feng, and P. M. He, *J. Phys. Chem. B* **113**, 2 (2009). [5]
- [59] I. Zanella, S. Guerini, S. B. Fagan, J. MendesFilho, and A. G. SouzaFilho, *Phys. Rev. B* **77**, 073404 (2008). [5]
- [60] R. M. Ribeiro, N. M. R. Peres, J. Coutinho, and P. R. Briddon, *Phys. Rev. B* **78**, 075442 (2008). [5]
- [61] D. W. Boukhvalov, M. I. Katsnelson, and A. I. Lichtenstein, *Phys. Rev. B* **77**, 035427 (2008). [5, 9, 22]
- [62] S. Lebegue, M. Klintonberg, O. Eriksson, and M. I. Katsnelson, *Phys. Rev. B* **79**, 245117 (2009). [5]
- [63] E. J. Duplock, M. Scheffler, and P. J. D. Lindan, *Phys. Rev. Lett.* **92**, 225502 (2004). [5]
- [64] D. W. Boukhvalov and M. I. Katsnelson, *Phys. Rev. B* **78**, 085413 (2008). [5, 23]
- [65] N. Z. Lu, Z. Y. Li, and J. L. Yang, *J. Phys. Chem. C* **113**, 16741 (2009). [5]
- [66] J. O. Sofo, A. S. Chaudhari, and G. D. Barber, *Phys. Rev. B* **75**, 153401 (2007). [5]
- [67] Z. Q. Luo, T. Yu, K. J. Kim, Z. H. Ni, Y. M. You, S. H. Lim, Z. X. Shen, S. Z. Wang, and J. Y. Lin, *ACS NANO* **3**, 1781 (2009). [5, 6, 20, 21]
- [68] K. S. Subrahmanyam, P. Kumar, U. Maitra, A. Govindaraj, K. P. Hembram, U. V. Waghmare, and C. N. R. Rao, *Proc. Nat. Acad. Sci. (USA)* **108**, 2677 (2011). [5, 6, 21]
- [69] M. Jaiswal, C. H. Lim, Q. Bao, C. T. Toh, K. P. Loh, and B. Ozyilmaz, *ACS NANO* **5**, 888 (2011). [5, 6, 21]
- [70] O. Leenaerts, B. Partoens, and F.M. Peeters, *Phys. Rev. B* **80**, 245422 (2009). [5, 9, 10, 23, 24]
- [71] [http://www.hydrogen.energy.gov/science.html\(2013-07-19\)](http://www.hydrogen.energy.gov/science.html(2013-07-19)). [5]
- [72] K. Sugawara, K. Kanetani, T. Sato, and T. Takahashi, *AIP. Adv.* **1**, 022103 (2011). [6, 7, 10, 24, 25]

- [73] K. R. Kganyago, and P. E. Ngoepe, *Phys. Rev. B* **68**, 205111 (2003). [6, 10, 25]
- [74] M. Khantha, N. A. Cordero, L. M. Molina, J. A. Alonso, and L. A. Girifalco, *Phys. Rev. B* **70**, 125422 (2004). [6, 10]
- [75] R. E. Mapasha, and N. Chetty, *Comput. Mat. Sci.* **49**, (2010). [6, 10]
- [76] A. M. Garay-Tapia, A. H. Romero, and V. Barone, *J. Chem. Theory Comput.* **8**, (2012) [6, 10]
- [77] K. T. Chan, J. B. Neaton, M. L. Cohen, *Phys. Rev. B* **77**, 235430 (2008) [6, 10]
- [78] S. Watcharinyanon, L. I. Johansson, A. A. Zakharov, and C. Virojanadara, *Surf. Sci.* **606**,3 (2012) [6, 10, 25]
- [79] M. S. Dresselhaus, and G. Dresselhaus, *Adv. Phys.* **51**, 1 (2002). [6]
- [80] P. V. C. Medeiros, F. de Brito Mota, A. J. S. Mascarenhas, and C. M. C. de Castilho, *Nanotechnology.* **21**, 115701 (2010). [6]
- [81] C. K. Yang, *Appl. Phys. Lett* **94**, 163115 (2009). [6]
- [82] X. Wang, *Appl. Phys. Lett* **95**, 183103 (2009). [6]
- [83] K. Persson, Y. Hinuma, Y. S. Men, A. V. der Ven, and G. Ceder, *Phys. Rev. B* **82** , 125416 (2010). [6]
- [84] T. Piao, S. M. Park, C. H. Doh, and S. I. Moon, *J. Electrochem. Soc* **146**, 2794 (1999). [6]
- [85] M. Noel, and V. Suryanarayanan, *J. Power Sources* **111**, 193 (2002). [6]
- [86] <http://www.gizmag.com/graphene-paper-battery-anodes/23881/> (20/11/2012). [6]
- [87] T. Wei, F. Wang, J. Yan, J. Cheng, Z. Fan, and H. Song, *J. Electroanalyt. Chem.* **653** (2011). [6]
- [88] E. Pollak, B. Geng, K. J. Jeon, I. T. Lucas, T. J. Richardson, F. Wang, and R. Kostecki, *Nano. Lett* **10**, (2010). [6]

- [89] D.Y. Pan, S. Wang, B. Zhao, M.H. Wu, H.J. Zhang, Y. Wang, and Z. Jiao, Chem. Mater. **21** 3136-3142 (2009). [6]
- [90] K. T. Chan, J. B. Neaton, and M. L. Cohen, Phys. Rev. B **77**, 1-12 (2008). [7]
- [91] P. Lian, X. Zhu, S. Liang, *et al.* Electrochem. Acta, **55**, 3909-3914 (2010) [7]
- [92] P. Hohenberg, and W. Kohn, Phys. Rev. B **136** 864 (1964). [7]
- [93] J. P. Perdew, and A. Zunger, Phys. Rev. B **23** 5048 (1981). [7]
- [94] J. P. Perdew, K. Burke, M. Ernzerhof, Phys. Rev. Lett. **77**, 3865 (1996). [7, 8]
- [95] J. Kohanoff and N.I. Gidopoulos, Mol. Phys. and Quant. Chem. **2** Chapter 26, pp 532-568. [7]
- [96] M. C. Payne, M. P. Teter, D. C. Allan, T. A. Arias, and J. D. Joannopoulos, Rev. Mod. Phys. **64** 1045 (1992). [7]
- [97] W. Kohn and L. J. Sham, Phys. Rev, **140** A1133, (1965). [8]
- [98] M. Dion, H. Rydberg, E. Schroder, D. C. Langreth, and B. I. Lundqvist, Phys. Rev. Lett. **92**, 246401 (2004). [8]
- [99] O. A. von Lilienfeld, I. Tavernelli, U. Rothlisberger, D. Sebastiani, Phys. Rev. Lett. **93**, 153004 (2004). [8]
- [100] J. Antony, and S. Grimme, Phys. Chem. Chem. Phys. **8**, 5287 (2006). [8]
- [101] A. D. Becke, and E. R. Johnson, J. Chem. Phys. **127**, 154108 (2007). [8]
- [102] S. Grimme, J. Antony, T. Schwabe, and C. Muck-Lichtenfeld, Org. Biomol. Chem. **5**, 741 (2007). [8]
- [103] T. Sato, T. Tsuneda, and K. Hirao, J. Chem. Phys. **126**, 234114 (2007). [8]
- [104] A. Tkatchenko and M. Scheffler, Phys. Rev. Lett. **102**, 073005 (2009). [8]
- [105] Y. Zhang and W. Yang, Phys. Rev. Lett. **80**, 890 (1998). [8]

- [106] J. Klimes, D. R. Bowler, and A. Michaelides, *J. Phys. Condens. Matter* **22**, 022201 (2010). [8]
- [107] V. R. Cooper, *Phys. Rev. B* **81**, 161104 (2010). [8]
- [108] I. Hamada and M. Otani, *Phys. Rev. B* **82**, 153412 (2010). [8]
- [109] K. Lee, E. D. Murray, L. Kong, B. I. Lundqvist, and D. C. Langreth, *Phys. Rev. B* **82**, 081101 (2010). [8]
- [110] E. D. Murray, K. Lee, and D. C. Langreth, *J. Chem. Theory Comput.* **5**, 2754 (2009). [8]
- [111] V. R. Cooper, L. Kong, and D.C Langreth, *Phys. Proc. B* **3**, 1417-1430 (2010). [8]
- [112] T. Bjorkman, A. Gulans, A. V. Krasheninnikov and R. M. Nieminen, *J. Phys. Condens. Matter* **24** 424218 (2012). [8]
- [113] T. Bjorkman, A. Gulans, A. V. Krasheninnikov, and R. M. Nieminen, *Phys. Rev. Lett.* **108**, 235502 (2012). [8]
- [114] S. Lebegue, J. Harl, T. Gould, J. G. Angyan, G. Kresse, J. F. Dobson, *Phys. Rev. Lett.***105**, 196401 (2010). [8]

Chapter 2

Review of previous work

In this chapter, we report various previous studies on adsorption of hydrogen (H) and lithium (Li) on bilayer graphene using experimental and theoretical techniques. Since the synthesis of single and few layered graphene structures by Novoselov *et al.* [1] in 2004, many studies have been carried out both experimentally and theoretically in trying to understand, and also to alter, their electronic properties. Theoretically, most of the investigations of H and Li on bilayer graphene have been performed using LDA and GGA exchange-correlation functionals. Fewer have been carried out using the newly developed exchange-correlation functionals that take the effects of van der Waals forces into account (vdW-DF, vdW-DF2, vdW-DF-C09_x, and vdW-DF2-C09_x). In order to obtain a significant picture of the adsorption of H and Li on bilayer graphene using these newly developed functionals, it is imperative to be aware of the previous results obtained using experimental techniques and the widely used functionals.

2.1 Adsorption of hydrogen on bilayer graphene

Luo *et al.* [2] conducted a comparative investigation on the hydrogenation of single and a few single layers of graphene SLG (more than three bound graphene monolayers).

They reported that the hydrogenation of a few SLG is less feasible than those of bilayer and trilayer graphene. They also showed experimentally that the hydrogenation and dehydrogenation of graphene depends on the number of monolayers. They found that, depending on the plasma power, the H coverage can be manipulated up to a saturation level of 100 % coverage. The observation by Elias *et al.* [3] that a SLG is far more receptive to H than bilayer graphene is in direct contrast to the measurements of Luo *et al.* [2]. Ryu *et al.* [4] performed hydrogenation of single and bilayer graphene using *in situ* electron-induced dissociation of hydrogen silsesquioxane. Using Raman spectroscopy, it was found that hydrogenation proceeds at a higher rate for single layer graphene than bilayer graphene, demonstrating the enhanced chemical reactivity of single layer graphene.

Furthermore, Subrahmanyam *et al.* [5] demonstrated the possible use of few layer graphene in H storage. They showed that such structure can contain up to 5 wt % of H, which is more than the 3 wt % stored in carbon nanotubes. Their spectroscopic measurements on hydrogenated bilayer graphene showed that the local structure contains some sp^3 -hybridized carbon bonds. They also observed that H decomposes when the structure is heated up to 500 °C. Jaiswal *et al.* [6] investigated the electronic properties of graphene sheets at different degrees of hydrogenation using Raman and charge transport spectroscopies. They demonstrated that partially hydrogenated mono- and bi-layer graphene has weak insulating behaviour, and that bilayer graphene is more readily affected by H compared to a few single layers of graphene, in agreement with the measurements of Luo *et al.* [2]. Wojtaszek *et al.* [7] reported the hydrogenation of single and bilayer graphene by an argon-hydrogen plasma produced in a reactive ion-etching-system. They showed that under ambient plasma conditions, the process does not introduce considerable damage to the graphene sheet, and the hydrogenation level can be precisely controlled.

Tanabe *et al.* [8] reported the growth of Quasi-free-standing bilayer graphene on H

intercalation of epitaxial monolayer graphene on SiC(0001). A larger size of stacked sheets compared to that of epitaxial bilayer graphene, grown on SiC(0001) (without intercalation), was observed using low-energy electron microscopy. They also reported that the quasi-free-standing bilayer graphene is p-doped at zero-gate voltage, when its electronic transport characteristics in top-gated devices are evaluated. Lastly, it was reported that the exposed Quasi-free-standing bilayer graphene has higher electronic mobility than epitaxial bilayer graphene, and it was concluded that H improves the size and quality of the free-standing bilayer graphene [8]. Lately, Wang *et al.* [9] performed experimental studies of the physisorption of H₂ molecules on graphene at low and high surface coverages. Their calculated heats of adsorption indicated that high surface coverage was favoured, leading them to conclude that graphene has a high H storage capability.

Earlier, Boukhalov *et al.* [10] performed a comparative study of H adsorption on single and bilayer graphene using DFT to predict the geometries and energetics. For the exchange-correlation interactions, LDA and GGA were utilized. They considered a single and pair of H adatoms and found that the lattice distortions were different in single and bilayer structures. They observed that the distance between any two bonded carbon atoms in the bilayer is less than the equivalent distance in a single layer. This is because the interlayer interaction is trying to force the layers to remain flat. Based on the chemisorption energies, they concluded that in both structures, a pair of H adatoms stabilizes the structure better than the single H adatom [10]. This conclusion was also validated by the activation energies, since the single, and pair, of H adatoms yielded positive and negative activation energies, respectively. They also found that the hydrogenated monolayer is far more stable than the hydrogenated bilayer graphene. The chemisorption energy as a function of H concentration was also calculated, as well as energy barriers for H binding and release. They concluded that graphene and bilayer graphene can be perspective materials for H storage.

Later on, Boukhvalov *et al.* [11] argued that the maximum H coverage on bilayer graphene is 25%, and that this configuration gives the most stable structure. At this coverage, the interlayer distance reduces to 3.25 Å from the 3.35 Å obtained in pristine bilayer graphene. In this configuration, the band structure showed a wide gap between the conduction and valence bands. Zhou *et al.* [12] used a PBE version of GGA to investigate the energetics and electronic structure of a bilayer graphone (having 25% degrees of hydrogenation). It was found that the most stable configuration undergoes a 1×2 surface reconstruction. It was also reported that an energy barrier of 1.83 eV is needed to separate this structure from the non-bonded state. They also claimed that bilayer graphone is metallic due to the existence of a delocalized π orbital on the unhydrogenated sp^2 carbon atoms. This contradicts Boukhvalov's findings, leading us to believe that they might have studied two different configurations.

Leenaerts *et al.* [13] investigated the possibility of 50% H coverage on bilayer graphene. The interlayer distance was found to reduce significantly, resulting in the creation of strong covalent bonds that stabilize the structure. However this transformation only occurs when the H is adsorbed on top of an indirect carbon atom (i.e. on top of the carbon atom that faces the centre of the hexagon on the opposite layer). In this configuration, the unhydrogenated carbon atom faces another unhydrogenated carbon atom on the opposite layer. The resulting structure has a wide band gap. Nevertheless, the formation energy is still higher than that of the hydrogenated single layer graphene. On this basis, they also concluded that the hydrogenated single layer is more stable than the hydrogenated bilayer graphene. Berashevich and Chakraborty [14] studied magnetic properties of the same configuration that was studied by Leenaerts *et al.* [13]. They reported that the structure is spin-unpolarized and a non-magnetic material, whereby the molecular orbitals for spin-up and spin-down states are characterized by the same energy. They reported that this configuration has a wide band gap of 7.01 eV between the highest occupied molecular orbital and lowest unoccupied

molecular orbital. Recently, Rohrer *et al.* [15] performed van der Waals density functional (vdW-DF) studies on the adsorption of H atoms on bilayer graphene and bulk graphite at 100% coverage. Their results demonstrated that vdW interactions can alter the electronic behaviour in the Brillouin zone. They also found that the engineered band gap is caused by two geometry-induced effects, viz. (1) the hybridization between unoccupied wavefunctions in the lowest conduction band, and (2) the modification of the electrostatic interaction between hybrid wavefunctions and the total density.

Although some minor discrepancies are found, the experimental studies above proved that hydrogenated structures are easily controllable under the ambient conditions. This brings about hope for the manufacturing and development of logical transistors that could operate at higher frequencies. It also encourages theorists to continue studying these types of systems, predicting further unknown results and possible novel configurations. Apart from references [13, 15], all theoretical studies presented above have only considered low H coverage, this is not being sufficient to saturate all the dangling bonds. References [13] and [15] considered 50% and 100% H coverages, respectively, but not all the possible configurations were modelled. The issue of the missing configurations in previous studies forms the foundation of this project.

2.2 Adsorption of lithium on bilayer graphene

Recently, Sugawara *et al.* [16] performed experimental studies on structural and electronic properties of Li intercalated bilayer graphene. Using low-energy electron diffraction (LEED), it was found that the effect of Li atoms between the layers is to increase the interlayer distance as compared to the pristine structure [16], thereby increasing the volume of the material. Their [16] angle-resolved photo emission spectroscopy (ARPES) measurements revealed that the intercalated Li atoms are fully ionized. Furthermore, the ARPES spectra indicated that the Dirac-point shifted from the Fermi level into the

valence bands by 1.4 eV, revealing the metallicity of the structure. Watcharinyanon *et al.* [17] also conducted experimental studies on the structural and electronic properties of intercalated Li in hydrogenated bilayer graphene. Their low energy electron microscopy (LEEM) measurements indicated that the deposited Li atoms form islands of defects which disappear during annealing. They also noted that the workfunction of the sample (bilayer) decreases after the deposition of Li-ions. Similar to the observation of Sugawara *et al.* [16], Watcharinyanon *et al.* [17] conducted ARPES measurements on the Li deposited sample and found that the Dirac-point also shifted from the Fermi level to the valence bands by 1.25 eV.

Virojanadara *et al.* [18] used LEEM, ARPES and μ -LEED to probe the influence of Li-ions on monolayer graphene grown on a silicon-terminated SiC (0001) surface. They noted the growth of a carbon interface (buffer) layer between the graphene and induced bulk SiC. Their results showed that the Li-ions penetrate through the graphene and carbon buffer layer. This observation reveals that Li-ions prefer to be sandwiched between the layers. The LEEM measurements deduced that the workfunction of the sample was reduced after Li deposition. Their ARPES results also confirmed the metallic behaviour of the compound.

Kganyago *et al.* [19] used GGA and LDA to investigate the lattice and electronic properties of Li intercalated graphite. It was reported that for pristine structures, GGA gives meaningless values but after Li intercalation the results are in good agreement with the experimental results. They found that the lithiated structures possess metallic behaviour. Imai and Wanatabe [20] also used GGA and LDA to investigate the energetics and geometries of Li intercalated graphite. They reported that the two functionals predict relatively good, reproducible, lattice constants for this lithiated structure. Denis [21] examined the chemical reactivity of Li-ions doped on monolayer and bilayer graphene using the DFT method. For the description of the exchange-correlation interaction, GGA-PBE and LDA functionals were used in the Li adsorbed single layer

graphene and bilayer graphene, respectively. The LDA functional was employed ostensibly to take into account the effect of the van der Waals forces. It was found that these Li doped structures are metallic in nature. It was revealed that the metallic character of Li-adsorbed single layer graphene can be easily affected by the attachment of radicals (OH, CH₃, H, etc), resulting in an observable band gap, but in Li-doped bilayer graphene, the metallicity was always retained after the attachment of radicals.

Zhou *et al.* [22] employed the LDA functional to perform comparative investigations of Li-ions intercalated AA and AB stacked bilayer graphenes. They found that for each Li-ions concentration, the Li intercalated AA stacking is lower in total energy compared to Li intercalated AB stacking. Interestingly, for the intercalation of one Li atom, both stackings have the same interlayer spacing but differ when the Li concentration increases. It was also revealed that due to an increase in the Li concentration, the AB stacking translates to AA stacking after relaxation. Kaloni *et al.* [23] conducted a DFT study to investigate the intrinsic charge carrier densities in Li intercalated bulk graphite, bilayer and trilayer graphene using the GGA functional. Firstly, it was observed that for all the systems under study, Li induces a metallic character and enhances the intrinsic charge carrier densities. They also deduced that Li-intercalated bilayer graphene has higher charge carrier densities than Li intercalated bulk graphite and trilayer graphene.

Lately, Buldum *et al.* [24] used DFT with LDA and GGA to predict the energetically stable and most promising graphene lithiated structures for battery applications. They performed a systematic study of different number of Li-ion layers on single and multilayer graphene structures. They found that the most energetically favourable structure is a single graphene layer having four lithium layers. It was established that this compound has six times the lithium density of that of intercalated graphite. The presence of a high concentration of electron density was also observed around the positive lithium atom. They suggested that this characteristic is useful in designing new,

advanced materials for battery applications. Chan and Hill [25] investigated the storage of lithium-ions between two parallel graphene sheets using the 6-12 Lennard-Jones potential to account for non-local effects. They noted the growth of single, double, and triple Li-ion layers forming between graphene layers. It was argued that double and triple configurations exceed the maximum theoretical storage capacity of graphite. It was also noted that a single Li-ion layer provides the least charge storage, but is the most stable configuration.

Apart from reference [25], all other studies have neglected the effects of van der Waals forces in their systems. Since we have the newly developed non-local density functionals, it will be useful to compare them with the widely used functionals on these lithiated structures. Moreover, Chan [25] considered only the Li intercalated structure. It will also be useful to examine the response of the new functionals to the various Li configurations on bilayer graphene.

Bibliography

- [1] K. S. Novoselov, A. K. Geim, S. V. Morozov, D. Jiang, Y. Zhang, S. V. Dubonos, I. V. Grigorieva, and A. A. Firsov, *Sci.* **306**, 666 (2004). [20]
- [2] Z. Q. Luo, T. Yu, K. J. Kim, Z. H. Ni, Y. M. You, S. H. Lim, Z. X. Shen, S. Z. Wang, and J. Y. Lin, *ACSNANO* **3**, 1781 (2009). [5, 6, 20, 21]
- [3] D. C. Elias, R. R. Nair, T. M. G. Mohiuddin, S. V. Morozov, P. Blake, M. P. Halsall, A. C. Ferrari, D. W. Boukhvalov, M. I. Katsnelson, A. K. Geim, and K. S. Novoselov, *sci.* **323**, 610 (2009). [5, 21]
- [4] S. Ryu, M. Y. Han, J. Maultzsch, T. F. Heinz, P. Kim, M. L. Steigerwald, and L. E. Brus, *Nano Lett.* **8** 4597 (2008). [21]
- [5] K. S. Subrahmanyam, P. Kumar, U. Maitra, A. Govindaraj, K. P. Hembam, U. V. Waghmare, and C.N.R. Rao, *Proc. Nat. Acad. Sci.(USA)* **108**, 2677 (2011). [5, 6, 21]
- [6] M. Jaiswal, C. H. Lim, Q. Bao, C. T. Toh, K. P. Loh, and B. Ozyilmaz, *ACSNANO* **5**, 888 (2011). [5, 6, 21]
- [7] M. Wojtaszek, N. Tombros, A. Caretta, P. H. M. van Loosdrecht, and B. J. van Wees, *JAP*, **110**, 063715-063715-6 (2011). [21]
- [8] S. Tanabe, Y. Sekine, H. Kageshima, and H. Hibino, *JJAP* **51** 02BN02 (2012). [21, 22]
- [9] L. Wang, N. R. Stuckert, and R. T. Yang, *AIChE*, **57**, 10 (2011). [22]
- [10] D. W. Boukhvalov, M. I. Katsnelson, and A. I. Lichtenstein, *Phys. Rev. B* **77**, 035427 (2008). [5, 9, 22]

- [11] D. W. Boukhvalov and M. I. Katsnelson, Phys. Rev. B **78**, 085413 (2008). [5, 23]
- [12] J. Zhou, Q. Wang, Q. Sun, and P. Jena, App. Phys. Lett. **98**, 063108 (2011). [23]
- [13] O. Leenaerts, B. Partoens, and F.M. Peeters, Phys. Rev. B **80**, 245422 (2009). [5, 9, 10, 23, 24]
- [14] J. Berashevich and T. Chakraborty, EPL, **93** 47007 (2011). [23]
- [15] J. Rohrer, and P. Hyldgaard, Phys. Rev. B **83**, 165423 (2011). [24]
- [16] K. Sugawara, K. Kanetani, T. Sato, and T. Takahashi, AIP. Adv. **1**, 022103 (2011). [6, 7, 10, 24, 25]
- [17] S. Watcharinyanon, L. I. Johansson, A. A. Zakharov, and C. Virojanadara, Surf. Sci. **606**,3 (2012). [6, 10, 25]
- [18] C. Virojanadara, S. Watcharinyanon, A. A. Zakharov, and L. I. Johansson, Phys. Rev. B **82**, 205402 (2010). [25]
- [19] K. R. Kganyago, and P. E. Ngoepe, Phys. Rev. B **68**, 205111 (2003). [6, 10, 25]
- [20] Y. Imai, and A. Watanabe, J. Alloys Compd. **439**, (2007). [25]
- [21] P. A Denis, J. Phys. Chem. C **115**, 27 (2011). [25]
- [22] J. J. Zhou, W. W. Zhou, C. M. Guan, J.Q. Shen, C. Y. Ouyang, M. S. Lei, S.Q. Shi and W.H. Tang, Sci. China-Phys. Mech. Astron. **55**, 8 (2012). [26]
- [23] T. P. Kaloni, Y. C. Cheng, M. Upadhyay Kahaly, U. Schwingenschlogl, Chem. Phys. Lett. **534**, (2012). [26]
- [24] A. Bulduma, and G. Tetiker, JAP **113**, 154312 (2013). [26]
- [25] Y. Chan, and J. Hill, NRL **6** 203 (2011). [27]

Chapter 3

Electronic structure methods

In this chapter, we cover the theoretical background of various methods used for electronic structure calculations. Firstly, the formulation of DFT and its standard exchange-correlation functionals (such as local density approximation and generalized gradient approximation) are given. Since it is known that these standard functionals fail to correctly describe the effects of van der Waals interactions in complex, sparse, layered materials, a detailed overview of the newly developed non-local functionals capable of capturing these effects is presented.

3.1 Introduction

In this thesis, the quantum mechanical model is solved to understand various properties of pristine, hydrogenated and lithiated bilayer graphenes. This model is appropriate because we are dealing with interactions at the electronic level. Ignoring relativistic effects, this quantum mechanical model is called the time-independent many-body Schrödinger equation [1, 2],

$$\hat{H}\Psi = E\Psi \tag{3.1}$$

where Ψ is the many-body wavefunction that depends on the ionic and electronic degrees of freedom. The Hamiltonian operator \hat{H} is expressed as

$$\begin{aligned} \hat{H} = & -\hbar^2 \sum_i \frac{\nabla_i^2}{2m_e} - \hbar^2 \sum_I \frac{\nabla_I^2}{2M_I} + \frac{1}{2} \sum_{i \neq j} \frac{e^2}{|\mathbf{r}_i - \mathbf{r}_j|} - \sum_{i,I} \frac{Z_I e^2}{|\mathbf{r}_i - \mathbf{R}_I|} \\ & + \frac{1}{2} \sum_{I \neq J} \frac{Z_I Z_J e^2}{|\mathbf{R}_I - \mathbf{R}_J|}. \end{aligned} \quad (3.2)$$

The first two terms in \hat{H} are the kinetic energy contributions (\hat{T}_e and \hat{T}_I) arising from the electrons and ions, respectively. The last three terms are the potential energy terms (\hat{V}_{ee} , \hat{V}_{Ie} and \hat{V}_{II}) describing the electron-electron, ion-electron and ion-ion Coulomb interactions, respectively. The term \hat{V}_{Ie} is also known as external potential energy (\hat{V}_{ext}) because the effect of ions on electrons is included in a fixed local external potential [3]. The letter \mathbf{r}_i denotes the configuration of the i^{th} electron, whereas \mathbf{R}_I and M_I are the position and mass of the I^{th} ion, respectively. The letter Z in Eqn. (3.2) is the atomic number for each ion.

Eqn. (3.1) is solved to obtain the many body ground state wavefunction $\Psi(\mathbf{r}_1, \mathbf{r}_2, \dots, \mathbf{r}_n, \mathbf{R}_1, \mathbf{R}_2, \dots, \mathbf{R}_M)$, from which various material properties can be derived. However, solving Eqn. (3.1) is a formidable task because of the complicated interactions presented in Eqn. (3.2). In order to handle such an intractable task, the Born-Oppenheimer approximation [4] is utilized. This approximation is based on the large mass differences between electrons and nuclei. For instance, the lightest nuclei weighs approximately 1800 times more than an electron [1]. Therefore, \hat{T}_I in Eqn. (3.2) is ignored, reducing it to

$$\hat{H} = \hat{T}_e + \hat{V}_{ee} + \hat{V}_{ext} + \hat{V}_{II} \quad (3.3)$$

such that Eqn (3.1) is expressed as

$$[\hat{T}_e + \hat{V}_{ee} + \hat{V}_{ext} + \hat{V}_{II}]\Psi = E\Psi. \quad (3.4)$$

The term \hat{V}_{II} is sometimes used as an added constant; it has an influence on the total energy of the system but is irrelevant to the electronic problem [3]. For that matter, Eqn. (3.4) consists of electrons moving under the influence of the fixed external potential. Owing to the large number of interacting electrons in real material systems, Eqn. (3.4) is still not solvable, even when using supercomputers, and therefore it requires further simplification.

In 1928, Hartree [5] proposed an approximation to reduce the complexity of this enormous number of interacting particles (electrons). In the Hartree approximation, the many-particle wavefunction $\Psi(\mathbf{r}_1, \mathbf{r}_2, \dots, \mathbf{r}_n, \mathbf{R}_1, \mathbf{R}_2, \dots, \mathbf{R}_M)$ is written as the product of the single independent electron wavefunctions $\psi(\mathbf{r}_1)\psi(\mathbf{r}_2)\dots\psi(\mathbf{r}_n)$. Thus, Eqn. (3.4) becomes a one-particle Schrödinger equation that is satisfied by the wavefunction $\psi_i(\mathbf{r})$ of the i^{th} electron [3, 6], and takes the form

$$[\hat{T}_e + \hat{V}_{eff}]\psi_i(\mathbf{r}) = \epsilon_i(\mathbf{r})\psi_i(\mathbf{r}), \quad (3.5)$$

where \hat{V}_{eff} is the effective potential defined as

$$\hat{V}_{eff} = \hat{V}_{ext} + \sum_{i \neq j}^N \int \frac{d^3r'}{|\mathbf{r} - \mathbf{r}'|} n_j(\mathbf{r}') \quad (3.6)$$

where $n_j(\mathbf{r}')$ is the electronic density of the j^{th} particle, and can be defined as

$$n_j(\mathbf{r}') = |\psi_j(\mathbf{r}')|^2. \quad (3.7)$$

The second term of Eqn. (3.6) describes the classical electrostatic potential energy generated by the self-interacting continuous charge distribution $\sum_{i \neq j}^N n_j(\mathbf{r}')$ and is also known as the Hartree potential ($V_{Hartree}$) [3]. The Greek letter ϵ_i in Eqn. (3.5) repre-

sents the one-electron energy eigenvalue of the i^{th} electron. From here on we adopt the atomic units system as $\hbar = m_e = e = 4\pi/\varepsilon_0 = 1$. The one-electron kinetic energy term in Eqn. (3.5) is reduced to

$$T_e = -\frac{1}{2}\nabla^2. \quad (3.8)$$

The solution to the independent-electron Schrödinger equation (Eqn. (3.5)) is obtained by a self-consistent field method, also known as self-consistent Hartree approximation [6]. Starting with an initial guess for the wavefunction to construct the density $n(\mathbf{r})$ using Eqn. (3.7), followed by constructing the expression for the effective potential, Eqn. (3.5) can be solved. This defines a new set of eigenwavefunctions which are used as inputs for the next cycle. The process repeats until the input and output wavefunctions are the same. Therefore the energy is minimized with respect to a set of variational parameters.

The Hartree approximation or independent-electron Schrödinger equation is somehow limited, because it is only capable of treating distinguishable particles [6]. Therefore, Eqn. (3.5) is not capable of representing real systems. In 1930, Fock [7] improved the Hartree approximation by anti-symmetrizing the many-particle wavefunction $\Psi(\mathbf{r}_1, \mathbf{r}_2, \dots, \mathbf{r}_n, \mathbf{R}_1, \mathbf{R}_2, \dots, \mathbf{R}_M)$. This was done by ensuring that the fermions satisfy the Pauli exclusion principle (no two electrons occupy the same state). Thereafter, it was proposed that the Hartree-Fock wavefunction (antisymmetric many-body wavefunction) should be written in the form of a Slater [8] determinant of one-electron wavefunctions

$$\Psi_e(\{\mathbf{r}_i, \sigma_i\}) = \frac{1}{\sqrt{N!}} \begin{vmatrix} \psi_1(\mathbf{r}_1, \sigma_1) & \psi_1(\mathbf{r}_2, \sigma_2) & \dots & \psi_1(\mathbf{r}_N, \sigma_N) \\ \psi_2(\mathbf{r}_1, \sigma_1) & \psi_2(\mathbf{r}_2, \sigma_2) & \dots & \psi_2(\mathbf{r}_N, \sigma_N) \\ \vdots & \vdots & \ddots & \vdots \\ \psi_N(\mathbf{r}_1, \sigma_1) & \psi_N(\mathbf{r}_2, \sigma_2) & \dots & \psi_N(\mathbf{r}_N, \sigma_N) \end{vmatrix}. \quad (3.9)$$

The expectation of the Hamiltonian [3] of Eqn. (3.5), using the wavefunction from Eqn. (3.9), is given by

$$\begin{aligned} \langle \Psi | H | \Psi \rangle = & \sum_{i,\sigma} \int d^3\mathbf{r} \psi_i^{\sigma*}(\mathbf{r}) [T_e + V_{ext}] \psi_i^\sigma(\mathbf{r}) + V_{Hartree} \\ & - \frac{1}{2} \sum_{i,j,\sigma} \int d^3\mathbf{r} d^3\mathbf{r}' \psi_i^{\sigma*}(\mathbf{r}) \psi_j^{\sigma*}(\mathbf{r}') \frac{1}{|\mathbf{r} - \mathbf{r}'|} \psi_j^\sigma(\mathbf{r}) \psi_i^\sigma(\mathbf{r}'). \end{aligned} \quad (3.10)$$

The first term in Eqn. (3.10) involves single-body expectation values, and still represents that of the Hartree approximation. The last term on the right hand side is the exact exchange energy that describes the Coulomb interaction which occurs between the electrons of the same spin [7]. The fraction $\frac{1}{2}$ is included in the exchange energy term since the electron-electron interaction is counted twice.

The exchange potential energy term can be given by the sum, over all orbitals, of the same spin as

$$V_x^{i,\sigma}(\mathbf{r}) = - \left[\sum_j \int d^3\mathbf{r}' \psi_j^{\sigma*}(\mathbf{r}') \psi_i^\sigma(\mathbf{r}') \frac{1}{|\mathbf{r} - \mathbf{r}'|} \right] \frac{\psi_j^\sigma(\mathbf{r})}{\psi_i^\sigma(\mathbf{r})}. \quad (3.11)$$

The single-electron Hartree-Fock equation [3] below is obtained by minimizing Eqn. (3.10) with respect to the many-body Slater wavefunction Eqn. (3.9)

$$[T_e + V_{ext}(\mathbf{r}) + V_{Hartree} + V_x^{i,\sigma}(\mathbf{r})] \psi_i^\sigma(\mathbf{r}) = \epsilon_i^\sigma \psi_i^\sigma(\mathbf{r}). \quad (3.12)$$

The Hartree-Fock approximation has been a reliable approach used by chemists to calculate various properties of molecular structures. Recently, this method has been used as a starting point for other theoretical methods such as the Moller-Plesset perturbation theory of second (MP2) and fourth (MP4) order [9]. Here the Hartree-Fock wavefunction is used to introduce the electronic correlations [6].

The Hartree-Fock approximation fails to correctly describe the known properties of the homogeneous electron gas. It predicts that the electronic density of states vanishes in the vicinity of the Fermi level, which is incorrect. This is caused by the neglect of the Coulomb repulsion felt by all electrons of opposite spin. This introduces a correlation energy for the electrons in Eqn. (3.10). The correlation energy is primarily described as the energy difference between the exact and Hartree-Fock energies [10]. To resolve this shortcoming, several approaches collectively called post-Hartree-Fock methods [11, 12], were developed. Another approximation is DFT [13, 14] which takes into account both the effects of exchange and correlation.

3.2 Density Functional Theory

DFT is the most popular tool used by both condensed matter physicists and quantum chemists to calculate the ground state properties of material systems [6, 10]. One of the reasons for its overwhelming success in the quantum chemistry community is its high computational efficiency compared to other popular approaches such as the Hartree and Hartree-Fock approximations. Besides the inclusion of the correlation potential of electrons in the DFT approach, its primary objective is to replace the many-body wavefunction $\Psi(\mathbf{r})$ associated with the Schrödinger equation by searching for the electronic density $n(\mathbf{r})$. $\Psi(\mathbf{r})$ is a very complicated mathematical entity to deal with because it depends on $4N$ variables, i.e. three spatial variables and one spin variable for each of the N electrons, and is therefore difficult to solve. The density $n(\mathbf{r})$ depends only on three spatial variables, and it can be experimentally measured as opposed to the mathematically constructed $\Psi(\mathbf{r})$.

The DFT technique is based on the two principal theorems formulated by Hohenberg and Kohn in their seminal paper [13] published in 1964. The two theorems are uncomplicated and quite easy to prove, and form the cornerstone of any implementa-

tion of DFT. The first theorem states that: *the non-degenerate ground state electron density $n(\mathbf{r})$ uniquely determines all the properties of the material (i.e ground state energies, wavefunction etc).* The proof of the first H-K theorem shows explicitly that the ground state electron density $n(\mathbf{r})$ determines the external potential $V_{ext}(\mathbf{r})$ for any interacting electronic system [13].

To proceed with the proof, the following assumptions are used: (1) two distinct external potentials $V_{ext}^1(\mathbf{r})$ and $V_{ext}^2(\mathbf{r})$ with their corresponding wavefunctions $\Psi^1(\mathbf{r})$ and $\Psi^2(\mathbf{r})$ are assumed to yield the same electron density $n(\mathbf{r})$, (2) the two external potentials $V_{ext}^1(\mathbf{r})$ and $V_{ext}^2(\mathbf{r})$ differ by more than a constant, (3) the ground state wavefunctions $\Psi^1(\mathbf{r})$ and $\Psi^2(\mathbf{r})$ are solutions to the Hamiltonians ($H^1 = T + U_{ee} + V^1$ and $H^2 = T + U_{ee} + V^2$) which have ground state energies (E^1 and E^2). The letters T , U_{ee} and V are the kinetic energy, Coulomb energy and external potential energy terms, respectively. The ground state energy E^1 can be expressed by the consideration of the Rayleigh Ritz variational (minimum) principle as follows:

$$E^1 = \langle \Psi^1(\mathbf{r}) | H^1 | \Psi^1(\mathbf{r}) \rangle < \langle \Psi^2(\mathbf{r}) | H^1 | \Psi^2(\mathbf{r}) \rangle. \quad (3.13)$$

Eqn. (3.13) shows that the Hamiltonians H^1 and H^2 are representatives of the different sets of Schrödinger equations. The last part of Eqn. (3.13) can be extended to

$$\langle \Psi^2(\mathbf{r}) | H^1 | \Psi^2(\mathbf{r}) \rangle = \langle \Psi^2(\mathbf{r}) | H^2 | \Psi^2(\mathbf{r}) \rangle + \int (V_{ext}^1 - V_{ext}^2) n(\mathbf{r}) d^3r \quad (3.14)$$

such that,

$$\langle \Psi^2(\mathbf{r}) | H^1 | \Psi^2(\mathbf{r}) \rangle = E^2 + \int (V_{ext}^1 - V_{ext}^2) n(\mathbf{r}) d^3r. \quad (3.15)$$

Then

$$E^1 < E^2 + \int (V_{ext}^1 - V_{ext}^2) n(\mathbf{r}) d^3r. \quad (3.16)$$

The variational principle is responsible for this strict inequality of non-degenerate ground state properties. The same relation is also considered for the ground state energy E^2 as

$$E^2 = \langle \Psi^2(\mathbf{r}) | H^2 | \Psi^2(\mathbf{r}) \rangle < \langle \Psi^1(\mathbf{r}) | H^2 | \Psi^1(\mathbf{r}) \rangle. \quad (3.17)$$

Expanding the last part of Eqn. (3.17),

$$\langle \Psi^1(\mathbf{r}) | H^2 | \Psi^1(\mathbf{r}) \rangle = \langle \Psi^1(\mathbf{r}) | H^1 | \Psi^1(\mathbf{r}) \rangle + \int (V_{ext}^2 - V_{ext}^1) n(\mathbf{r}) d^3r. \quad (3.18)$$

Similarly,

$$E^2 < E^1 + \int (V_{ext}^2 - V_{ext}^1) n(\mathbf{r}) d^3r. \quad (3.19)$$

When Eqns. (3.16) and (3.19) are added together, the following contradiction occurs:

$$E^1 + E^2 < E^2 + E^1. \quad (3.20)$$

The observed inconsistency in Eqn. (3.20) indicates that two external potentials V_{ext}^1 and V_{ext}^2 differing to within a constant, satisfying different sets of Schrödinger equations, cannot give the same ground state electron density $n(\mathbf{r})$. Thus, the ground state electron density $n(\mathbf{r})$ uniquely determines the external potential $V_{ext}(\mathbf{r})$ to within a constant [3, 1].

The second H-K theorem introduces the functional $F[n(\mathbf{r})]$, such that the ground state electron density and energy of an electronic system can be obtained through the variational principle, for any given external potential $V_{ext}(\mathbf{r})$ [13]. The functional $F[n(\mathbf{r})]$ is universal (it does not depend on the identity of the material). The second H-K theorem states that: *the electron density that minimizes the energy functional*

$E[n(\mathbf{r})]$ towards the ground state energy of the electronic system, is the true ground state electron density. The meaning of this theorem is that an exact electron density $n(\mathbf{r})$ minimizes the energy functional $E[n(\mathbf{r})]$ to be equal to the ground state energy E_0 of the system. In this thesis, the functional $F[n(\mathbf{r})]$ is defined through the constrained search approach of Levy and Lieb [15, 16] as

$$F[n(\mathbf{r})] = \min_{\Psi(\mathbf{r}) \rightarrow n(\mathbf{r})} \langle \Psi(\mathbf{r}) | T + U_{ee} | \Psi(\mathbf{r}) \rangle, \quad (3.21)$$

where T and U_{ee} are the kinetic and Coulomb (electronic interaction) energy terms, respectively. The minimum in Eqn. (3.21) is considered for all wavefunctions $\Psi(\mathbf{r})$ in the N -space for all N -representable densities which give the same density $n(\mathbf{r})$, for any given external potential, unlike in reference [13] where the subspace of N , also known as V -representable densities is considered. The V -representable densities can be applicable to some range of external potentials [17]. The energy functional $E[n(\mathbf{r})]$ in the case of the constrained search approach is

$$E[n(\mathbf{r})] = F[n(\mathbf{r})] + \int V_{ext}(\mathbf{r}) n(\mathbf{r}) d^3r \geq E_0, \quad (3.22)$$

for any given external potential. Considering the ground state electron density $n_0(\mathbf{r})$ that corresponds to the wavefunction $\Psi_0(\mathbf{r})$, Eqn. (3.22) is reduced to

$$E[n_0(\mathbf{r})] = F[n_0(\mathbf{r})] + \int V_{ext}(\mathbf{r}) n_0(\mathbf{r}) d^3r = E_0 \quad (3.23)$$

Following Levy and Lieb's definition of the functional $F[n(\mathbf{r})]$, we begin the proof of the second H-K theorem by considering an arbitrary wavefunction $\Psi'(\mathbf{r})$ that corresponds to an electron density $n'(\mathbf{r})$ influenced by an external potential $V'_{ext}(\mathbf{r})$. It is also assumed that an arbitrary wavefunction $\Psi'(\mathbf{r})$ minimizes the functional $F[n'(\mathbf{r})]$

such that

$$F[n'(\mathbf{r})] = \langle \Psi'_{\min}(\mathbf{r}) | T + U_{ee} | \Psi'_{\min}(\mathbf{r}) \rangle. \quad (3.24)$$

With this arbitrary external potential $V'_{ext}(\mathbf{r})$, the energy functional $E[n'(\mathbf{r})]$ is expressed as,

$$E[n'(\mathbf{r})] = F[n'(\mathbf{r})] + \int V'_{ext}(\mathbf{r}) n'(\mathbf{r}) d^3r \geq E_0. \quad (3.25)$$

For the summation of all the individual external potentials such that $V = \sum V_{ext}(\mathbf{r}_i)$, the energy functional $E[n'(\mathbf{r})]$ is equal to the sum of expectation values of the potential V , kinetic energy T and electron-electron interaction energy U_{ee} operators as follows,

$$E[n'(\mathbf{r})] = \langle \Psi_{\min}(\mathbf{r}) | V + T + U_{ee} | \Psi_{\min}(\mathbf{r}) \rangle \geq E_0. \quad (3.26)$$

Eqn. (3.26) completes the proof of Eqn. (3.22), and it is clearly noted that the total energy of the electronic system obtained from any trial electron density should always be higher than the ground state energy. The ground state energy is that obtained through the variational principle. The two H-K theorems demonstrate that it is useful to use the electron density rather than the wavefunctions. Unfortunately, the H-K theorems, themselves, do not say anything about the method of finding the exact form of the functional $F[n(\mathbf{r})]$.

3.3 Kohn-Sham (KS) equations

In the previous section, the importance of DFT was clearly defined through the two H-K theorems, but nothing has been mentioned about the simplicity of this *state-of-the-art* method compared to the other classical methods. In the following year (1965), Kohn and Sham [14] published the set of equations that were able to map the interacting many-body electronic system onto a system of non-interacting electrons moving in an effective potential [10]. The paper gave an assurance that DFT is an accessible ap-

proach, because the complicated many-body Schrödinger equation of a real electronic system is replaced by the self-consistent one-electron Kohn-Sham equations where the same electronic density as that of the fully-electronic interacting system is used. The paper [14] expressed the total energy functional as

$$E[n(\mathbf{r})] = T_{non}[n(\mathbf{r})] + E_{ext}[n(\mathbf{r})] + E_{Hartree}[n(\mathbf{r})] + E_{xc}[n(\mathbf{r})]. \quad (3.27)$$

The term $T_{non}[n(\mathbf{r})]$ is the kinetic energy of the non-interacting electron defined as

$$T_{non}[n(\mathbf{r})] = \frac{1}{2} \sum_i n_i \int \psi_i^*(\mathbf{r}) [-\nabla^2] \psi_i(\mathbf{r}) d\mathbf{r}, \quad (3.28)$$

where $\psi_i(\mathbf{r})$ is a one-electron KS wavefunction. Even though containing the effects of non-interacting particles, Eqn. (3.27) provides the exact ground state energy of the fully interacting system. The n_i in Eqn. (3.28) is the occupation number of i^{th} electronic state. The second term in Eqn. (3.27) is the well known external potential energy expressed as

$$E_{ext} = \int V_{ext}(\mathbf{r}) n(\mathbf{r}) d^3r, \quad (3.29)$$

whereas the third term is the Hartree potential energy defined as

$$E_{Hartree}[n(\mathbf{r})] = \frac{1}{2} \int \int \frac{n(\mathbf{r}_1)n(\mathbf{r}_2)}{|\mathbf{r}_1 - \mathbf{r}_2|} d^3r_1 d^3r_2 \quad (3.30)$$

respectively. $E_{Hartree}[n(\mathbf{r})]$ describes the Coulomb energy of a self-interacting continuous classical charge distribution of density $n(\mathbf{r})$. The term $E_{xc}[n(\mathbf{r})]$ in Eqn. (3.27) is the exchange-correlation energy functional. It simply carries the missing information when the interacting terms (V_{ee} and T_e) are replaced by non-interacting terms ($E_{Hartree}$ and $T_{non}[n(\mathbf{r})]$), respectively. The detailed description of $E_{xc}[n(\mathbf{r})]$ will follow in the next section.

Applying the variational principle to Eqn. (3.27) wrt. $n(\mathbf{r})$, bearing in mind that

$$\frac{\delta E[n(\mathbf{r})]}{\delta \psi_i^*(\mathbf{r})} = \frac{\delta T_{non}[n(\mathbf{r})]}{\delta \psi_i^*(\mathbf{r})} + \left[\frac{\delta \int V_{ext}(\mathbf{r})n(\mathbf{r})d^3r}{\delta n(\mathbf{r})} + \frac{\delta E_{Hartree}[n(\mathbf{r})]}{\delta n(\mathbf{r})} + \frac{\delta E_{xc}[n(\mathbf{r})]}{\delta n(\mathbf{r})} \right] \frac{\delta n(\mathbf{r})}{\delta \psi_i^*(\mathbf{r})} = 0, \quad (3.31)$$

subject to the constraint of orbital orthonormalization at a constant particle number, the KS equations can be derived [3]. Since Eqn. (3.27) has no electron-electron interactions, the effective potential $V_{eff}(\mathbf{r})$ is obtained [3, 6] based on the information arising from Eqn. (3.31) and expressed as

$$V_{eff}(\mathbf{r}) = V_{ext}(\mathbf{r}) + V_{Hartree}(\mathbf{r}) + V_{xc}(\mathbf{r}). \quad (3.32)$$

The first term on the right hand side of Eqn. (3.32) is the external potential $V_{ext}[n(\mathbf{r})]$. The second term $V_{Hartree}$ is the Hartree potential

$$V_{Hartree} = \frac{\delta E_{Hartree}[n(\mathbf{r})]}{\delta n(\mathbf{r})} = \int \frac{n(\mathbf{r}_2)}{|\mathbf{r}_1 - \mathbf{r}_2|} d^3r_2. \quad (3.33)$$

The third term V_{xc} is known to be the exchange-correlation potential. As stated earlier, since V_{xc} contains unknown quantum mechanical effects, it is then written as the functional derivative of $E_{xc}[n(\mathbf{r})]$ as

$$V_{xc} = \frac{\delta E_{xc}[n(\mathbf{r})]}{\delta n(\mathbf{r})}. \quad (3.34)$$

Having the effective potential $V_{eff}(\mathbf{r})$, the ground state electron density $n(\mathbf{r})$ can be obtained by solving the set of KS equations below:

$$\left[-\frac{1}{2}\nabla^2 + V_{eff}(\mathbf{r}) \right] \psi_i(\mathbf{r}) = \epsilon_i \psi_i(\mathbf{r}), \quad (3.35)$$

where ϵ_i is the one-electron KS energy eigenvalue. In addition, the KS wavefunction $\psi_i(\mathbf{r})$ must satisfy the normalization condition for the number of electrons $N =$

$\int \psi^*(\mathbf{r})\psi(\mathbf{r})d\mathbf{r}$ through the Lagrange multipliers.

Eqn. (3.35) is also solved self-consistently, just like the Hartree and Hartree Fock approximations, in an iterative way as follows:

1. Start with an initial guess of $n(\mathbf{r})$.
2. Calculate $V_{eff}(\mathbf{r})$, where the local density approximation or generalized gradient approximation is used for the exchange-correlation potential (V_{xc}) term.
3. The KS equations are solved to find the KS wavefunctions.
4. The new $n(\mathbf{r})$ is calculated from KS wavefunctions using Eqn. (3.7).
5. The process is repeated until the new $n(\mathbf{r})$ is equal to the initial $n(\mathbf{r})$ of the cycle. This means convergence has been reached.
6. Based on the convergence, various properties such as total energies, forces etc. can be computed.

Since the $E_{xc}[n(\mathbf{r})]$ functional is not known exactly, then an approximation is required in order to accurately perform practical calculations. In the next section, a brief description of the $E_{xc}[n(\mathbf{r})]$ functional is presented together with the formulation of the standard DFT approximations (LDA and GGA).

3.4 Exchange Correlation Energy Functional

A detailed description of the exchange-correlation interactions is clearly presented in the review paper published by Payne *et al.* [10]. As explained earlier, the exchange-correlation energy functional $E_{xc}[n(\mathbf{r})]$ is basically the collection of errors made when the non-interacting kinetic energy and Hartree potential are used. Even though $E_{xc}[n(\mathbf{r})]$ contributes little to the total energy functional $E[n(\mathbf{r})]$ of the system [17], it is important

in defining the accuracy of practical calculations. Up to now there has been no straightforward way of defining the $E_{xc}[n(\mathbf{r})]$ term except by means of approximation. There are already various approximations in DFT developed for the practical calculation of the $E_{xc}[n(\mathbf{r})]$ functional. The most popular used approximations are the local density approximation (LDA) [14] and generalized gradient approximation (GGA) [18]. But it must be mentioned that there are many more attempts to construct approximations, some are even complex than those presented in this thesis.

3.4.1 Local Density Approximation

The LDA proposed by Kohn and Sham [14] is the first approximation to be used in condensed matter pseudopotential calculations, and is the foundation of any development in the context of the exchange-correlation functionals. In the construction of LDA, it is assumed that the exchange-correlation energy per electron $\varepsilon_{xc}[n(\mathbf{r})]$ is local at point \mathbf{r} , and is the same as that for a uniform (homogeneous) electron gas $\varepsilon_{xc}^{hom}[n(\mathbf{r})]$ with the same density as the local density $n(\mathbf{r})$. Thus, for slowly varying densities, the exchange-correlation energy functional $E_{xc}[n(\mathbf{r})]$ in LDA is expressed as

$$E_{xc}^{LDA}[n(\mathbf{r})] = \int n(\mathbf{r})\varepsilon_{xc}[n(\mathbf{r})] d^3r, \quad (3.36)$$

where

$$\varepsilon_{xc}[n(\mathbf{r})] = \varepsilon_{xc}^{hom}[n(\mathbf{r})] \quad (3.37)$$

for homogeneous systems [3, 6, 14]. Eqn. (3.36) is only suitable for non-magnetic systems. For spin-polarized (magnetic) systems, the following local spin density approximation (LSDA) equation must be used [3, 6, 14]:

$$E_{xc}^{LSDA}[n^\uparrow(\mathbf{r}), n^\downarrow(\mathbf{r})] = \int d^3r n(\mathbf{r}) \varepsilon_{xc}^{hom}[n^\uparrow(\mathbf{r}), n^\downarrow(\mathbf{r})], \quad (3.38)$$

where $\varepsilon_{xc}^{hom}[n^\uparrow(\mathbf{r}), n^\downarrow(\mathbf{r})]$ is the exchange-correlation energy per electron, where electrons are spin polarized with different spin densities ($n^\uparrow(\mathbf{r}), n^\downarrow(\mathbf{r})$). But for our systems, Eqn. (3.36) is enough to yield the satisfactory results.

In practice, one can usually split the exchange-correlation energy per electron $\varepsilon_{xc}[n(\mathbf{r})]$ into exchange and correlation contributions as

$$\varepsilon_{xc}[n(\mathbf{r})] = \varepsilon_x[n(\mathbf{r})] + \varepsilon_c[n(\mathbf{r})]. \quad (3.39)$$

The derivation of the exchange energy per electron $\varepsilon_x[n(\mathbf{r})]$ contribution was first proposed in 1930 by Dirac [19] as

$$\varepsilon_x[n(\mathbf{r})] = -\frac{3}{4} \left(\frac{3n(\mathbf{r})}{\pi} \right)^{\frac{1}{3}}. \quad (3.40)$$

This contribution $\varepsilon_x[n(\mathbf{r})]$, can be evaluated exactly [3]. It is not possible to analytically determine the correlation energy per electron $\varepsilon_c[n(\mathbf{r})]$, and this therefore requires an approximation [3]. The first approximation of $\varepsilon_c[n(\mathbf{r})]$ for a uniform electron gas was performed by Ceperley and Alder in 1980 using the highly accurate numerical quantum Monte-Carlo method [20]. Based on the results obtained by Ceperley and Alder, several authors [21, 22, 23] made extra contributions by presenting an analytical parameterization of $\varepsilon_c[n(\mathbf{r})]$ using interpolation schemes. The most widely used parameterization is that published by Perdew and Zunger [23].

LDA performs very well for homogeneous electron systems [6]. It generally overbinds solids and molecular systems thereby underestimating the bond distances. LDA also predicts the structural properties of covalent, ionic and metallic bonded systems very well [6]. The success of LDA in a slowly varying system is partly due to the fact that it correctly satisfies the sum rule that the exchange-correlation hole integrates to exactly one removed electron [6, 10, 24, 25, 26]. The other reason is attributed to the fortuitous cancellation of errors occurring in the exchange and correlation energies

when they are added together, i.e. the LDA typically underestimates the $\varepsilon_c[n(\mathbf{r})]$ while it overestimates the $\varepsilon_x[n(\mathbf{r})]$ as shown by quantum Monte Carlo calculations for silicon [27]. LDA usually fails in systems where the density $n(\mathbf{r})$ has large variations throughout the entire region, due to incomplete cancellation of the electronic self-interaction [6]. The large variation in electron density greatly affects the nature of the bonding in any real material. LDA also severely underestimates the energy band gap in semiconducting materials. For instance, it predicts Germanium to be a metal. This is mainly attributed to the derivative discontinuity in the exchange-correlation potential in LDA [17]. Based on these shortcomings, it is clear that LDA requires major improvements.

3.4.2 Generalized Gradient Approximation

The first logical step taken to correct LDA was to incorporate gradient effects of electron density, known as the GGA. It is constructed in such a way that at any point \mathbf{r} in the system, the density $n(\mathbf{r})$ as well as its gradient $\nabla n(\mathbf{r})$ is considered, in order to account for the non-homogeneity of the true electron density ($n(\mathbf{r}) \neq \text{constant}$) [28]. It is constructed in practical terms by starting from the second order density gradient expansion for the exchange-correlation hole surrounding the electron in a system of slowly varying density, where the long range part is ignored in order to satisfy the sum rules on the exact hole that the LDA obeys [18, 28, 29, 30, 31, 32]. The GGA exchange-correlation energy functional is written in the form

$$E_{xc}^{GGA}[n^\uparrow(\mathbf{r}), n^\downarrow(\mathbf{r})] = \int n(\mathbf{r}) \varepsilon_{xc}[n(\mathbf{r})] f[n^\uparrow(\mathbf{r}), n^\downarrow(\mathbf{r}), \nabla n(\mathbf{r})^\uparrow(\mathbf{r}) \nabla n(\mathbf{r})^\downarrow(\mathbf{r})] d^3r, \quad (3.41)$$

where $\varepsilon_{xc}[n(\mathbf{r})]$ is the exchange-correlation energy density of a non-magnetic homogeneous electron gas as defined in LDA. In order for calculations to be practical, f and

$\varepsilon_{xc}[n(\mathbf{r})]$ must be parametrized with an analytic function.

It must be mentioned that there are various ways, in principle, in which the gradient $\nabla n(\mathbf{r})$ can be incorporated into E_{xc} , leading to different variants of GGA. In this thesis, the PBE version of the GGA functional developed by Perdew, Burke and Ernzerhof is among those used; thus, a brief overview on its construction is presented. Just as in LDA, one can split the exchange-correlation energy functional E_{xc}^{GGA} into its exchange E_x^{GGA} and correlation E_c^{GGA} energy contributions. The Perdew, Burke and Ernzerhof exchange energy $E_x^{GGA-PBE}$ part is constructed from the four main conditions presented in Ref. [32]. It is expressed as

$$E_x^{GGA-PBE}[n(\mathbf{r})] = \int d^3\mathbf{r} n(\mathbf{r}) \varepsilon_x^{hom}[n(\mathbf{r})] F_x(s), \quad (3.42)$$

where $\varepsilon_x^{hom}[n(\mathbf{r})]$ is equal to $-3k_F/4\pi$ and $F_x(s)$ is the enhancement factor which is the function of the reduced gradient of the density s . The enhancement factor is defined as

$$F_x(s) = 1 + k - \frac{k}{1 + \frac{\mu s^2}{k}}, \quad (3.43)$$

where $\mu = \beta(\pi^2/3)$, β is related to the second-order gradient expansion coefficient for exchange [33] and k is fitted as 0.804, obtained using the local Lieb-Oxford bound [34] (*Improved lower bound on the indirect coulomb energy*). Practically, one can recover the correct form of the uniform gas limit if $F_x(s) = 1$, provided $s = 0$. The Fermi wave vector $k_F(\mathbf{r})$ is defined as $k_F(\mathbf{r}) = (3\pi^2 n(\mathbf{r}))^{\frac{1}{3}}$.

The correlation energy E_c^{GGA} part is constructed from an extra three conditions, also presented in Ref. [32], and is given as

$$E_c^{GGA-PBE}[n^\uparrow, n^\downarrow] = \int d^3\mathbf{r} n(\mathbf{r}) \left[\varepsilon_c^{hom}(r_s, \zeta) + H(r_s, \zeta, t) \right]. \quad (3.44)$$

From equation (3.44), we notice that a gradient contribution H , clearly defined in

Ref. [32], is added to that of a homogeneous gas, and t is the dimensionless gradient of the density. The other parameters to be known are r_s and ζ defined as the local Seitz radius and the relative spin polarization $\zeta = (n^\uparrow - n^\downarrow)/n$, respectively.

GGA-PBE tends to improve typical binding energies, atomization energies and geometries of those systems that have large varying density $n(\mathbf{r})$, but only up to a certain limit [6, 32]. It also improves the energies, geometries, and dynamical properties of water molecules as compared to the experimental values [6].

The two functionals LDA and GGA-PBE fail to correctly describe systems with strongly localized d or f electrons. The failure is mainly caused by an incomplete cancellation of the Hartree self-interaction and the lack of integer discontinuity in the exchange and correlation energy. Various methods such as self-interaction-correction (SIC) [23], local density approximation with on-site coulomb energy (LDA+U) [35, 36] etc. have been developed to correct these shortcomings. The standard DFT exchange-correlation functionals also fail to correctly describe the effects of the non-local van der Waals forces (weak interlayer interactions) in complex, sparse and layered materials. For instance, the interlayer binding arising from the long-range dynamical charge-charge correlation interactions between the two fragments, is ignored by the LDA and GGA-PBE. In the next section, a brief overview of the methods that incorporate van der Waals interactions into DFT is presented.

3.4.3 The origin of van der Waals forces and derivation of the London dispersion energy term

The van der Waals (vdW) forces were named after Prof. Johannes Diderik van der Waals [37, 38] as an honour for deriving an equation of state that can accurately describe the behaviour of real gases. These forces are defined as the relatively soft, weak attraction interactions caused by the correlations in the rapidly fluctuating polarization between two fragments (atoms, molecules etc.) [39]. Fluctuating polarization can be

explained on the basis that in a molecule, electrons move randomly, keeping the polarity of a material wavering back and forth. This results in the instantaneous dipole fluctuations. The vdW forces play a crucial role in determining the properties of molecular systems, graphitic (layered) structures and many other sparse materials, and are investigated seriously in organic chemistry, surfaces science and more widely in condensed matter physics.

The vdW forces exist between two neutral systems when the following interactions do occur (originally summarized in Ref. [39]):

1. Permanent dipole-permanent dipole (Keesom) interactions between two largely separated systems.
2. Permanent dipole-induced dipole (Debye) interactions between two largely separated systems. The induced dipole is created when the fragment having the permanent dipole generates an electric field that is felt by the second neutral fragment. Therefore, the second fragment becomes polarized or rather develops an induced charge polarization, namely an induced dipole moment that leads to the weak attraction between the two materials.
3. Induced dipole-induced dipole interaction (dispersion interaction). This interaction is caused by the correlation effects of the charge distributions between two fragments. The correlation effects are possible when an instantaneous dipole fluctuation in one fragment induces an extra dipole in the other separated fragment or vice versa. This kind of interaction is also known as the London dispersion forces named after Fritz London [40], which are attractive in nature.

Some of the systems studied in this thesis, i.e. graphite, bilayer graphene and hydrogen molecule-surface interaction contain the Vdw interactions from Item 3, no permanent dipole is present. Thus, it is important to ensure that the DFT approach

applied to these systems does not neglect or ignore the effects of vdW dispersion interactions.

In 1930 London [40, 41, 42, 43] proposed an expression for dispersion interaction energy between two separated AB monomers as $E_{disp}^{AB} = -\frac{C_6^{AB}}{R^6}$, where R is the interatomic separation. The dispersion coefficients C_6 depend greatly on the elemental pair of monomers A and B. The dispersion interaction energy can be marked by being highly repulsive (growing exponentially) at the short range, but slowly decaying at the long range, separations. The London dispersion interaction energy is derived through the second-order perturbation theory. The word perturbation in this context can be defined as the Coulomb interaction between an electron and the nuclei of the two monomers. For a complete expression, the interacting terms defined through the perturbation are expanded using a Taylor expansion power series to obtain the term R^{-6} .

We present the derivation of the London dispersion energy term [40, 41, 42, 43] taking the simple hydrogen molecule H_2 as an example, where the two weakly interacting hydrogen atoms (h_A and h_B) are separated by the distance R , and are located along the z -axis. Firstly, it is assumed that $R \gg a_0$ (where a_0 is the Bohr radius) to avoid the overlap of the electronic densities arising from the isolated hydrogen atoms. This is only possible for two atoms with the same electronic spin, because for short range interactions ($R \approx a_0$) a high amount of repulsion occurs, while a weak attraction is experienced for long range interactions ($R \gg a_0$) due to weak vdW forces.

In this section, perturbation theory is used to estimate the long range interaction energy between the hydrogen molecules [44]. This is to consider the fact that molecules attract each other weakly at a relatively further distance, but strongly repel each other at a nearby distance. Thereby, Van der Waals forces are considered to be weaker than the covalent bonds.

Hamiltonian H of a hydrogen molecule is divided into unperturbed as well as per-

turbed contributions [44] as follows:

$$H = H_0^{h_A} + H_0^{h_B} + H^P, \quad (3.45)$$

where the Hamiltonians $H_0^{h_A}$ and $H_0^{h_B}$ contain the unperturbed information of two hydrogen atoms, and are defined as

$$H_0^{h_A} = -\frac{1}{2}\nabla_{h_A}^2 - \frac{1}{\mathbf{r}_{h_A}}, \quad (3.46)$$

and

$$H_0^{h_B} = -\frac{1}{2}\nabla_{h_B}^2 - \frac{1}{\mathbf{r}_{h_B}}, \quad (3.47)$$

where \mathbf{r}_{h_A} and \mathbf{r}_{h_B} are the electronic position vectors of hydrogen atoms h_A and h_B , measured wrt. to the protons. The last Hamiltonian term H^P in Eqn. (3.45) is the perturbation that contains the contributions of all the interactions, including the dipole-dipole interactions between the hydrogen atoms in the molecule, and is expressed as

$$H^P = \left(\frac{1}{R} + \frac{1}{R + \mathbf{r}_{h_A} - \mathbf{r}_{h_B}} - \frac{1}{\mathbf{r}_{h_A} - R} - \frac{1}{R + \mathbf{r}_{h_B}} \right). \quad (3.48)$$

It is clearly noted that the above expression greatly depends on the interatomic distance R . In order to estimate the dipole-dipole interaction energy between the two hydrogen atoms forming a molecule, the following assumptions are made:

1. Since $R \gg a_0$, the interaction between h_A and h_B is asymptotic, and therefore Eqn. (3.48) can be expanded into the higher powers of $1/R$.
2. The separation R is also assumed to be parallel to the molecule z -axis.

We further, expand the second, third and fourth terms in Eqn. (3.48) into higher powers of $1/R$ as

$$\frac{1}{R + \mathbf{r}_{h_B}} = \frac{1}{\sqrt{R^2 + \mathbf{r}_{h_B} + (2\mathbf{r}_{h_B} \cdot R)}} \quad (3.49)$$

since separation R is parallel to the molecule z -axis,

$$\frac{1}{R + \mathbf{r}_{h_B}} = \frac{1}{\sqrt{R^2 + \mathbf{r}_{h_B} + (2z_{h_B}R)}} = \frac{1}{R} \frac{1}{\sqrt{1 + 2z_{h_B}/R + (\mathbf{r}_{h_B}/R)^2}}, \quad (3.50)$$

also

$$\frac{1}{\mathbf{r}_{h_A} - R} = \frac{1}{R} \frac{1}{\sqrt{1 - 2z_{h_A}/R + (\mathbf{r}_{h_A}/R)^2}} \quad (3.51)$$

and lastly, using similar concept, the fourth term in Eqn. (3.48) is written as

$$\frac{1}{R + \mathbf{r}_{h_A} - \mathbf{r}_{h_B}} = \frac{1}{R} \frac{1}{\sqrt{1 + 2(z_{h_B} - z_{h_A})/R + (\mathbf{r}_{h_B} - \mathbf{r}_{h_A})^2/R^2}}. \quad (3.52)$$

The letters z_{h_A} and z_{h_B} are the z -axes of dipoles for h_A and h_B , respectively.

Eqns. (3.50), (3.51), and (3.52) can further be expressed as a Taylor expansion power series, retaining all the contributions up to the 2^{nd} order. For instance, Eqn. (3.51) can be expanded to

$$\frac{1}{\mathbf{r}_{h_A} - R} = \frac{1}{R} \left(1 - \frac{z_{h_A}}{R} - \frac{1}{2} \left(\frac{\mathbf{r}_{h_A}}{R} \right)^2 + \frac{3}{2} \left(\frac{z_{h_A}}{R} \right) \right). \quad (3.53)$$

The position vector \mathbf{r} can be expressed into co-ordinates of the form (x, y, z) such that $\mathbf{r}_{h_A} = x_{h_A} + y_{h_A} + z_{h_A}$ and $\mathbf{r}_{h_B} = x_{h_B} + y_{h_B} + z_{h_B}$. Substituting all the contributions obtained through the Taylor expansion power series into Eqn. (3.48), and after some mathematical simplification [44], H^P is reduced to

$$H^P = \frac{1}{R^3} (x_{h_A}x_{h_B} + y_{h_A}y_{h_B} - 2z_{h_A}z_{h_B}). \quad (3.54)$$

Eqn. (3.54) can also be derived using an instantaneous dipole moment on each

atom [44].

To obtain the dipole-dipole interaction energy (vdW interaction energy E^{vdW}), second order perturbation theory is applied to Eqn. (3.54) as a correction, in the form

$$E^{vdW} = \sum \frac{|\langle \Phi_0^{h_A} | H^P | \Phi_0^{h_B} \rangle|^2}{E_0 - E_{add}}, \quad (3.55)$$

where $\Phi_0^{h_A}$, $\Phi_0^{h_B}$ and $E_0 = -\frac{1}{a_0}$ are the ground state wavefunctions and energy of the unperturbed molecule, respectively. The ground state wavefunction $|\Phi_0\rangle$ can also take the form $|\Phi_0^{h_A}\rangle|\Phi_0^{h_B}\rangle = |100\rangle^{h_A}|100\rangle^{h_B}$. Where $|100\rangle^{h_A}$ is the state vector for hydrogen A. The summation in Eqn. (3.55) is for the interaction of two isolated hydrogen atoms for all excited states. The energy E_{add} in Eqn. (3.55) is the energy contribution arising from the interaction of two isolated hydrogen atoms for all excited states. Considering only the contribution from the lowest energy states, E_{add} is given by

$$E_{add} = E^{h_A} + E^{h_B} = -\frac{1}{2a_0} \left(\frac{1}{n_{h_A}^2} + \frac{1}{n_{h_B}^2} \right) = -\frac{1}{4a_0}, \quad (3.56)$$

where n is the number of states [44]. Eqn. (3.56) was evaluated by setting $n = 2$ to consider only the lowest energy states. The numerator of Eqn. (3.55) can be evaluated by considering the ground state properties of the wavefunction and also expressing \mathbf{r} into the co-ordinates form, yielding

$$\frac{1}{R^6} \langle 1, 0, 0; 1, 0, 0 | (x_{h_A}^2 x_{h_B}^2 + y_{h_A}^2 y_{h_B}^2 + 4z_{h_A}^2 z_{h_B}^2) | 1, 0, 0; 1, 0, 0 \rangle = \frac{6a_0^4}{R^6}. \quad (3.57)$$

Eqn. (3.57) is achieved on the basis that $\langle 1, 0, 0; 1, 0, 0 | (x_{h_A}^2) | 1, 0, 0; 1, 0, 0 \rangle = a_0^2$. Substituting Eqns. (3.56) and (3.57) into Eqn. (3.55), we obtain the final expression of vdW interaction energy [44]

$$E^{vdW} \approx -\frac{8a_0^5}{R^6} \approx -\frac{C_6}{R^6}. \quad (3.58)$$

Eqn. (3.58) can also be derived using the classical model of the vdW forces [45]. In this model, the derivation is based on the evaluation of the electric field created by the polarized atom and felt by the unpolarized second atom. Obviously the second atom will become polarized, meaning it will exhibit the induced dipole moment. In the classical model, the instantaneous dipole moment at each atom is realized and instead of the application of second order perturbation theory on the interaction, the potential energy is defined and expressed in terms of the dipole-dipole moments interactions.

The failure of DFT to accurately describe the properties of the systems that contain the vdW interactions, is the result of the missing of expression in Eqn. (3.58) in the Kohn-Sham equations. Therefore, DFT fails to yield reasonable R^{-6} asymptotic behaviour for the dispersion interaction between two largely separated systems. A simple correction for the shortcomings of DFT is to develop a model in such a way that an additional energy term which accounts for the missing long range attraction is incorporated into the Kohn-Sham equations.

To date, the theoretical methods developed to take vdW forces into account are empirical approach (termed DFT-D and DFT-D2) [46, 47, 48, 49, 50] which is based on the optimized positions of atom cores and first-principles method (termed vdW-DF) [51, 52, 53, 54, 55] which greatly depends on the electronic densities. Both approaches are certainly able to address the problem, but owing to the fact that our study is based on first principles calculations, it is imperative to pay attention to the vdW-DF implementation.

3.4.4 Approaches to incorporate van der Waals interactions into DFT

In order to incorporate vdW forces into the DFT framework, where the correction is based on the electron charge density $n(\mathbf{r})$, Rutgers-Chalmers collaborators led by H. Rydberg proposed the method [51, 52, 53, 54, 55] that slightly modifies the Kohn-Sham exchange-correlation energy functional $E_{xc}[n(\mathbf{r})]$ term. In this scheme, the $E_{xc}[n(\mathbf{r})]$ splits into three terms as follows:

$$E_{xc}[n(\mathbf{r})] = E_x^{Sl}[n(\mathbf{r})] + E_c^l[n(\mathbf{r})] + E_c^{nl}[n(\mathbf{r})], \quad (3.59)$$

where $E_x^{Sl}[n(\mathbf{r})]$ is a semi-local exchange energy, and is taken from GGA functionals as $E_x^{GGA-PBE}[n(\mathbf{r})]$ defined from Ref. [32] or as a revised Perdew Burke Ernzerhof (revPBE) exchange energy functional $E_x^{revPBE}[n(\mathbf{r})]$ that also accounts for the gradient of the density proposed by Zhang and Yang [59]. The second term $E_c^l[n(\mathbf{r})]$ in Eqn. (3.59) is a local correlation energy, and approaches the LDA in the limit of a slowly varying electron gas. The last term of Eqn. (3.59) $E_c^{nl}[n(\mathbf{r})]$ is the non-local correlation energy term, and it takes into account the long range interactions that basically create the vdW forces. The construction of the $E_c^{nl}[n(\mathbf{r})]$ term is usually based on the following primary argument: *the long range interaction terms are less sensitive to the details of the dielectric functions (ϵ) of the system; therefore, this allows the simple approximations for the dielectric function to be made.* The approximations for the dielectric function predict the polarization properties of materials.

The complete derivation of a non-local correlation energy term $E_c^{nl}[n(\mathbf{r})]$ specifically for layered systems is found in the Refs. [51, 52]. Its final form is given in terms of dielectric function ϵ as

$$E_c^{nl}[n(\mathbf{r})] = \int_0^\infty \frac{du}{2\pi} \ln |\det (1 + \epsilon^{-1}(\nabla\epsilon - \epsilon\nabla) \cdot \nabla G)|, \quad (3.60)$$

where G is the Coulomb Green's function defined in terms of the inter-electronic

Coulomb potential V as

$$G = -\frac{V}{4\pi}. \quad (3.61)$$

The symbol u in Eqn. (3.60) represents the imaginary frequency. It is difficult to directly evaluate Eqn. (3.60) because of the combination of trace and logarithm; therefore, it can only be computed with a specific algorithm. Rydberg *et al.* [52] presented an algorithm for the determinant that scales linearly with the size of the system at a given density $n(r)$. In this algorithm, the integration is singled out and replaced by the expansion of the logarithm into the second order differential equation. Applying this algorithm to the two surfaces separated by the distance d , the Lifshitz limit expression [60, 61] is recovered, in such a way that

$$E_c^{nl}[n(\mathbf{r})] = A \int_0^\infty \frac{du}{2\pi} \frac{d^2k}{(2\pi)^2} \ln \left| 1 - \left(\frac{\epsilon_b - 1}{\epsilon_b + 1} \right)^2 e^{-2kd} \right| + 2\gamma_{nl}, \quad (3.62)$$

where A is the surface lateral area and ϵ_b is the bulk dielectric function. The separation d is the distance between the surfaces. The letter k is the wave vector parallel to the surfaces perpendicular to the z direction and the symbol γ_{nl} is the long range correlation contribution to the surface tension of a surface. The surface tension is given by,

$$\gamma_{nl} = \frac{[E_c^{nl}(d \rightarrow \infty) - E_c^{nl}(0)]}{2A}, \quad (3.63)$$

where $E_c^{nl}(0)$ approaches zero for a system with $d=0$, i.e. in a homogeneous electron gas system limit. To complete (3.62), one must have the knowledge of ϵ . In this theory, ϵ can only be approximated using a simple Plasmon-pole model [52] as,

$$\epsilon(z, \omega) = 1 + \omega_p^2(z) \left[u^2 + \frac{[v_F(z)qk]^2}{3} + \frac{q_k^4}{4} \right]^{-1}, \quad (3.64)$$

where $\omega = iu$ is the imaginary frequency. The Plasmon frequency $\omega_p^2(z)$ can be defined

as

$$\omega_p^2(z) = \frac{4\pi n(z)e^2}{m} \quad (3.65)$$

and the Fermi velocity as

$$v_F(z) = \frac{(3\pi^2 n(z))^{1/3}}{m}. \quad (3.66)$$

Both velocity and frequency are the functions of the local density $n(z)$ along the z direction. The quantity q_k^2 mimics the 3-D wave vector, which gives $\epsilon(z, iu)$ its k dependence.

The complete form of the correlation energy functional $E_c[n(\mathbf{r})]$ that contains the vdW or non-local interactions correction based on the electronic densities of the fragments, proposed by Rydberg *et al.* [51], is also known as the *van der Waals density functional* (vdW-DF version). The vdW-DF correlation combined with revPBE exchange was first implemented within the plane wave pseudopotential DFT code called dacapo [62]. The test of this version was performed on three graphitic structures, viz. graphite, boron-nitride and molybdenum disulfide MoS₂. The computed interlayer binding energies and equilibrium interlayer distances were found to be in good agreement with experimental results [51, 52]. Rydberg *et al.* [51] concluded that the vdW-DF-revPBE version should replace the GGA functional in the studies of graphitic systems.

In the following year (2004), M. Dion and the same co-workers who published Refs. [51, 52, 53], developed the vdW-DF correlation in such a way that it is not restricted to a certain type of material [54, 55]. Since the results obtained in this thesis are derived from this developed vdW-DF scheme, we therefore give a detailed discussion of its construction. In this scheme, the full exchange-correlation energy functional still splits into three contributions just like in Eqn. (3.59) above and also in Refs. [51, 52, 53]:

$$E_{xc}[n(\mathbf{r})] = E_x^{Sl}[n(\mathbf{r})] + E_c^l[n(\mathbf{r})] + E_c^{nl}[n(\mathbf{r})]. \quad (3.67)$$

Our discussion still focuses on the derivation of the last term of Eqn. (3.67), as it was stated earlier that the vdW forces exist in the non-local correlation interaction part. The first and second terms of Eqn. (3.67) are still obtained in the same manner as defined earlier. The simplest form of non-local correlation energy E_c^{nl} for general geometries can be written as

$$E_c^{nl} = \frac{1}{2} \int dr \int dr' n(\mathbf{r}) \Phi(\mathbf{r}, \mathbf{r}') n(\mathbf{r}'), \quad (3.68)$$

where $\Phi(\mathbf{r}, \mathbf{r}')$ is the kernel that greatly depends on the distance $(\mathbf{r} - \mathbf{r}')$. The Kernel relates the density $n(\mathbf{r})$ to that of $n(\mathbf{r}')$. We see that in order to correctly evaluate Eqn. (3.68), the value of $\Phi(\mathbf{r}, \mathbf{r}')$ must be known, and this is the central part of the vdW-DF scheme. The kernel is derived within the adiabatic connection theorem, whereby the Plasmon-pole model is utilized to approximate the dielectric function ϵ . Interestingly, it does not contain any adjustable parameter [53, 54].

3.4.5 Derivation of the kernel $\Phi(\mathbf{r}, \mathbf{r}')$

To derive the kernel, we still need to express the non-local correlation energy E_c^{nl} by a simple approximation for the dielectric functions ϵ (the reason for this is the same as that given earlier). Firstly, the $E_{xc}[n(\mathbf{r})]$ term in Eqn. (3.35) is modified through the adiabatic connection approach such that the electronic Coulomb interaction can be easily regulated (continuously turned on and off) [56, 57]. The modified E_{xc} due to the introduction of coupling constant λ is expressed as

$$E_{xc} = \int \frac{n(\mathbf{x}) n_{xc}^\lambda(\mathbf{x}, \mathbf{x}')}{\mathbf{r} - \mathbf{r}'} d\lambda d^4r d^4r', \quad (3.69)$$

where $n(\mathbf{x})$ and $n_{xc}(\mathbf{x}, \mathbf{x}')$ are the electronic and exchange-correlation hole densities that greatly depend on the temporal coordinates \mathbf{x} and \mathbf{x}' [54, 55]. To express E_{xc} in terms of the dielectric functions ϵ , the fluctuation-dissipation theorem [58] and full potential

approximation (FPA) [54, 55] are applied to Eqn. (3.69) such that E_{xc} becomes

$$E_{xc}^{FPA} = \int \frac{du}{2\pi} Tr[\ln(1 - \tilde{\chi}V)] - \int n(\mathbf{r})drV_0, \quad (3.70)$$

where $\tilde{\chi}$ is the density response function of the system. The last term is the self-interaction energy. The inter-electronic Coulomb potential V in Eqn. (3.70) is scaled by coupling constant λ such that

$$V_\lambda = \frac{\lambda}{\mathbf{r} - \mathbf{r}'} \quad (3.71)$$

Since it is difficult to know the coupling constant λ that corresponds to a specific density response function $\tilde{\chi}$, the FPA is applied to Eqn. (3.69) in accordance with which $\tilde{\chi}_\lambda \approx \tilde{\chi}_{\lambda=1}$. The fluctuation-dissipation theorem enables us to relate the E_{xc} to the density response function $\tilde{\chi}$ of the system. The purpose of $\tilde{\chi}$ is to introduce the dielectric functions ϵ as follows:

$$\tilde{\chi} = \nabla \frac{\epsilon - 1}{4\pi} \nabla. \quad (3.72)$$

Substituting Eqn. (3.72) into Eqn. (3.70), the exchange-correlation energy functional E_{xc} is simply related to dielectric functions ϵ in this form

$$E_{xc}^{FPA} = \int \frac{du}{2\pi} Tr[\ln(-\nabla \frac{\epsilon}{4\pi} \nabla)V] - \int n(\mathbf{r})drV_0. \quad (3.73)$$

It must be known that FPA ensures that the non-local correlation energy only accounts for long range interactions, and therefore vanishes for a system of slowly varying density limits to avoid the double counting in the LDA correlation energy. This implies that, in the case of homogeneous electron gas, Eqn. (3.73) reduces to

$$E_{xc}^{FPA-homo} = \int \frac{du}{2\pi} Tr[\ln\epsilon] - \int n(\mathbf{r})drV_0, \quad (3.74)$$

where the relation $\nabla^2 V = -4\pi$ is applied [54, 55]. Eqn. (3.74) is only applicable for LDA correlation (see Eqn. (3.67)). Following this information, one can obtain the non-local correlation energy expression E_c^{nl} by subtracting Eqn. (3.74) from Eqn. (3.73), such that

$$E^{nl} = \int \frac{du}{2\pi} \text{Tr} \left[\ln \left(1 - \left(1 - \frac{1}{\epsilon} \right) - \frac{\tilde{\chi} V}{\epsilon} \right) \right]. \quad (3.75)$$

This equation is only applicable for long range interactions; however up to this point it cannot be evaluated straight away because of the combination of trace and logarithm functions. We further use the algorithm that can expand the logarithm into the second order derivatives in terms of quantity $S = 1 - \frac{1}{\epsilon}$. Applying this quantity S into Eqn. (3.75), and definitely after some algebraic performance,

$$E_c^{nl} = \int \frac{du}{4\pi} \text{Tr} \left[S^2 - \left(\frac{\nabla S \cdot \nabla V}{4\pi e^2} \right)^2 \right]. \quad (3.76)$$

The significance of Eqn. (3.76) is that it is not restricted to specific geometries. To evaluate Eqn. (3.76), an accurate approximation for quantity S as a functional of the density $n(\mathbf{r})$ is required, which is possible through the use of a simple Plasmon-pole model. In the simple Plasmon-pole model, the quantity S takes the general form of

$$S_{\mathbf{q}}(u) = \frac{\omega_p^2}{u^2 + \omega_q^2}, \quad (3.77)$$

where $u = -i\omega$ is the imaginary frequency, whereas ω_p^2 is still the Plasmon frequency approximated by $q^2[2h(y)q/q_0]^{-1}$, where $h(y)$ is defined as

$$h(y) = 1 - e^{-\gamma y^2}. \quad (3.78)$$

The symbol γ is a fitted parameter where its typical value is $4\pi/9$. The dispersion function ω_q^2 can be easily affected by excitations such as the electron-hole pairs, where one of them is excited above the Fermi surface, and, also, by a collective motion of an

electron gas causing a long wave excitations.

To approximate Eqn. (3.77), the value of ω_q^2 needs to be known, but this can only happen if the value of q_0 is to be defined first. Dion et al. [54] defined q_0 based on the knowledge of exchange-correlation energy per electron $\epsilon_{xc}(\mathbf{r})$ and exchange energy per electron $\epsilon_x^{LDA}(\mathbf{r})$ for homogeneous electron gas as

$$q_0 = \frac{\epsilon_{xc}(\mathbf{r})}{\epsilon_x^{LDA}(\mathbf{r})} k_F(\mathbf{r}), \quad (3.79)$$

where the Fermi wave vector is still given by $k_F(\mathbf{r}) = (3\pi^2 n(\mathbf{r}))^{\frac{1}{3}}$.

For implementation purposes, Eqn. (3.77) can be expressed in the form of a plane wave representation as

$$S_{\mathbf{q},\mathbf{q}'} = \frac{1}{2}[\tilde{S}_{\mathbf{q},\mathbf{q}'} + \tilde{S}_{-\mathbf{q}',-\mathbf{q}}], \quad (3.80)$$

where

$$\tilde{S}_{\mathbf{q},\mathbf{q}'} = \int d\mathbf{r} e^{-i(\mathbf{q}-\mathbf{q}')\cdot\mathbf{r}} \frac{\omega_p^2}{[\omega + \omega_{\mathbf{q}}(\mathbf{r})][-\omega + \omega_{\mathbf{q}'}(\mathbf{r})]} \quad (3.81)$$

provided the next symmetry constraints fully defined in Ref. [54] are obeyed. Equation (3.80) holds only if the large frequency f-sum rule is obeyed $S_{\mathbf{q},\mathbf{q}'} \rightarrow -(4\pi e^2/m\omega^2)n_{\mathbf{q}-\mathbf{q}'}$, and for large q , the known self-correlation must be produced as long as $\int_{-\infty}^{\infty} S_{\mathbf{q},\mathbf{q}'} \rightarrow 8\pi^2 N e^2/q^2$, where N is the number of electrons. Equation (3.76) can be expressed in a plane wave representation form based on the information gathered from Eqns. (3.80) and (3.81):

$$\tilde{E}_c^{nl} = \int \frac{du}{4\pi} \sum_{\mathbf{q},\mathbf{q}'} [1 - (\hat{q} \cdot \hat{q}')^2] S_{\mathbf{q},\mathbf{q}'} S_{\mathbf{q}',\mathbf{q}}. \quad (3.82)$$

It can be seen that this equation is nearly transformed into Eqn. (3.60); what is left is to have a complete final expression for kernel Φ . The completed derivation for Φ is available in Ref. [55]. The final asymptotic form of the kernel is given in terms of

dispersion functions ω_0 as

$$\Phi(\mathbf{r}, \mathbf{r}') = -\frac{3}{2} \frac{1}{R^6} \frac{1}{\omega_0 \omega'_0 (\omega_0 + \omega'_0)} = -\frac{C_6}{R^6}, \quad (3.83)$$

where the distance $R = |\mathbf{r} - \mathbf{r}'|$ and the dispersion function $\omega_0 = \frac{q_0}{\lambda}$. It can be noted that Eqn. (3.83) is similar to that of the London dispersion energy term, derived using 2^{nd} order perturbation theory. Eqn. (3.83) can be substituted into Eqn. (3.68) to yield a non-local correlation energy term known as the vdW-DF correlation energy function.

The final form of developed vdW-DF correlation combined with revPBE exchange [59] was also implemented within the dacapo code [62]. The binding energies and interlayer distances for Ar and Kr dimers were computed to test its (vdW-DF-revPBE) performance. Even though the computed interlayer separations are slightly larger than the experimental data for such systems (see Fig. 2 of Ref. [54]), the authors were satisfied that the vdW-DF-revPBE scheme is a promising exchange-correlation functional for vdW bonded materials.

Despite the ability of vdW-DF-revPBE to predict the correct properties of vdW interacting systems, the noted overestimation of the interlayer distance is a problem. This shortcoming is attributed to the use of revPBE exchange, which is repulsive in nature. To resolve this problem, *Lee et al.* [63] proposed the second version of the vdW-DF correlation functional, referred to as vdW-DF2. In the vdW-DF2 version, a large-N asymptote gradient correction is used during the derivation of the vdW kernel (see Eqn. (3.83)), and it also takes the form

$$E_c^{nl} = \frac{1}{2} \int dr \int dr' n(\mathbf{r}) \Phi(\mathbf{r}, \mathbf{r}') n(\mathbf{r}'). \quad (3.84)$$

The vdW-DF2 version employs the refit Perdew-Wang (PW86R) [30, 64] exchange functional which does not contain the spurious exchange binding, and correctly mimics the Hartree-Fock exchange energy. To test the performance of the vdW-DF2-PW86R

exchange-correlation version, the binding energy and interlayer separation for graphite were computed. It was noted that vdW-DF2-PW86R shortens the interlayer distance by 2% compared to that of vdW-DF-revPBE [63]. In the case of binding energy calculations, no substantial differences were noted when comparing the two functionals.

In the same year, Cooper [65] proposed the exchange functional referred to as Cooper exchange ($C09_x$) in order to replace the highly repulsive revPBE exchange. The $C09_x$ exchange belongs to the GGA-PBE exchange developed by Perdew, Burke and Ernzerhof, and is defined as

$$E_x^{C09} = \int d^3r \epsilon_x^{unif}(n) F_x(s). \quad (3.85)$$

The $C09_x$ exchange depends greatly on the introduced enhancement factor $F_x(s)$, which is the function of gradient density $s = \nabla n / 2k_F n$. The typical $F_x(s)$ for $C09_x$ obeys the following two specific constraints:

1. For slowly varying densities, in the limit $s \rightarrow 0$, the functional approaches the gradient expansion approximation GEA [66] to reduce the short range exchange repulsion. In this regard, the enhancement factor $F_x(s)$ takes the form

$$F_x^{GEA}(s) = 1 + \mu s^2, \quad (3.86)$$

where $\mu = 0.0864$, obtained from Ref. [66].

2. The proposed $C09_x$ approach the revPBE exchange upper bound of 2.245 in the large gradient density s -limit [59] asymptotically. This is to ensure that the $C09_x$ exchange becomes compatible with the non-local vdW-DF correlation as the revPBE exchange does.

Based on these two constraints, the enhancement factor $F_x(s)$ for $C09_x$ exchange of Eqn. (3.85) is expressed in this form,

$$F_x(s) = 1 + \mu s^2 e^{-\alpha s^2} + k(1 - e^{-\alpha s^2/2}), \quad (3.87)$$

with the fitted parameters $\mu = 0.0617$, $k = 1.245$ and $\alpha = 0.0483$.

The non-local vdW-DF correlation combined with C09_x exchange is referred to as vdW-DF-C09_x, and was first implemented within the Abinit plane wave pseudopotential code [67]. To test the performance of vdW-DF-C09_x, the interaction energies and interlayer separations for s22 database structures [68] were calculated. It was noted that vdW-DF-C09_x is in good agreement with the benchmark CCSD(T) and SAPT(DFT) calculations [69]. The test was also carried out for the graphite structure. It was found that vdW-DF-C09_x gives a short interlayer separation of 3.28 Å, which is within 2% of the experimental value of 3.35 Å, [70] whereas the vdW-DF-revPBE gives 3.675 Å [65]. In the case of interlayer binding energies for graphite, it was also noted that vdW-DF-C09_x gives -59 kcal/mol which is perfectly in agreement with the experimental value of -52±10 kcal/mol [70] as compared to -39 kcal/mol predicted by vdW-DF-revPBE [65]. It was concluded that, the C09_x exchange is an appropriate functional to study the sparse material (weakly bounded material).

The C09_x exchange is also compatible with vdW-DF2 correlation, and they are collectively called the vdW-DF2-C09_x exchange-correlation functional. Benchmark tests for various versions of LDA, GGA-PBE, vdW-DF-revPBE, vdW-DF2-PW86R, vdW-DF-C09_x and vdW-DF2-C09_x were computed by Hamada *et al.* [71, 72] on graphite and bilayer graphene. In this thesis, similar tests were performed using a quantum espresso package [73] and are presented in chapter IV.

3.5 Plane waves formulation of the Kohn-Sham equations

In this section, we present an overview of the formulations of plane wave basis sets and atomic pseudopotential methods, which are one way to solve the Kohn-Sham equations.

Furthermore, the importance of the projector augmented wave (PAW) approach, which is the generalization of ultrasoft and linear augmented plane waves techniques, is discussed.

From a solid state physics point of view, it is known that an ordered real crystal consists of an enormous number of electrons (approximately 10^{23}) moving in an electric field generated by a large number of ions. In electronic structure calculations, the plane wave pseudopotential approximation uses Bloch's theorem to reduce these extremely large number of electrons to at least half the number of electrons in the unit cell, exploiting the periodicity of the crystal.

3.5.1 Bloch's theorem

According to Bloch's theorem [74], the electronic wavefunctions $\Psi_i(\mathbf{r})$ for a periodic solid can be expressed in the form of a plane wave $e^{i\mathbf{k}\cdot\mathbf{r}}$ times a cell periodic function $g_i(\mathbf{r})$ as

$$\Psi_i(\mathbf{r}) = e^{i\mathbf{k}\cdot\mathbf{r}} g_i(\mathbf{r}). \quad (3.88)$$

The function $g_i(\mathbf{r})$ can be expressed in a Fourier series expansion using a discrete plane waves set whose wave vectors are reciprocal lattice vectors \mathbf{G} of the periodic crystal

$$g_i(\mathbf{r}) = \sum_{\mathbf{G}} c_{i,\mathbf{G}} e^{i\mathbf{G}\cdot\mathbf{r}}. \quad (3.89)$$

The reciprocal lattice vectors \mathbf{G} are defined using a Bravais lattice vector \mathbf{R} as $\mathbf{G}\cdot\mathbf{R} = 2\pi n$, where n is an integer number. Each electronic wavefunction $\Psi_i(\mathbf{r})$ can now be expressed as the sum of all plane waves [74],

$$\Psi_i(\mathbf{r}) = \sum_{\mathbf{G}} c_{i,\mathbf{k}+\mathbf{G}} e^{i(\mathbf{k}+\mathbf{G})\cdot\mathbf{r}}. \quad (3.90)$$

The $c_{i,(\mathbf{k}+\mathbf{G})}$ coefficients for the plane waves basis set need to be solved self consistently, and greatly depend on the choice of plane wave kinetic energy cut-off (see the next section). Eqn. (3.90) shows that by using Bloch's theorem, each electronic wavefunction of a periodic cell can be obtained for each \mathbf{k} -point in the first Brillouin zone. Thus, the Bloch theorem makes it possible to map the problem of solving KS equations onto one of finding a number of electronic wavefunctions, depending on the number of \mathbf{k} -points in the first Brillouin zone of a periodic cell. This implies that the correct properties of a crystal can be obtained, to a desired numerical accuracy, from the electronic wavefunctions provided the number of \mathbf{k} -points and the energy cut-off are large enough.

3.5.2 Plane wave kinetic energy cut-off

The expansion of the electronic wavefunction as the sum of a plane wave basis set causes the KS equations to take a simple reciprocal space representation form. This is obtained by substituting Eqn. (3.90) into the KS equations (3.35) and integrating over region \mathbf{r} [10] as

$$\sum_{\mathbf{G}'} \left[\frac{1}{2} |\mathbf{k} + \mathbf{G}'|^2 \delta_{\mathbf{G}\mathbf{G}'} + V_{ion}(\mathbf{G} - \mathbf{G}') + V_H(\mathbf{G} - \mathbf{G}') + V_{xc}(\mathbf{G} - \mathbf{G}') \right] c_{i,\mathbf{k}+\mathbf{G}'} \quad (3.91)$$

$$= \varepsilon_i c_{i,\mathbf{k}+\mathbf{G}'}$$

The descriptions of local potentials (V_{ion} , V_H and V_{xc}) in Eqn. (3.91) are in terms of their Fourier transformation components. The solution of Eqn. (3.91) is obtained by diagonalization of the Hamiltonian matrix represented in the brackets. Each plane wave with coefficients $c_{i,(\mathbf{k}+\mathbf{q})}$ has the corresponding kinetic energy $\frac{1}{2} |\mathbf{k} + \mathbf{G}'|^2$. The kinetic energies in Eqn. (3.91) are diagonally aligned in a matrix. The size of the matrix is

determined by the kinetic energy cut-off

$$E_{cut} = \frac{1}{2}|\mathbf{k} + \mathbf{G}_{max}|^2. \quad (3.92)$$

To solve Eqn. (3.91) efficiently using iterative techniques encourages development for DFT code. In practical calculations, the size of the kinetic energy cut-off is always moderate because the description of rapidly oscillating wavefunctions of electrons in the core region that require more plane waves is addressed by pseudopotential approximation.

3.5.3 k-point sampling

Mapping out the Brillouin zone (BZ) by a continuous set of \mathbf{k} -points throughout the reciprocal space plays a role in determining the properties of real material systems. From the Bloch theorem (see Eqn. (3.90)), it is noted that a finite number of wavefunctions in the unit cell can be considered for an infinite number of \mathbf{k} -points within the first BZ. Therefore, plane waves basis sets are required to represent the wavefunctions at an infinite number of \mathbf{k} -points within the BZ, such that an infinite number of electronic states in a crystal is transformed into a finite number of electronic states in a unit cell.

First principles codes require functions to be integrated over the BZ in order to calculate electronic properties. These integrations averaged over the BZ have the form:

$$F(\mathbf{r}) = \frac{\Omega}{(2\pi)^3} \int_{BZ} f(\mathbf{k}) d^3k \quad (3.93)$$

where $f(\mathbf{k})$ is the Fourier transformation of functions $F(\mathbf{r})$ and Ω is the volume of the unit cell. The functions are completely symmetric and periodic in k -space. The Fourier transform can be expressed in terms of $A_m(\mathbf{k})$ as follows:

$$f(\mathbf{k}) = f_o + \sum_{m=1} A_m(\mathbf{k}) \quad (3.94)$$

where $A_m(\mathbf{k})$ is the transformation expression defined as

$$A_m(\mathbf{k}) = \sum e^{i\mathbf{k}\cdot\mathbf{r}}. \quad (3.95)$$

The sum in Eqn. (3.94) is taken over all \mathbf{r} vectors related by the operations of the lattice point group, and can be truncated because of the exponential decrease of the terms at large \mathbf{r} . Using a discrete set of special points in the BZ, the integration sum (see Eqns. (3.94), (3.93)) can be calculated over all filled bands, since the functions have identical values around any given point. One such method is that proposed by Monkhorst and Pack [75]. This special \mathbf{k} -point scheme has been developed to use a few \mathbf{k} -points at a low computational cost for a given accuracy. The scheme [75] is an unbiased method for choosing the set of \mathbf{k} -points, for sampling the BZ in a fractional co-ordinate form in a rectangular grid of points (\mathbf{k}_x , \mathbf{k}_y , \mathbf{k}_z) based on

$$\mathbf{k}_{n_1 n_2 n_3} = \sum_{i=1}^3 \frac{2n_i - N_i - 1}{2N_i} \mathbf{G}_i. \quad (3.96)$$

Eqn. 3.93 integrates exactly over the identical points, if the Fourier components for each $f_i(\mathbf{k})$ only extend to $N_i R_i$ in each direction. Based on this, the total energy of the solid systems can be calculated with a very small number of special \mathbf{k} -points. The errors arising during calculations can be reduced by choosing a large set of Monkhorst and Pack [75] \mathbf{k} -points. For example, metals have partially filled bands, so that their integrals over the BZ are given as

$$I = \int_{BZ} S(E(\mathbf{k}) - E_F) f(\mathbf{k}) d^3\mathbf{k} \quad (3.97)$$

where $E(\mathbf{k})$ is the energy of bands and $S(E(\mathbf{k}) - E_F)$ is the unit step function with a drop off at the Fermi energy. Eqn. (3.97) is considered to be a density of states calculation. The sharp drop in electron occupation just below the Fermi level would

require a very high number of \mathbf{k} -points to correctly define the Fermi surface and to reduce the amount of errors in the total energy that might occur during the sampling of the Brillouin zone. In 1989, Methfessel and Paxton [76] proposed a smearing method for integration of the BZ, specifically for metals. The method is based on the smearing approximants to smoothen the sharp drop in electron occupation just below the Fermi level during the sampling of the BZ. The sampling converges exponentially, utilizing a fairly small number of \mathbf{k} -points.

3.6 The atomic pseudopotential approximation

The wave functions in materials vary with bonding. In the core region around the nucleus, the wavefunction oscillates rapidly, whereas in the valence (bonding) region they are smooth. This variation seriously affects the accurate description of the nature of bonding by electronic structure methods. In the previous section, it has been shown that Bloch's theorem enables the electronic wavefunction to be expanded as the sum of plane waves. In *ab initio* electronic structure calculations, that use the pseudopotential (PPS) approximation, only the valence wavefunctions are expanded because the core electrons are considered to be inert (unreactive). The inert electrons would require too many plane waves to expand the core orbitals due to the very deep potential in this region. Therefore, the computing time would be too costly and too much memory would be occupied.

The PPS approximation does not completely ignore the inert core electrons, but replaces the electrostatic potential ($-\frac{Z}{r}$) that occurs during their interactions with the nuclear charge by a weaker ionic PPS V_{pseudo} within a core region of cut-off radius r_c (see Fig. 3.1). The core radius r_c is usually chosen to be approximately half the nearest-neighbour distance.

The design of PPS is based on a set of fictitious pseudo wavefunctions rather than

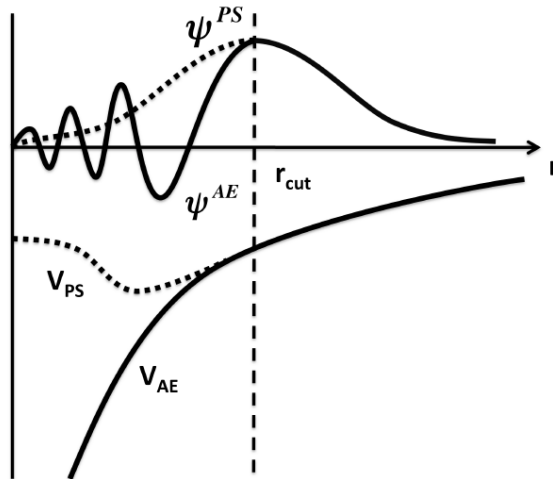


Figure 3.1: Schematic illustration of all-electron (solid lines) and pseudo electron (dashed lines) potentials and their corresponding wavefunctions. The radius at which all-electron and pseudo electron values match is designated r_{cut} . Taken from Ref. [10]

the true all-electron (AE) wavefunctions. The advantage of PPS is that, in the region occupied by the core electrons, its pseudo wavefunction oscillates smoothly compared to the high rapid oscillation of the AE wavefunctions as shown in Fig. 3.1. This rapid oscillation of the AE wavefunctions is due to the strong (deep) ionic potential well in this region. This behaviour in the core region is necessary to ensure the orthogonality between the valence and core wavefunctions, to obey the Pauli exclusion principle.

The PPS are constructed in such a way that they reproduce the effects of inert core electrons usually felt by the valence electrons. But it is advisable to test the pseudopotential, to ensure that all the salient features of a valence electron in a material, including relativistic effects [84, 10] are well described.

3.6.1 Requirements for pseudopotential construction

There are various methods available for PPS generation. The most popular PPS are norm conservation [77, 78], ultrasoft [79] and projector augmented wave (PAW) [81]. In order for these PPS to be accurate and reliable, the following criteria must be obeyed

during their generation:

1. The PPS used in electronic structure calculations must be generated from AE density-functional calculations for spherical atoms such that the generation satisfies

$$\int_0^{r_c} \Psi^{AE}(\mathbf{r})\Psi^{AE*}(\mathbf{r}) = \int_0^{r_c} \Psi^{PS}(\mathbf{r})\Psi^{PS*}(\mathbf{r}), \quad (3.98)$$

where $\Psi^{AE}(\mathbf{r})$ is the all-electron wavefunction and $\Psi^{PS}(\mathbf{r})$ is the pseudo wavefunction. Eqn. (3.98) guarantees that the AE and pseudo wavefunctions outside the core region are equal. This property is for norm conserving pps [77, 78]. To ensure the accuracy of this norm conserving PPS in describing the various atomic systems, they must be highly transferable.

2. The PPS V_{pseudo} and pseudo wavefunction must be the same as the ionic potential and AE wavefunction respectively, and continuous even outside of r_c .
3. Pseudo electron and AE eigenvalues obtained from the atomic wavefunctions must be identical.
4. Pseudo wavefunction and its derivatives must always be continuous at the core radius and must be non-oscillatory.

The PAW method [81] has recently become the most widely used technique in first principles electronic structure calculations, and is basically the generalization of the ideas arising from the construction of the Vanderbilt ultrasoft PPS [79] and the linear-augmented-plane-wave (LAPW) [80] methods. Since the computational results of this thesis were obtained using the pseudopotentials generated by the PAW method, we give a brief overview of this method in the next section.

3.6.2 The projector augmented wave (PAW) PPS method

The concept of the PAW PPS method was first introduced by Blöchl in 1994 [81]. In 1999 Kresse and Joubert published the formulation that performed the transition from ultrasoft to PAW pseudopotentials [82]. Just like in the traditional PPS methods, the PAW method reduces the complexity of electron-ion interaction by smoothly varying the valence wavefunction inside the core region, but in a computationally efficient manner, during the solution of KS equations.

The main idea behind the PAW method is to map the AE valence wavefunction Ψ onto a fictitious pseudo nodeless wavefunction $\tilde{\Psi}$ using a linear transformation τ in this manner:

$$|\Psi\rangle = \tau|\tilde{\Psi}\rangle. \quad (3.99)$$

If the transformation τ from the pseudo wavefunction to the AE wavefunctions can be determined, the physical quantities expressed as the expectation value $\langle A \rangle$ of operator A can be calculated. The quantity which is of interest can be obtained from pseudo wavefunction $|\tilde{\Psi}\rangle$ in the form $\langle \Psi|A|\Psi\rangle$, after transformation to the true AE wavefunctions $|\Psi\rangle = \tau|\tilde{\Psi}\rangle$. The linear transformation τ acting between the AE valence wavefunctions and fictitious pseudo wavefunctions can be expanded in terms of a sum of local atom-centred contributions τ_R as

$$\tau = 1 + \sum_R \tau_R = 1 + \sum_i \left(|\phi_i\rangle - |\tilde{\phi}_i\rangle \right) \langle \tilde{P}_i|, \quad (3.100)$$

where ϕ_i and $\tilde{\phi}_i$ are the AE and pseudo partial wavefunctions respectively. The index i signifies that all the partial wavefunctions are from within the augmentation region Ω_R enclosing the atom (within a cut-off radius r_c region), and that is where each contributions τ_R acts. \tilde{P}_i is the projector function for pseudo partial wavefunctions. The set of projector functions \tilde{P}_i with the pseudo wavefunctions must certify the orthonormal condition $\langle \tilde{P}_i|\tilde{\phi}_j\rangle = \delta_{ij}$.

After transformation, the complete form of Eqn. (3.99) can be written as

$$|\Psi\rangle = |\tilde{\Psi}\rangle + \sum_i (|\phi_i\rangle - |\tilde{\phi}_i\rangle) \langle \tilde{P}_i | \tilde{\Psi} \rangle. \quad (3.101)$$

Eqn. (3.101) is determined in the following manner:

1. the all electron partial wavefunctions ϕ_i are obtained by radially integrating the Schrödinger equation of the atomic energies,
2. the pseudo partial wavefunctions $\tilde{\phi}_i$ are obtained as the mere solution of the Schrödinger equation for the energy of all electron partial wavefunctions and partial pseudopotential, due to the fact that the pseudo partial wavefunctions are equivalent to the all electron partial wavefunctions outside a core radius r_c [10].

The Ψ in Eqn. (3.101) is the Kohn-Sham wavefunction for one electron, and can be obtained by rapidly varying the pseudo wavefunction $\tilde{\Psi}$.

Considering the information given by Eqn. (3.101), the AE charge density $n(\mathbf{r})$ and the total energy E_{tot} , expressed as the expectation values of the pseudo wavefunctions, can be evaluated. The charge density $n(\mathbf{r})$ can be divided into three partial densities as follows:

$$n(\mathbf{r}) = \tilde{n}(\mathbf{r}) + n^1(\mathbf{r}) - \tilde{n}^1(\mathbf{r}), \quad (3.102)$$

where $\tilde{n}(\mathbf{r})$ is the smooth charge density obtained directly from $\tilde{\Psi}$ as

$$\tilde{n}(\mathbf{r}) = \sum_n f_n \langle \tilde{\Psi}_n | r | \tilde{\Psi}_n \rangle, \quad (3.103)$$

evaluated on a plane waves grid. f_n is the occupation of the n^{th} state. The other two partial charge densities

$$n^1(\mathbf{r}) = \sum_{n,(i,j)} f_n \langle \tilde{\Psi}_n | \tilde{p}_i \rangle \langle \phi_i | \mathbf{r} \rangle \langle \mathbf{r} | \phi_j \rangle \langle \tilde{p}_j | \tilde{\Psi}_n \rangle \quad (3.104)$$

and

$$\tilde{n}^1(\mathbf{r}) = \sum_{n,(i,j)} f_n \langle \tilde{\Psi}_n | \tilde{p}_i \rangle \langle \tilde{\phi}_i | \mathbf{r} \rangle \langle \mathbf{r} | \tilde{\phi}_j \rangle \langle \tilde{p}_j | \tilde{\Psi}_n \rangle \quad (3.105)$$

are treated on a radial support grid applying the projector wavefunctions \tilde{P}_i .

Following Eqn. (3.101), the total energy functional E_{tot} can also be divided into three sub energy contributions:

$$E_{tot} = \tilde{E} + E^1 - \tilde{E}^1, \quad (3.106)$$

where \tilde{E} is the smooth (pseudo) energy defined as

$$\begin{aligned} \tilde{E} = & \sum_n f_n \langle \tilde{\Psi}_n | -\frac{1}{2} \Delta | \tilde{\Psi}_n \rangle + E_{xc}[\tilde{n} + \hat{n} + \tilde{n}_c] + E_H[\tilde{n} + \hat{n}] \\ & + \int v_H[\tilde{n}_{Zc}][\tilde{n}(\mathbf{r}) + \hat{n}(\mathbf{r})] d\mathbf{r} + U(\mathbf{R}, Z_{ion}). \end{aligned} \quad (3.107)$$

This equation is evaluated on regular grids in Fourier or real space. V_H and E_H are the Hartree potential and energy, respectively, for electronic charge density $n(\mathbf{r})$. $U(\mathbf{R}, Z_{ion})$ is the electrostatic potential energy arising from point charges Z_{ion} [83] and E_{xc} is the exchange-correlation energy functional. The charge density \hat{n} is called the compensation charge. The energy contributions \tilde{E}^1 and E^1 can be expanded as

$$\begin{aligned} \tilde{E}^1 = & \sum_{ij} \rho_{ij} \langle \tilde{\phi}_i | -\frac{1}{2} \Delta | \tilde{\phi}_j \rangle + E_{xc}[\tilde{n}^1 + \hat{n} + \tilde{n}_c] + E_H[\tilde{n}^1 + \hat{n}] \\ & + \int_{\Omega_r} v_H[\tilde{n}_{Zc}][\tilde{n}^1(\mathbf{r}) + \hat{n}(\mathbf{r})] d\mathbf{r} \end{aligned} \quad (3.108)$$

and

$$\begin{aligned}
 E^1 = & \sum_{ij} \rho_{ij} \langle \tilde{\phi}_i | -\frac{1}{2} \Delta | \tilde{\phi}_j \rangle + E_{xc}[n^1 + n_c] + E_H[n^1] \\
 & + \int_{\Omega_r} v_H[n_{Zc}] n^1(\mathbf{r}) d\mathbf{r}.
 \end{aligned}
 \tag{3.109}$$

The contributions $n^1(\mathbf{r})$, $\tilde{n}^1(\mathbf{r})$, \tilde{E}^1 and E^1 are evaluated for each sphere on a radial support grid with no problems arising from the string variations near the nucleus. All the energy contributions mentioned in this thesis are from Ref. [82] which represents the improvements of those in Ref. [81]. In these two references, the kinetic and Hartree energies are treated in the same manner, but the core-core charges overlaps are ignored in Ref. [82], in some of the above mentioned contributions. In Ref. [81], the core-core electrostatic interactions are automatically included in the Hartree energy for all terms; however in this thesis, those interactions are only evaluated in the $U(\mathbf{R}, Z_{ion})$ of contribution \tilde{E} .

In summary, an overview of the PAW method shows that it is more advantageous than other traditional approaches due to the fact that it has an all-electron nature. In the PAW method, the formulation of charge density and the total energy functional are easy to follow. Lastly, the PAW method uses the full density and potential of the entire system, and therefore the converged results do not depend on an isolated atom, unlike in the other traditional approaches where PPS are constructed from an isolated atom, which this does not guarantee the accuracy of the PPS for the description of the entire system. In Ref. [82] it was concluded that the PAW method is able to handle most of the structures, including those having strong magnetic moments and large electro-negativity differences, with exceptional precision.

3.7 Tests of convergence

The plane wave self-consistent field (PWSCF) code included in the quantum espresso package [73] has been employed in this study of bilayer graphene systems. The projector augmented wave (PAW) method has been employed to mimic the electron-ion interaction. In order to accurately compute the properties for real materials, we need to test convergence for plane waves kinetic energy cut-off and the number of \mathbf{k} -points. For the convergence of energy in terms of plane waves kinetic energy cut-off, Fig. 3.2 depicts the variation of total energy with respect to energy cut-off for bilayer graphene. For the description of the exchange-correlation interaction, these tests were done using vdW-DF2-C09_x. Fig. 3.2 clearly displays smooth variation in the total energies as the

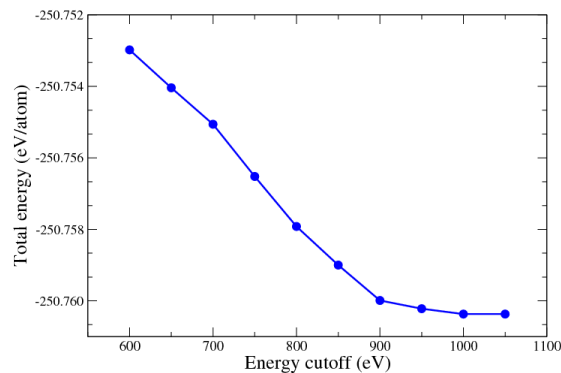


Figure 3.2: Total energy versus energy cutoff for bilayer graphene structure.

energy cutoff passes 900 eV. It is noted that the total energy adequately converges to within a meV at this energy cutoff. Further increase of the energy cutoff would have no significant effect on the accuracy of the results. Therefore, for all calculations presented in this thesis, the basis set contains the plane waves energy cutoff of 900 eV unless otherwise stated.

For the most suitable number of \mathbf{k} -points to sample the Brillouin zone, Fig. 3.3 illustrates the variation of total energies with respect to Monkhorst pack grid sizes calculated at a suitable energy cut-off of 900 eV. It is noted that the total energy

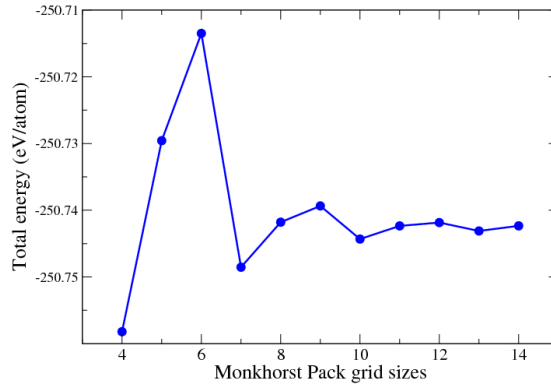


Figure 3.3: Plot of total energies variations with respect to Monkhorst Pack grid sizes ($k_x \times k_y \times k_z$) for bilayer graphene structure. Note that for two dimensional systems, grid sizes are defined as $k_x=k_y$ and $k_z=1$.

converges adequately, to within a 1 meV, at the $8 \times 8 \times 1$ Monkhorst pack \mathbf{k} -points. For the results computed in this thesis, the Brillouin zone integration was performed using the set of $10 \times 10 \times 1$. These tests were also carried out using the LDA and GGA PBE for comparison of the functionals, but no significant differences were observed on the plots.

Bibliography

- [1] D. Joubert, African School on Electronic Structure Methods: Density Functional Theory Basics, lecture notes, 3-45 (2008). [30, 31, 37]
- [2] D. Joubert (Ed.), Density Functionals: Theory and Applications, Springer Lecture notes in Physics **500**, (1998). [30]
- [3] R. M. Martin, Electronic Structure: Basic Theory and Practical Methods, Cambridge University Press, (2004). [31, 32, 34, 37, 41, 43, 44]
- [4] M. Born and J. R. Oppenheimer. Zur quantentheorie der molekeln, Ann. Physik, **84**, (1927). [31]
- [5] D. R. Hartree, Proc. Cambridge Phil. Soc., **24**, 89, 111, 426 (1928). [32]
- [6] J. Kohanoff and N.I. Gidopoulos, Molecular Physics and Quantum Chemistry **2**, Ch. 26, 532-568 (2003). [32, 33, 34, 35, 41, 43, 44, 45, 47]
- [7] V. Fock. Z. Phys., **65**, 209, (1930). [33, 34]
- [8] J. C. Slater, Phys. Rev., **35**, 210 (1930). [33]
- [9] C. Moller and M. S. Plesset, Phys. Rev., **46**, 618, (1934). [34]
- [10] M. C. Payne, M. P. Teter, D. C. Allan, T. A. Arias and J. D. Joannopoulos, Rev. Mod. Phys. **64**, 1045 (1992). [iv, 35, 39, 42, 44, 65, 69, 72]
- [11] C. J. Cramer, Essentials of Computational Chemistry, John Wiley & Sons. ISBN 0-470-09182-7 (2002). [35]

- [12] F. Jensen, Introduction to Computational Chemistry 2nd edition. John Wiley & Sons (1999). [35]
- [13] P. Hohenberg and W. Kohn, Phys. Rev. B **136**, 864 (1964). [35, 36, 37, 38]
- [14] W. Kohn and L. J. Sham, Phys. Rev. A **140**, 1133 (1965). [35, 39, 40, 43]
- [15] M. Levy, Phys. Rev. A **26**, 1200 (1982). [38]
- [16] E. H. Lieb, Physics as Natural Philosophy: Essays in Honour of Laszlo Tisza on his 75th Birthday, 111 (1982). [38]
- [17] R. O. Jones and O. Gunnarson, Rev. Mod. Phys **61**, 689 (1989). [38, 42, 45]
- [18] J. P. Perdew and Y. Wang, Phys. Rev. B **45**, 13244 (1992). [43, 45]
- [19] P. A. M. Dirac, Proc. Cambridge Phil. Roy. Soc. **26**, 376 (1930). [44]
- [20] D. M. Ceperley and B. J. Alder, Phys. Rev. Lett. **45**, 566 (1980). [44]
- [21] L. Hedin and B. Lundqvist, J. Phys. C **4**, 2064 (1971). [44]
- [22] S. H. Vosko, L. Wilk and M. Nusair, Can. J. Phys. **58** 1200 (1980). [44]
- [23] J. P. Perdew and A. Zunger, Phys. Rev. B **23**, 5048 (1981). [44, 47]
- [24] J. Harris and R. O. Jones, J. Phys. **4**, 177 (1974). [44]
- [25] O. Gunnarsson and B. I. Lundqvist, Phys. Rev. B **13**, 4174 (1976). [44]
- [26] D. C. Langreth and J. P. Perdew, Phys. Rev. B **15**, 2884 (1977). [44]
- [27] R. Q. Hood, M. Y. Chou, A. J. Williamson, G. Rajagopal, R. J. Needs and W. M. C. Foulkes, Phys. Rev. Lett. **78**, 3350 (1997). [45]
- [28] W. Koch and M. C. Holthausen, A Chemist Guide to Density Functional Theory: Wiley-VCH New York, 2nd. edn. (2001). [45]
- [29] J. P. Perdew, Phys. Rev. B **33**, 8822 (1986). [45]
- [30] J. P. Perdew and Y. Wang, Phys. Rev. B **33**, 8800 (1986). [45, 61]

- [31] S. Kurth, J. P. Perdew and P. Blaha, *Int. J. Quantum Chem.* **75**, 889 (1999). [45]
- [32] J. P. Perdew, K. Burke and M. Ernzerhof, *Phys. Rev. Lett.* **77**, 3865 (1996). [45, 46, 47, 54]
- [33] J.P. Perdew and Y. Wang, *Phys. Rev. B*, **45**, 13244 (1991). [46]
- [34] E. H. Lieb, S. Oxford, *International Journal of Quantum Chemistry*, **19**, 427 (1981). [46]
- [35] J. Hubbard, *Proceedings of the Royal Society A*, **296**, 100-112, (1967). [47]
- [36] J. Hubbard, *Proceedings of the Royal Society A*, **277**, 237-259, (1964). [47]
- [37] J. D. Van der Waals, *The Equation of State for Gases and Liquids*, in *Nobel Lectures in Physics 1901-1921* (Amsterdam, 1967) pp. 254-265. [47]
- [38] M. J. Klein, *Physica* **73**, 20-47 (1974). [47]
- [39] H. C. Hamaker, *Physica* **4**, 1058-1072 (1937). [47, 48]
- [40] R. Eisenschitz and F. London, *Z. Physik* **60**, 491-527, (1930). [48, 49]
- [41] F. London, *Z. Physik* **63**, 245, (1930). [49]
- [42] F. London, *Z. Physik. Chemie* **33**, 8-26 (1937). [49]
- [43] F. London, *Transactions of the Faraday Society*, **33**, 8-26 (1937). [49]
- [44] N. Zettili, *Quant. Mech. Concepts and Applications: John Wiley and Sons, LTD* (2001). [49, 50, 51, 52]
- [45] J. J. Breim, and W. J. Mullin, *A Course in Modern Physics: Introduction to the structure of matter*, John Wiley and Sons, LTD (1989). [53]
- [46] X. Wu, M. C. Vargas, S. Nayak, V. Lotrich and G. Scoles, *J. Chem. Phys.* **115**, 8748 (2001). [53]
- [47] S. Grimme, *J. Comput. Chem.* **25**, 1463-73 (2004). [53]
- [48] S. Grimme, *J. Comp. Chem.* **27**, 1787 (2006). [53]

- [49] L. A. Girifalco, M. Hodak and R. S. Lee, Phys. Rev. B **62**, 104 (2000). [53]
- [50] M. Hasegawa, K. Nishidate and H. Iyetomi, Phys. Rev. B **76**, 115424 (2007). [53]
- [51] H. Rydberg, B. Lundqvist, D. Langreth and M. Dion. Phys. Rev. B, **62**, 11 (2000). [53, 54, 56]
- [52] H. Rydberg, M. Dion, N. Jacobson, E. Schroder, P. Hyldgaard, S. Simak, D. Langreth and B. Lundqvist, Phys. Rev. Lett, **91**, 12 (2003). [53, 54, 55, 56]
- [53] D. C. Langreth, M. Dion, H. Rydberg, E. Schroder, P. Hyldgaard and B. I. Lundqvist. Int. J. Quant. Chem., **101**, 5 (2004). [53, 54, 56, 57]
- [54] M. Dion, H. Rydberg, E. Schroder, D. C. Langreth and B. I. Lundqvist, Phys. Rev. Lett., **92**, 246401 (2004). [53, 54, 56, 57, 58, 59, 60, 61]
- [55] M. Dion, PhD thesis, Rutgers University, (2004). [53, 54, 56, 57, 58, 59, 60]
- [56] D. C. Langreth and J. P. Perdew, Phys. Rev. B **15**, 2884 (1977). [57]
- [57] D. C. Langreth and J. P. Perdew, Sol. Sta. Commun, **17**, 1425 (1975). [57]
- [58] F. BU, PhD J. Math. Phys, **11**, 5 (1978). [57]
- [59] Y. Zhang and W. Yang, Phys. Rev. Lett. **80**, 890 (1998). [54, 61, 62]
- [60] E. M. Lifshitz, Sov. Phys. JETP **2**, 73, (1956). [55]
- [61] Y. Anderson, E. Hult, P. Apell, D.C. Langreth, and B.I. Lundqvist, Sol. Sta. Commun. **106**, 235 (1996). [55]
- [62] DACAPO materials simulation code can be found at, <http://www.fysic.dtu.dk/CAMPOS/>. [56, 61]
- [63] K. Lee, E. D. Murray, L. Kong, B. I. Lundqvist and D. C. Langreth, Phys. Rev. B **82**, 081101 (2010). [61, 62]
- [64] E. D. Murray, K. Lee and D. C. Langreth, J. Chem. Theory Comput. **5**, 2754 (2009). [61]
- [65] V. R. Cooper, Phys. Rev. B **81**, 161104 (2010). [62, 63]

- [66] L. J. Sham, Computational Methods in Band Theory (Plenum, New York), (1971). [62]
- [67] X. Gonze, J.-M. Beuken, R. Caracas, F. Detraux, M. Fuchs, G.-M. Rignanese, L. Sindic, M. Verstraete, G. Zerah, F. Jollet, *et al.*, Comp. Mat. Scie. **25**, 478 (2002). [63]
- [68] P. Jurecka, J. Sponer, J. Cerny and P. Hobza, Phys.C. Chem. Phys. **8**, 1985 (2006). [63]
- [69] R. Podeszwa and K. Szalewicz, Chem. Phys. Lett. **412**, 488 (2005). [63]
- [70] R. Zacharia, H. Ulbricht, and T. Hertel, Phys. Rev. B **69**, 155406 (2004). [63]
- [71] I. Hamada and M. Otani, Phys. Rev. B **82**, 153412 (2010). [63]
- [72] See Table SIV in the supplementary material of Ref. 54. Available online at: <http://link.aps.org/supplemental/10.1103/PhysRevB.82.153412>. [63]
- [73] P. Giannozzi, S. Baroni, N. Bonini, M. Calandra, R. Car, C. Cavazzoni, D. Ceresoli, G. L. Chiarotti, M. Cococcioni, I. Dabo, A. Dal Corso, S. Fabris, G. Gougoussis, A. Kokalj, M. Lazzeri, L. Martin-Samos, N. Marzari, F. Mauri, R. Mazzarello, S. Paolini, A. Pasquarello, L. Paulatto, C. Sbraccia, S. Scandolo, G. Sclauzero, A. P. Seitsonen, A. Smogunov, P. Umari, and R. M. Wentzcovitch, J. Phys. Condens. Matter **21**, 395502 (2009). [63, 75]
- [74] N. W. Ashcroft and N. D. Mermin. Sol. Sta. Phys., 762-763 (1976). [64]
- [75] H. J. Monkhorst and J. D. Pack, Phys. Rev. B **13**, 5188, (1976). [67]
- [76] M. Methfessel and A. T. Paxton. Phys. Rev. B **40**, 3616,(1989). [68]
- [77] D. R. Hamann, M. Schluter, and C. Chiang, Phys. Rev. Lett. **43**, 1494, (1979). [69, 70]
- [78] G. B. Bachelet, M. Schluter, and C. Chiang, Phys. Rev. B **26**, 4199 (1982). [69, 70]
- [79] D. Vanderbilt, Phys. Rev. B **41**, 7892 (1990). [69, 70]
- [80] D. J. Singh, Planewaves, Pseudopotentials and the LAPW Method: Kluwer Academic, Norwell, MA, (1994). [70]
- [81] P. E. Blochl, Phys. Rev. B **50**, 17 953 (1994). [69, 70, 71, 74]
- [82] G. Kresse and D. Joubert, Phys. Rev. B **59**, 1758 (1999). [71, 74]

- [83] N. A. W. Holzwarth, G. E. Matthews, R. B. Dunning, A. R. Tackett, and Y. Zeng, Phys. Rev. B **55**, 2005 (1997). [73]
- [84] M.L. Cohen and V. Heine, Sol. Sta. Phys., **24**, 37 (1970). [69]

Chapter 4

Ab initio studies of hydrogen adatoms on bilayer graphene

The work presented in this chapter has been published: R. E. Mapasha, A. M. Ukpong and N. Chetty, *PHYSICAL REVIEW B* **85**, 205402 (2012). In this chapter, we use the newly developed exchange-correlation functionals to study various hydrogen configurations on bilayer graphene at 50% coverage. As mentioned earlier, previous studies only focused on hydrogenating the top and bottom external faces of the bilayer graphene, in this study, we consider also the hydrogenation of the interlayer faces. Detailed information for this study is given in the attached publication. This publication outlines the computational details used and the results that were obtained together with the conclusions that were drawn from the study.

Ab initio studies of hydrogen adatoms on bilayer graphene

R. E. Mapasha,¹ A. M. Ukpong,^{1,*} and N. Chetty^{1,2}

¹*Department of Physics, University of Pretoria, Pretoria 0002, South Africa*

²*National Institute for Theoretical Physics, Johannesburg, 2000, South Africa*

(Dated: August 28, 2013)

We present a comparative density functional study of the adsorption of hydrogen on bilayer graphene. Six different exchange-correlation functionals are employed to explore the possible configurations of hydrogen adsorption at 50% coverage. Using the four variants of the non-local van der Waals density functional, we identify three distinct competing configurations that retain the coupled bilayer structure at 0 K. One of the configurations undergoes a spontaneous transformation from hexagonal to tetrahedral structure, under hydrogenation, with heat of formation ranging between -0.03 eV (vdW-DF) and -0.37 eV (vdW-DFC09_x). This configuration has a finite band gap of around 3 eV, whereas all other competing configurations are either semi-metallic or metallic. We also find two unique low-energy competing configurations of decoupled bilayer graphene, and therefore suggest the possibility of graphene exfoliation by hydrogen intercalation.

PACS numbers: 71.15.Nc, 71.20.-b, 73.20.Hb, 73.22.Pr

I. INTRODUCTION

Graphene, a free-standing single-atom thick layer of graphite, was first isolated in 2004.¹ The first production of graphene involved the ex-foliation and cleavage methods. These involve the peeling of single-atom thick layers from bulk highly-oriented pyrolytic graphite (HOPG).¹ Graphene has remarkable properties, such as the anomalous quantum Hall effect, high carrier mobility and ballistic transport up to room temperatures.²⁻⁶ These properties suggest that graphene can be a reliable candidate for applications in nanotechnology and microelectronic devices.⁷ The local network structure of graphene, just as in graphite, consists of sp²-hybridized carbon bonds. In the plane of the hexagonal lattice, each carbon atom is bonded to three nearest neighbors by strong σ -bonds.⁸ In addition, there is a weak π -bond localized on each carbon atom. The resulting band structure shows the π -bands near the Fermi level.^{3,8} These arise from orbitals located near the K and K' points on opposite corners of the Brillouin zone. The electronic signatures of the π -bands are uniquely characterized by a Dirac-like dispersion at the Γ -point. These form linear dispersions, at the K -point. Since the valence and conduction bands meet at the K -point, graphene exhibits a zero band gap.^{3,8} The resulting semi-metallic behavior therefore limits the range of applicability of graphene monolayers in nanotechnological and microelectronic applications.

As a result, concerted efforts have been directed towards tuning the band gap in graphene monolayers both experimentally⁹⁻¹⁵ and theoretically.¹⁶⁻²⁴ There are various ways in which the graphene structure has been explored. These include producing nanoribbons,²⁵⁻²⁷ rotating the carbon atoms at specific angles to form Stone-Wales-type defects,^{18,21,28-32} and adsorbing different impurities on the monolayer.⁹⁻²⁴ The latter has been regarded as the most promising method because the adsorption of hydrogen modifies the local structure significantly. At 100 % hydrogen-coverage, the local structure

is completely transformed from sp² to sp³ hybridized carbon bonds.^{14,15,24} Adsorption of hydrogen atoms on graphene was first studied experimentally by Elias *et al.*¹⁵ and theoretically by Sofo *et al.*²⁴ The band gap was found to be 3.5 eV in both cases. However, more recent studies¹⁶⁻²³ have focused on the energetics, and structural stability of the graphene monolayer using density functional theory (DFT).

Bilayer graphene is a stacked double layer of graphene, which is weakly bound by van der Waals forces. It possesses interesting electronic properties, which are slightly different from those of single layer graphene. In bilayer graphene, electrons behave as massive chiral fermions,^{33,34} whereas they behave as massless Dirac fermions in single layer graphene.⁶ This results in ballistic electron transport seen in the graphene monolayer. The linear dispersion around the K -point in a graphene monolayer becomes parabolic in bilayer graphene.³³ However, the valence and conduction bands also meet at the K -point of the Brillouin zone. This arrangement of bands indicate that bilayer graphene is also semi-metallic.^{33,34} Experimentally, the first attempt to open the band gap in bilayer graphene was successfully achieved by the application of a strong electric field perpendicular to the graphene planes.³⁵ In addition, this has been achieved by chemical modification of the local structure,^{15,19,22,34,36-39} and by the application of uniaxial strain on the structure.^{40,41} Just as in single layer graphene, the hydrogen adatoms were considered to be the preferred candidates to facilitate the transformation of the structure from a semimetal to an insulator.

Luo *et al.*³⁶ reported that the hydrogenation of a few single layers of graphene is less feasible than those of bilayer and trilayer graphene. They also showed experimentally that the hydrogenation and dehydrogenation of graphene depends on the number of monolayers. They found that, depending on the plasma power, the hydrogen coverage can be manipulated up to the saturation level of 100 % H-coverage. Furthermore, Subrah-

manyam *et al.*³⁷ demonstrated the possible use of few layer graphene in hydrogen storage. They showed that few layer graphene can contain up to 5 wt% of hydrogen, which is more than the 3 wt% stored in carbon nanotubes. Their spectroscopic measurements on hydrogenated bilayer graphene showed that the local structure contains some sp^3 -hybridized carbon bonds. They also observed that hydrogen decomposes when the structure is heated up to 500 °C. Jaiswal *et al.*³⁸ investigated the electronic properties of graphene sheets at different degrees of hydrogenation using Raman and charge transport spectroscopies. They showed that partially hydrogenated mono- and bi-layer graphene has weak insulating behavior, and that bilayer graphene is more readily affected by hydrogen compared to few single layers of graphene, in agreement with the measurements of Luo *et al.*³⁶

Few single layers of graphene (SLG) contain more than three bound graphene monolayers. The observation by Elias *et al.*,¹⁵ that the SLG is far more receptive to hydrogen than bilayer graphene is in direct contrast to the measurements of Luo *et al.*³⁶ Earlier, Boukhvalov *et al.*¹⁹ performed a comparative study of hydrogen adsorption on single and bilayer graphene using DFT. They considered the single hydrogen and pair of hydrogen adatoms and found that the lattice distortions were different in single and bilayer structures. They observed that the distance between any two bonded carbon atoms in the bilayer is less than the equivalent distance in the single layer. This is because the interlayer interaction makes the layers to remain flat. Based on the chemisorption energies, they concluded that in both structures, the pair of hydrogen adatoms stabilizes the structure better than the single hydrogen adatom.¹⁹ This conclusion was also validated using the activation energies, since the single and pair of hydrogen adatoms yielded positive and negative activation energies, respectively. They also found that the hydrogenated monolayer is far more stable than the hydrogenated bilayer graphene. Later on, Boukhvalov *et al.*²² argued that the maximum hydrogen coverage on bilayer graphene is 25 %, and that this configuration gives the most stable structure. At 25 % coverage, the interlayer distance reduces to 3.25 Å from the 3.35 Å obtained in pristine bilayer graphene. In this configuration, the band structure showed a wide gap between the conduction and valence bands.

Leenaerts *et al.*³⁹ investigated the possibility of 50 % hydrogen coverage on bilayer graphene. The interlayer distance was found to reduce significantly, resulting in the creation of strong covalent bonds that stabilize the structure. However this transformation only occurs when the hydrogen is adsorbed on top of an indirect carbon atom (*i.e.*, on top of the carbon atom that faces the center of the hexagon on the opposite layer). In this configuration, the unhydrogenated carbon atom faces another unhydrogenated carbon atom on the opposite layer. The resulting structure has a wide band gap. Nevertheless, the formation energy is still higher than that of the hydrogenated

single layer graphene. On this basis, they also concluded that the hydrogenated single layer is more stable than the hydrogenated bilayer graphene.

Previous DFT investigations of hydrogen adsorption on graphene mono-, bi-, and few single layers of graphene have so far, not included the effects of van der Waals interactions. Besides, Boukhvalov *et al.*¹⁹ investigated the chemisorption of a single H atom, and a pair of H atoms on a 32-atom supercell. These two configurations correspond to hydrogen coverage of 3.1% and 6.3%, respectively. In particular, these two levels of hydrogen coverage are low, and insufficient to capture the H-induced transformations of the bilayer graphene structure. Moreover, the more recent investigation of Leenaerts *et al.*³⁹ considered a single configuration for hydrogen adsorption at 50% coverage. Because previous studies only focused on hydrogenating the top and bottom external faces of the graphene bilayer,³⁹ we consider also the hydrogenation of the interlayer faces.

We present a comparative density functional study of the structural configurations of hydrogen adsorption on bilayer graphene. In our work, the number of hydrogen adatoms is always chosen to be 50 % coverage in each of the configurations. Leenaerts *et al.*³⁹ suggested this as the maximum possible H-coverage on bilayer graphene. This has motivated us to systematically investigate the stable competing low-energy configurations that may exist at this level of hydrogenation. The aim is to identify energetically favorable configurations and identify competing low energy structures at 0 K. We also investigate the influence of H-adatoms on the electronic properties of bilayer graphene within the framework of density functional theory, using different exchange-correlation (XC) potentials. We show that no single XC functional is able to reproduce all the known physical properties of all the configurations considered. The relative strengths and weaknesses of the functionals are discussed.

II. METHODOLOGY

The ground state electronic structure was calculated using the plane wave self-consistent field (PWSCF) code as implemented in the Quantum ESPRESSO package.⁴² The calculations were first performed using the local density and the generalized gradient approximations (LDA)⁴³ and (GGA)⁴⁴ for the exchange-correlation interaction. We used the GGA parameterization of Perdew, Burke and Ernzerhof (PBE).⁴⁴ Thereafter, the Roman-Perez and Soler implementation⁴⁵ of the non-local van der Waals density functional (vdW-DF) theory of Dion *et al.*⁴⁶ was used to study the ground state properties of graphite, pristine and hydrogenated bilayer graphene. The second version of the van der Waals density functional (vdW-DF2) theory proposed by Lee *et al.*⁴⁷ was also used to calculate the properties of these materials for comparison. In the vdW-DF2 calculations, an accurate refit⁴⁸ of the Perdew-Wang (PW86) semilocal exchange

functional⁴⁹ was used. Furthermore, the exchange functional (C09_x) of Cooper⁵⁰ was also used within the two vdW-DF schemes to perform a comparative study of these materials, and results from these two schemes are denoted as vdW-DFC09_x and vdW-DF2C09_x.

The core electron interactions were described using the projector augmented wave (PAW) methods.⁵¹ Energy cut-offs of 500 and 5170 eV were set for the wave function and charge density expansions, respectively, in the plane waves basis. The Monkhorst-Pack scheme⁵² was used for the integration of electronic states, using a grid of size $10 \times 10 \times 1$. The Methfessel-Paxton (MP) scheme⁵³ was used in the self-consistent field calculations, with a smearing width of 0.3 eV. The total energies were converged to within 10^{-7} eV. The supercells were optimized using the conjugate gradient algorithm with an atomic force convergence criterion of 0.01 eV/Å. In each case, the graphite and bilayer graphene structures were modeled using a 1×1 periodic unit cell. The vacuum height was set to 15 Å to avoid spurious interactions between periodically repeated images of the graphene bilayer system.

III. RESULTS AND DISCUSSION

A. Test of exchange-correlation functionals on bulk bilayer graphene and graphite

In this section, the different exchange-correlation functionals are tested on the properties of graphite and bilayer graphene. In bilayer graphene, the two monolayers are arranged in two distinct stacking sequences: the simple (AA) and Bernal (AB) conformations. Results show that the Bernal stacking gives a more stable bilayer graphene structure than the simple stacking sequence. The AB-stacked structure gives a total energy per atom, which is 0.02 eV (LDA), 0.01 eV (GGA) and 0.01 eV (vdW-DF) lower than the corresponding total energy in the simple stacking sequence. The LDA total energy difference is consistent with the results of De Andres *et al.*⁴¹ In addition, the AB-stacking sequence consistently yields stronger interlayer binding from all the XC functionals. For instance, the simple stacking sequence gives an interlayer separation that is 0.21 Å (LDA), 0.02 Å (GGA) and 0.22 Å (vdW-DF) larger than the corresponding distance in a Bernal stacked structure. As a result, we will not discuss the AA-stacked bilayer graphene any further and all subsequent adsorption studies are reported for the AB-stacked structures.

Table I shows the lattice constant (a_0), interlayer distance (d_0), and the interlayer binding energy (E_B) of graphite and pristine bilayer graphene from different form of exchange correlation functionals. The interlayer binding energy in this case, is the total energy difference between the two coupled and uncoupled graphene layers. The properties of the bilayer, *i. e.* lattice constant and interlayer distance, are generally similar to

those of graphite as expected. For instance, although slightly smaller than the experimental value (2.46 Å) in both structures,⁵⁸ the optimized LDA lattice constant (2.45 Å) is the same for bilayer graphene and graphite. The difference between their corresponding GGA values is less than 1%. This trend is also consistent with other LDA and GGA calculations.⁵⁴ The LDA interlayer distance is 3.25 Å for graphite and 3.33 Å for bilayer graphene. In both structures, the GGA predicts the same value (4.10 Å) for d_0 but overestimates the experimental value substantially (see Table I). More significant differences are observed between our GGA-PBE values, and the GGA-PBE(DCAP) data⁶² for d_0 and E_B respectively. Nevertheless, there is good agreement between our results and similar calculations. The calculated LDA interlayer binding energy of graphite is 27.70 meV/atom. Our calculated LDA bilayer binding energy decreases to 17.30 meV/atom. This value is nearly half the experimental value of the binding energy in graphite. As expected, results of our GGA calculations fail to accurately describe structures that are bounded together by van der Waals forces (see Table I). We also tested the structural properties of the bilayer and graphite using different variants of the van der Waals (vdW) corrections to DFT. Our calculated vdW-DF lattice constants for graphite and bilayer graphene are 2.48 Å and 2.47 Å respectively, in good agreement with results of other vdW-DF calculations.^{55,56}

TABLE I. Properties of graphite and pristine bilayer graphene calculated using different exchange-correlation functionals to show the equilibrium lattice constants a_0 , interlayer distances d_0 and the interlayer binding energies E_B . Results of our calculations are marked with an asterisk (*). The vdW-DF exfoliation energy of graphite is also shown (in parenthesis).

Functionals	Graphite			Bilayer		
	a_0 (Å)	d_0 (Å)	E_B (meV)	a_0 (Å)	d_0 (Å)	E_B (meV)
LDA*	2.45	3.25	27.70	2.45	3.33	17.30
LDA	2.44 ^a	3.32 ^a	(-26.00) ^a		3.30 ^h	13.98 ^h
GGA*	2.47	4.10	3.00	2.46	4.10	3.00
GGA	2.46 ^a	4.50 ^a	(-2.00) ^a		3.32 ⁱ	27.00 ⁱ
vdW-DF*	2.48	3.57	55.00	2.47	3.51	22.70
vdW-DF			(-52.00) ^a		3.58 ^h	25.43 ^h
vdW-DF	2.47 ^b	3.76 ^c	24.00 ^b			
vdW-DF		3.60 ^d	45.50 ^d			
vdW-DF2*	2.47	3.49	66.00	2.47	3.49	29.00
vdW-DF2			(-53.00) ^a		3.48 ^h	25.84 ^h
vdW-DF C09 _x *	2.48	3.25	91.00	2.48	3.27	38.90
vdW-DF C09 _x			(-73.00) ^a		3.23 ^h	35.63 ^h
vdW-DF2 C09 _x *	2.47	3.29	59.60	2.48	3.29	28.60
vdW-DF2 C09 _x			(-54.00) ^a		3.28 ^h	25.86 ^h
Experimental	2.46 ^e	3.35 ^e	52±5 ^f , 35±10 ^g	2.46 ^j	3.40 ^j	

^aReference⁵⁴

^bReference⁵⁵

^cReference⁵⁶

^dReference⁵⁷

^eReference⁵⁸

^fReference⁵⁹

^gReference⁶⁰

^hReference⁶¹

ⁱReference⁶²

^jReference³⁵

Our vdW-DF optimized interlayer distance of 3.50 Å is intermediate between the GGA and LDA values for both graphite and bilayer graphene. However, this is closer to the LDA value than to the GGA value. On the other hand, vdW-DF2 yields the same structural properties for

graphite and the bilayer. For graphite, we find that using the Cooper exchange functional (C09_x) within the vdW scheme results in the highest interlayer binding energy of 91.00 meV (vdW-DFC09_x). This value is 18.00 meV higher than the exfoliation energy predicted for graphite within the vdW-DFC09_x scheme.⁵⁴ However, within the vdW-DF2C09_x scheme, the interlayer binding energy reduces to 59.60 meV. Consider that the graphite interlayer binding energies of 55.00 meV (vdW-DF) and 66.00 meV (vdW-DF2) are significantly lower, prior to correction with C09_x functional. Because the structural properties of graphite predicted within the vdW-DFC09_x scheme, in Table I, agree with experimental values to within $\pm 3\%$, we attribute the large discrepancy in interlayer binding energy to the inability of the vdW-DFC09_x functional to simultaneously describe the energetics and the structural properties consistently. In Ref. 57, however, bilayer graphene is used as a model to estimate the binding energy of graphite as 45.50 meV/atom using the vdW-DF scheme. It is therefore expected *a posteriori* that bilayer graphene should have nearly the same binding energy. The calculated bilayer binding energy is 22.70 meV/atom (vdW-DF) and 29.00 meV/atom (vdW-DF2), which are 50% and 36% smaller than anticipated. Nevertheless, our vdW-DF and vdW-DF2 values are within the range of the results of other similar calculations (see Table I).

The use of the Cooper exchange functional (C09_x) shows a substantial increase to 38.90 eV/atom (vdW-DFC09_x), and a marginal increase to 28.60 meV/atom (vdW-DF2C09_x) in each case. Taken together, the vdW-interaction corrections give bilayer binding energy that agree with the experimental value of 35 ± 10 meV/atom for graphite, in agreement with previous vdW-DF calculations.⁵⁴ However, more recent experiments show a substantially higher interlayer binding energy of 52 ± 5.00 meV/atom in graphite.⁵⁹ This is significantly higher than the calculated bilayer binding energy, but consistent with our calculated values for graphite. We attribute this discrepancy to the inability of the functionals to simultaneously account for both the structural properties and the binding energies of weakly bound structures that are coupled together by vdW forces.

B. Hydrogen adatoms on bilayer graphene

1. Site geometries for hydrogen adsorption

The unrelaxed site geometries for hydrogen adsorption on the bilayer graphene unit cell are shown in Fig. 1. Because H prefers the on-top site,³⁹ each coupled bilayer graphene configuration has the H atoms occupying on top sites in the unrelaxed state. However, we do not consider the case of hydrogen adsorption at both the on top and bottom sites of the same carbon atom - even if such configurations can, in principle, give 50 % H coverage in the unrelaxed state. This is to preserve the hexagonal symmetry of the sp²-hybridized carbon bonding in bilayer

graphene prior to relaxation. In the following analysis, the carbon atoms that directly face another carbon atom (i.e., a and b' in Fig. 1) are labeled direct carbon atoms, whereas indirect carbon atoms face hollow sites in the adjacent layer (i.e., b and a' in Fig. 1). In all the unrelaxed configurations, the interlayer distance is the same, and the C-C distance is unique in both A- and B-planes, by symmetry.

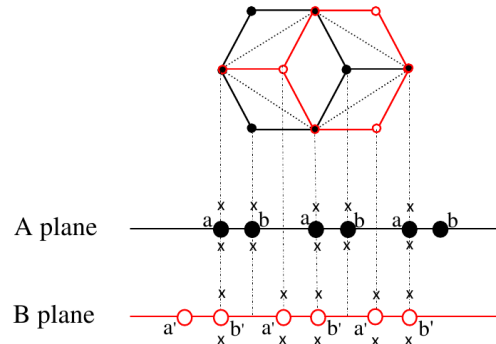


FIG. 1. Hydrogen adsorption sites (marked x) in the unrelaxed state of the bilayer graphene unit cell. The carbon atoms denoted by a and b' are the direct carbon atoms, while atoms b and a' are the indirect carbon atoms.

A total of 24 non-unique configurations are identified for cases where the two hydrogen atoms are adsorbed at on top sites on two different carbon atoms. From translational symmetry, this reduces to 18 configurations. In Fig. 1, planes A and B are invariant under 180° rotation. After correcting for double counting, only the 16 configurations listed in Table II are unique in the unrelaxed state. We find that some configurations are energetically equivalent after relaxation in spite of the uniqueness of their initial unrelaxed states.

For instance, three distinct cases are identified for formation of molecular hydrogen after relaxation. The dimer forms above the coupled bilayer structure in configuration c_1 as shown in Fig. 2(a), and within the interlayer region in configurations c_{12} , c_{14} and c_{15} . Because the dimer is oriented horizontally in both configurations c_{12} and c_{14} (see Fig. 2(b)), we conclude that both configurations are energetically equivalent. On the other hand, the dimer in configuration c_{15} is oriented vertically (Fig. 2(c)), and therefore represents a unique configuration, and distinct from configuration c_{12} or c_{14} . The three cases of dimer formation are energetically non-equivalent and unique, suggesting that their unrelaxed states are not stable. As a result, we investigate the physisorption of the H₂ dimer above bilayer graphene, and within the interlayer region as special cases of the hydrogen adsorption.

Each of the four schemes for correcting for vdW-

TABLE II. Configurations of hydrogenated bilayer at 50 % coverage and the corresponding hydrogen adsorption site geometries in the unrelaxed and relaxed states showing the changes in the local structure after structure optimization.

Configurations	Geometry of the H adatom site		Structural transformations
	Unrelaxed state	Relaxed state	
c_1	$a_{above}b_{above}$	$a_{above}a_{above}$	Formation of horizontal H ₂ dimer None (c_2 is symmetrical to c_{10} by translation) None None None None None None Formation of diamond-like structure None One hydrogen site is swapped (c_{10} relaxes to c_2) None Formation of horizontal H ₂ dimer (c_{12} relaxes to c_{14}) None Formation of horizontal H ₂ dimer (c_{14} relaxes to c_{12}) Formation of vertical H ₂ dimer None
c_2	$a_{above}b_{below}$	$a_{above}b_{below}$	
c_3	$a_{above}a_{above}$	$a_{above}a_{above}$	
c_4	$a_{above}b_{above}$	$a_{above}b_{above}$	
c_5	$a_{above}b_{below}$	$a_{above}b_{below}$	
c_6	$a_{above}a_{below}$	$a_{above}a_{below}$	
c_7	$b_{above}a_{below}$	$b_{above}a_{below}$	
c_8	$b_{above}a_{above}$	$b_{above}a_{above}$	
c_9	$b_{above}b_{above}$	$b_{above}b_{above}$	
c_{10}	$b_{above}b_{below}$	$b_{above}b_{below}$	
c_{11}	$a'_{above}b_{below}$	$a'_{above}b_{below}$	
c_{12}	$a'_{above}a_{below}$	$a'_{above}a_{below}$	
c_{13}	$a_{above}b'_{above}$	$a_{above}b'_{above}$	
c_{14}	$b'_{above}a_{below}$	$b'_{above}a_{below}$	
c_{15}	$b'_{above}b_{below}$	$b'_{above}b_{below}$	
c_{16}			

interaction predict the same interlayer distances for the two configurations of the horizontally-oriented dimer as: 6.67 Å (vdW-DF), 6.29 Å (vdW-DF2), 6.19 Å (vdW-DFC09_x) and 6.14 Å (vdW-DF2C09_x) respectively. In configuration c_{15} the dimer is vertically oriented, and the interlayer distance changes slightly to 6.93 Å (vdW-DF), 6.53 Å (vdW-DF2), 6.26 Å (vdW-DFC09_x) and 6.22 Å (vdW-DF2C09_x) respectively. When the Cooper (C09_x) functional is used within the two vdW-DF schemes, the interlayer distances only reduce slightly. Because of this marginal reduction in interlayer distance, we conclude that vdW-DFC09_x and vdW-DF2C09_x schemes both predict slightly stronger binding in the two cases of interlayer dimer formation. Nevertheless, the trend for variation in interlayer distances with exchange-correlation functional in configuration c_{12} , c_{14} and c_{15} is not uniform. For instance, although all the functionals consistently yield large values of d_0 , the variations in d_0 with vdW-DF correction scheme are non-uniform. Particularly, the vdW-DF2, vdW-DFC09_x and vdW-DF2C09_x schemes predict smaller interlayer distances in configurations c_{12} and c_{15} respectively. Similarly, LDA gives a slight decrease from 5.90 Å (c_{12}) to 5.84 Å (c_{14}) although both configurations are equivalent, whereas GGA-PBE shows a slight increase from 8.42 Å (c_{12}) to 8.51 Å (c_{14}), respectively. More importantly, apart from the vdW-DFC09_x functional, all other schemes show that d_0 is consistently larger when the dimer forms vertically in configuration c_{15} compared to when it forms horizontally in configuration c_{12} .

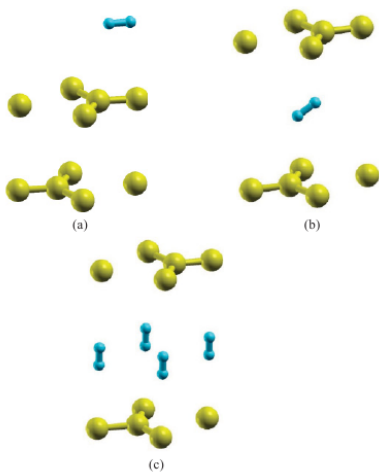


FIG. 2. Relaxed configurations showing the formation of the H₂ dimer: (a) above bilayer graphene in configuration c_1 , and within the interlayer region of the decoupled bilayer graphene showing (b) horizontal intercalation in configurations c_{12} and c_{14} , and vertical intercalation in configuration c_{15} .

Taken together, these interlayer distances are large relative to the equilibrium interlayer distances in pristine

graphene bilayer (see Table I). We ascribe the large interlayer distances to the decoupling of the bound bilayer graphene because of formation of the molecular hydrogen. The dimer formation breaks the symmetry of bilayer graphene structure. In the relaxed state, the large interlayer distances in configurations c_{12} , c_{14} , and c_{15} imply that the two bound monolayers of graphene are no longer coupled, and are therefore structurally not equivalent to the coupled bilayer system in configuration c_1 . This is due to weakened van der Waals interactions between layer A and B. The formation of the dimer in the interlayer region is analogous to hydrogen intercalation of bilayer graphene. By extension, we suggest the mechanism of hydrogen intercalation of graphite as a promising method of exfoliating graphene monolayers.

2. Formation energy of hydrogenated bilayer graphene

Competing low energy configurations of hydrogenated bilayer graphene are identified by investigating the formation energy per carbon atom. The formation energy was obtained using the expression²⁴

$$E_f = [E_{H-b} - N_C \times E_G - N_H \times \frac{1}{2}E_{H_2}]/N_C, \quad (1)$$

where E_{H-b} is the energy of relaxed hydrogenated bilayer graphene, E_G and E_{H_2} are the total energy per atom of the graphite and hydrogen molecule (H₂). N_C and N_H denote the total number of carbon and hydrogen atoms in the 1×1 unit cell. Formation energies are presented for LDA, GGA and the four implementations of the non-local vdW corrections to compare their relative stabilities and to predict the competing low energy structures at 0 K.

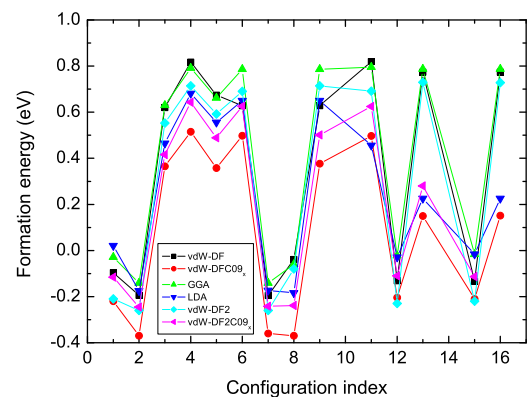


FIG. 3. Formation energies of unique configurations of hydrogenated bilayer graphene obtained using the LDA, GGA and the four different applications of the non-local van der Waals correlation functional.

Fig. 3 shows the formation energy per carbon atom

in structurally unique configurations of hydrogenated bilayer graphene from six XC functionals. In the cases where more than one configuration presents the same formation energy, only one formation energy is presented. The LDA gives the lowest formation energies E_f compared to GGA and vdW-DF. The high formation energies indicate that it is energetically more expensive to create these configurations. In the relaxed state of configuration c_{10} , the local structure shows that the H-adatom on the direct carbon of the interlayer region (i.e. hydrogen atom adsorbed on site b'_{above}) undergoes interlayer diffusion, and migrates to occupy another on top site. This further confirms the affinity of hydrogen to the on top site in graphene monolayers. However, the local structure in configuration c_{10} is equivalent to that in configuration c_2 because the difference between their heats of formation is 0.002 eV (LDA), 0.0 eV (GGA) and 0.001 eV (vdW-DF). Hence the two configurations are energetically equivalent in their relaxed states.

The vdW-DF schemes yield the same formation energies in energetically equivalent structures. For instance, we obtain -0.13 eV (vdW-DF) and -0.23 eV (vdW-DF2) in configurations c_{12} and c_{14} , and -0.13 eV (vdW-DF) and -0.22 eV (vdW-DF2) in configuration c_{15} . These energies change to -0.20 eV (vdW-DFC09 $_x$) and -0.11 eV (vdW-DF2C09 $_x$) in c_{12} and c_{14} respectively, and -0.21 eV (vdW-DFC09 $_x$) and -0.11 eV (vdW-DF2C09 $_x$) respectively in configuration c_{15} . Because the energy of formation of the vertical dimer in configuration c_{15} is different from the energy required to form horizontal dimers in both configurations c_{12} and c_{14} , we identify the formation of both dimer orientations as unique.

We identify six energetically favorable configurations at 0 K. These are configurations c_1 , c_2 , c_7 , c_8 , c_{12} and c_{15} . Only configurations c_1 , c_2 , c_7 and c_8 retain the coupled bilayer structure in the relaxed state. Because configuration c_8 is known³⁹ to undergo a hydrogen-induced phase transformation from hexagonal to tetrahedral geometry, we suggest that the four low energy configurations are competing structures at 0 K. Our calculated formation energies for configuration c_8 from both LDA, GGA and vdW-DF functionals agree with the GGA and LDA calculations of Leenaerts *et al.*³⁹ Apart from configurations c_1 and c_{12} , the LDA gives comparatively lower formation energies than GGA and the vdW-corrected functionals. We observe that GGA and vdW-DF yield nearly the same formation energies for configurations c_3 , c_4 , c_5 , c_8 , c_{10} , c_{13} and c_{16} . The formation energy differences ΔE_f between GGA and vdW-DF in configuration c_1 is slightly more than 0.05 eV, but less than 0.03 eV in configuration c_4 , c_5 and c_{10} (see Fig. 3). Our LDA calculation gives small positive formation energy in configuration c_1 , whereas both vdW-DF and GGA yields a negative enthalpy of formation suggesting that configuration c_1 may form spontaneously. The low formation energy from vdW-DF in c_1 suggests that the binding force between the molecular hydrogen and the bilayer graphene arises from van der Waals interaction because the H₂ dimer is

physisorbed above layer A (see Fig. 2(a)).

The hydrogen adatoms are all chemisorbed in the relaxed state, except in configurations c_1 , c_{12} , c_{14} and c_{15} , as shown in Table II. The local structures of competing low energy structures are shown in Fig. 4 for the relaxed states. These suggest that the properties of the hydrogenated bilayer graphene configurations are sensitive to the location of the carbon atom in the unit cell, and on the hydrogen adsorption site geometries. The top layers in configurations c_2 and c_7 are equivalent to the stable structure of monolayer graphene under the condition of 100 % H-coverage. The resulting graphane structure is known to be stable both theoretically²⁴ and experimentally.¹⁵ In the theoretical study of Sofo *et al.*,²⁴ the GGA functional predicted short, and strong covalent bonds between hydrogen and carbon atoms.

Fig. 3 shows that the most stable configuration of hydrogen adatoms on the bilayer graphene (*i.e.* with the lowest formation energy) is obtained when sites b_{above} a'_{below} are fully saturated (Table II). The resulting local structure is equivalent to the bilayer analogue of graphane - a fully hydrogenated graphene monolayer. Table II shows the properties of coupled structures of pristine and hydrogenated bilayer graphene after relaxation. All the XC functionals give the same bond length ($l_{C-C} = 1.429$ Å) and bond angle ($\theta = 120^\circ$) in the pristine bilayer. Similarly, hydrogen adsorption causes an increase in mean bond-length towards the value of 1.51 Å expected in the diamond structure, while bond angles simultaneously decrease towards sp³-hybridized angle of 109.7°. The inclusion of non-local vdW corrections show minimal deviations in the bond length and bond angle of configuration c_8 relative to values expected in graphane^{24,39} while configurations c_2 and c_7 give slightly larger values (see Table III). Because the experimental value of the layer-layer separation in pristine bilayer is 3.35 Å³⁵ we conclude that LDA gives the most accurate bilayer separation, although in configurations c_2 and c_7 , it overestimates it by 10.3 %. Within vdW-correction, the interlayer distance is both underestimated; 3.29 Å (vdW-DF2C09 $_x$) and 3.27 Å (vdW-DFC09 $_x$), and overestimated; 3.51 Å (vdW-DF) and 3.59 Å (vdW-DF2) in the pristine bilayer. Both vdW- schemes and GGA overestimates the layer-layer distance of the bilayer by a maximum of 21.4 % and 41.3 % respectively.

Table III shows significantly reduced interlayer distance in configuration c_8 after structural relaxation. Configurations c_2 and c_8 exhibit the largest deviations in bond angles, θ . Their low total energies, and heats of formation at 0 K after correcting for vdW interactions (see Fig. 3) suggest that their high relative stability could be ascribed to puckering- mechanism, in good agreement with Sofo *et al.*²⁴ Thus, although the adsorption of hydrogen atoms on a single sublattice of either plane A or plane B of the bilayer graphene structure does not result in any stable structure, hydrogenating both external faces, specifically at site b_{above} a'_{below} (see Table II) gives rise to the most stable configuration. Our results confirms the

TABLE III. The calculated properties of selected competing structural configurations: the distances between two bonded carbon atoms l_{C-C} (in Å), the bond angles θ_{C-C-C} (in degrees) and the interlayer distances d_0 (in Å). The l_{C-C} bond lengths are quoted to three decimal places to demonstrated the similarity of the results for the six exchange correlation functionals.

Parameters	Functionals	Top (bottom) layers of structural configurations							
		Pristine		2		7		8	
		T	B	T	B	T	B	T	B
l_{C-C}	vdW-DF	1.429 (1.429)	1.498 (1.429)	1.498 (1.429)	1.498 (1.429)	1.504 (1.504)	1.504 (1.504)	1.504 (1.504)	1.504 (1.504)
	vdW-DF2	1.429 (1.429)	1.501 (1.429)	1.501 (1.429)	1.505 (1.429)	1.514 (1.514)	1.514 (1.514)	1.514 (1.514)	1.514 (1.514)
	vdW-DF C09 _x	1.429 (1.429)	1.503 (1.429)	1.503 (1.429)	1.503 (1.429)	1.513 (1.513)	1.513 (1.513)	1.513 (1.513)	1.513 (1.513)
	vdW-DF2 C09 _x	1.429 (1.429)	1.504 (1.429)	1.504 (1.429)	1.504 (1.429)	1.512 (1.512)	1.512 (1.512)	1.512 (1.512)	1.512 (1.512)
	LDA	1.420 (1.420)	1.500 (1.421)	1.500 (1.421)	1.500 (1.421)	1.509 (1.509)	1.509 (1.509)	1.509 (1.509)	1.509 (1.509)
	GGA	1.429 (1.429)	1.504 (1.430)	1.504 (1.430)	1.504 (1.430)	1.512 (1.512)	1.512 (1.512)	1.512 (1.512)	1.512 (1.512)
θ_{C-C-C}	vdW-DF	120.0 (120.0)	110.4 (120.0)	110.4 (120.0)	110.4 (120.0)	109.8 (109.8)	109.8 (109.8)	109.8 (109.8)	109.8 (109.8)
	vdW-DF2	120.0 (120.0)	110.9 (120.0)	110.9 (120.0)	110.7 (120.0)	109.8 (109.8)	109.8 (109.8)	109.8 (109.8)	109.8 (109.8)
	vdW-DF C09 _x	120.0 (120.0)	110.9 (120.0)	110.9 (120.0)	110.9 (120.0)	109.9 (109.9)	109.9 (109.9)	109.9 (109.9)	109.9 (109.9)
	vdW-DF2 C09 _x	120.0 (120.0)	110.8 (120.0)	110.8 (120.0)	110.8 (120.0)	110.0 (110.0)	110.0 (110.0)	110.0 (110.0)	110.0 (110.0)
	LDA	120.0 (120.0)	111.2 (120.0)	111.2 (120.0)	111.2 (120.0)	110.3 (110.3)	110.3 (110.3)	110.3 (110.3)	110.3 (110.3)
	GGA	120.0 (120.0)	110.8 (120.0)	110.8 (120.0)	110.8 (120.0)	109.9 (109.9)	109.9 (109.9)	109.9 (109.9)	109.9 (109.9)
d_0	vdW-DF	3.51	4.06	4.06	4.14	1.57	1.57	1.57	1.57
	vdW-DF2	3.59	3.96	3.96	4.05	1.58	1.58	1.58	1.58
	vdW-DF C09 _x	3.27	3.69	3.69	3.87	1.58	1.58	1.58	1.58
	vdW-DF2 C09 _x	3.29	3.86	3.86	3.87	1.56	1.56	1.56	1.56
	LDA	3.33	3.69	3.69	3.88	1.55	1.55	1.55	1.55
	GGA	4.10	4.73	4.73	4.85	1.56	1.56	1.56	1.56

recent observation³⁹ that adsorption of hydrogen on the both faces of bilayer graphene, at 50% coverage, causes the transformation of the structure to the tetrahedral geometry. In this H-mediated transformation, both the top and bottom layer carbon atoms come into sufficiently close proximity to allow interlayer chemical bonds to form between them. This is also accompanied by a change in the hybridization of the carbon bonds from sp^2 to sp^3 resulting in increased mean bond length from 1.42Å in pristine bilayer to 1.51Å expected in the diamond structure. The low formation energy observed in configuration c_8 suggests that the interlayer bond-formation mechanism favors the binding of hydrogen atoms to the two external faces of the bilayer in order to form the interlayer bond. As suggested by Leenaerts *et al.*,³⁹ the implication is that both sides of the bilayer graphene has to be exposed to hydrogen for the transformation to occur because graphene is hard to penetrate.^{63,64}

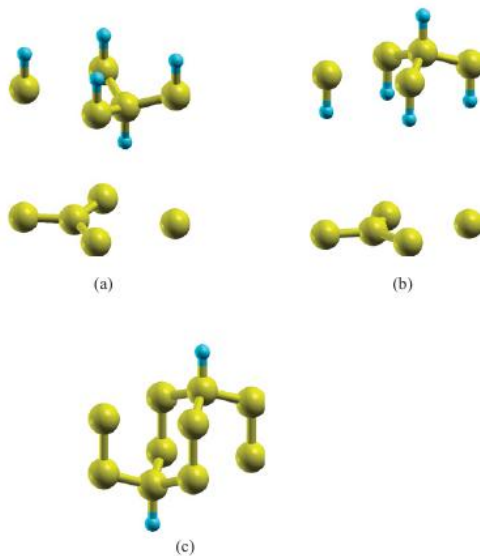


FIG. 4. Relaxed geometries of competing low-energy structures of coupled bilayer graphene at 50% hydrogen coverage showing configurations: (a) c_2 , (b) c_7 , and (c) c_8 .

In configurations c_2 and c_7 , the bond lengths in the hydrogen-free bottom layer still retain their graphitic values of 1.42 Å. The difference between the H-adsorption sites in configurations c_2 and c_7 (see Fig. 4) results in non-trivial differences in the interlayer separation in the two configurations (as shown in Table III). All the exchange-correlation functionals consistently give wider interlayer separation in configuration c_7 compared to configuration c_2 . The physical justification for the wider interlayer in configuration c_7 is unclear, since the bottom layer in both structures are unhydrogenated. Nevertheless, it suffices to attribute the wide interlayer separation in configuration c_7 to the fact that the interlayer adsorption of the

hydrogen atom directly on top of the bottom layer carbon gives rise to a higher local displacement of the top layer compared to configuration c_2 . Since the interlayer hydrogen atom in configuration c_2 is not located on top of any atom of the bottom layer, the net interatomic repulsion is minimal, relative to configuration c_7 .

Boukhalov *et al.*¹⁹ showed that adsorbing a single hydrogen atom on single layer graphene yields a positive activation energy, and thus its chemisorption energy is not favorable. In Fig. 3, configurations with high formation energies (*i.e.*, $E_f > 0.4$ eV) are considered metastable, and therefore are unstable at 0 K relative to configurations c_2 , c_7 , and c_8 . It is relevant to note that configurations c_4 and c_{10} are equivalent, with the hydrogen adsorption sites swapped. Because the formation energy of all the metastable configurations (see Fig. 3) are less than 1.00 eV relative to configurations c_2 , c_7 and c_8 , and consider that formation energies are determined with respect to graphite and molecular hydrogen, we conclude that it is distinctly possible to form these metastable configurations under finite temperature conditions if the temperature is high enough to overcome their formation barriers.¹⁹

In the case of single graphene layer, the effects of the hydrogen adatoms are balanced by the simultaneous adsorption of hydrogen atoms both above and below the layer. The observed instability in configuration c_4 , c_5 and c_{10} arises from the high chemisorption energy expected in a single H-adatom configuration. This is due to the absence of the hydrogen adatom on the opposite face of the top, and bottom, of monolayers. Otherwise, the presence of such configuration deviates from the 50% coverage hydrogen adatoms on bilayer graphene. Therefore, the absence of the single layer distortion-balancing effect must be responsible for the observed structural instability. The effect of this instability is clearly exhibited in the inconsistency in C-C bond lengths within the top and bottom layers of the metastable configurations.

In the electrostatic approximation, the top and bottom layers in the metastable configurations (*i.e.*, c_4 , c_5 and c_{10}) can be considered to carry charges q_1 , q_2 and q_3 respectively, of the same magnitude. This implies that they carry equal charges on both layers, and are each separated by the corresponding interlayer distances. For the stable configurations, Table III shows that the interlayer separation varies significantly from the equilibrium value ($d_0 = 3.35$ Å), after relaxation. These variations arise from the competition between the Coulombic repulsion, the puckering effect of hydrogen, and van der Waals interactions between the polar layers. An effective polarity develops in the metastable configurations because the two unhydrogenated carbon atoms in the top and bottom layers are indirect. This implies that a large number of symmetry raising Jahn-Teller distortions are necessary to change the interplanar ordering from the Bernal (AB) stacking to the simple (AA) stacking sequence.

We therefore suggest that the high stability of competing low-energy, coupled hydrogenated bilayer, structures

arise because the hydrogen adatoms are chemisorbed on indirect carbon atoms. Because the indirect carbon atoms are not positioned directly above each other along the c -axis, the effective repulsion between the carbon ion cores is minimized. The structural relaxation effects of the hydrogenation reduces the effective interlayer separation, such that $d \ll d_0$ as shown in Table III. The reduced interlayer separation therefore brings all the direct carbon atoms into sufficiently close contact, to allow the overlap of the atomic wave functions. This therefore creates strong C-C bonds due to the hydrogen-induced rehybridization of the atomic orbitals. Moreover, the interlayer separation in c_8 is equivalent to the C-C bond-length in the diamond structure. We therefore conclude that configuration c_8 represents a viable template for synthesizing nanodiamonds from graphene by hydrogenation. This is consistent with the observation of the formation of full sp^3 -hybridized structure from hydrogen adsorption on bilayer graphene.³⁹

C. Electronic properties

Fig. 5(a)-(d) shows the band structures of pristine bilayer graphene from the four forms of the non-local vdW-functionals. The electronic states are labeled at high symmetry points of the Brillouin zone with reference to the Fermi level, in each case. These show a conical dispersion at the Γ -point, and a parabolic dispersion at the K -point, as expected. There are four π -bands which nearly meet at the K -point. The highest occupied molecular orbitals (HOMO) and lowest unoccupied molecular orbitals (LUMO) levels nearly coincide at Brillouin zone point K giving rise to zero-band gap. Fig. 5 show that the four vdW-functionals give similar band structures for pristine bilayer graphene. Despite the similarities in the band structure, subtle differences are observed in the dependence of band energies on Brillouin zone direction ($E(k)$ dispersion) and energy eigenvalues at high symmetry points. The agreement of the vdW-interaction corrected band structures with LDA and GGA band structures is qualitative because although the $E(k)$ dispersion is correctly predicted, slight differences are observed in the band energies at high-symmetry points. Table IV shows the eigenvalues of the HOMO and LUMO levels in the pristine bilayer relative to the Fermi level calculated using the different functionals. After correcting for vdW-interactions, the maximum and minimum eigenvalues of the HOMO (K_{1v}) /LUMO (K_{1c}) level are 1.38 eV (vdW-DF2) and 1.21 eV (vdW-DFC09_x) in the pristine bilayer. The difference between the vdW-DF and vdW-DF2C09_x eigenvalues for both HOMO and LUMO levels is 0.02 eV.

We have further investigated how the adsorbed hydrogen alters the electronic structures of bilayer graphene in all the structural configurations considered. For the pristine bilayer graphene, and for configurations c_1 , c_2 , c_7 and c_8 , the band energies decrease significantly for all

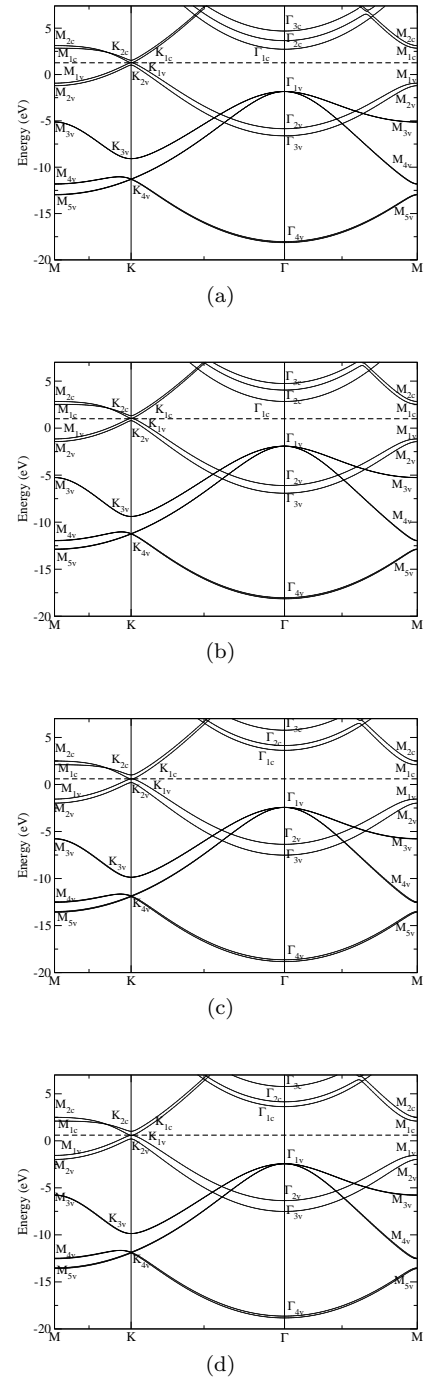


FIG. 5. Electronic band structure of pristine bilayer graphene calculated from four vdW-DF functionals: vdW-DF (a), vdW-DF2 (b), vdW-DFC09_x (c), and vdW-DF2C09_x (d). The Fermi level is marked by the dotted line.

the functionals. Nevertheless, the HOMO/LUMO levels in configurations c_2 and c_7 are the same for all functionals, and coincide at point K in the Brillouin zone. These configurations show semimetallic behavior except for configuration c_8 , where there is an energy gap between the Γ_{1v} and Γ_{1c} levels. From Table IV, the calculated band gap (at Γ -point) in configuration c_8 is 2.80

eV (vdW-DF), 2.61 eV (vdW-DF2), 2.91 eV (vdW-DFC09_x), 2.90 eV (vdW-DF2C09_x), 2.89 eV (LDA) and 3.09 eV (GGA), respectively. It is noted in particular that the LDA and GGA energy gaps are in agreement with previous results.³⁹ We therefore conclude that use of the Cooper exchange functional (C09_x) in vdW-DF and vdW-DF2 has very minimal influence on the band gap of configuration c_8 . The implication is that vdW interaction is not significant in configuration c_8 because of the formation of strong interlayer carbon bonds.

We also investigate the alignment of the hydrogen-induced energy bands in bilayer graphene. Because the electronic structures from LDA, GGA and the four schemes for vdW interaction correction are similar, we only show the vdW-DF band structures of selected hydrogenated configurations in Fig. 6.

In configuration c_1 , the physisorption does not alter the physical properties of the bilayer structure. However, in comparison with the pristine band structure, there are two extra bands due to hydrogen. These are denoted in Fig. 6(a) by K_{3v} and K_{3c} . The extra bands are attributed H-H bonding in the H₂-dimer. The K_{3v} band arises from the σ -bonding state between the two H 1s-states, while K_{3c} is an anti-bonding state. Nevertheless, the resulting structure is semimetallic. As seen in Sec.III(B), configurations c_2 and c_7 are similar - differing only in terms of their H-adsorption sites. In Table IV, the energy difference at K_{1v} for configurations c_2 and c_7 is less than 0.01 eV. However configuration c_7 has a slightly lower Fermi energy compared to configuration c_2 . Hence, we show the band structure for configuration c_7 in Fig. 6(b) for comparison with other configurations. In contrast with the pristine band structure, there are two linearly-dispersed bands instead of the four bands coinciding at point K_1 . This also shows that the system is semimetallic. This same trend has also been seen experimentally by Nourbakhsh *et al.*⁶⁵ for oxygen adatoms on bilayer graphene. We find that by fully saturating the top layer in configuration c_7 , the two π -bands at point K reduce to one (see Fig. 6(b)). Fig. 6(c) shows that configuration c_8 gives rise to a wide band gap at point K . The relaxed geometry of configuration c_8 (see Fig. 4(c)) shows that the network structure is fully saturated. Because the interplanar C-C bond length (see Table III) is significantly reduced, strong sp^3 hybridized bonds form between neighboring C atoms and break the symmetry of the π -bands. The band structures in configurations c_4 , c_5 and c_{10} are the same, despite the differences in the positions of the adsorbed hydrogen atoms after relaxation. These are presented in Fig. 6(d), to show metallic transport at 0 K in these configurations because there are no HOMO and LUMO levels due to bands crossings at their Fermi levels.

The metastable configurations yield longer C-H bond lengths, and their band structures show metallic transport properties. We also investigate the influence of the

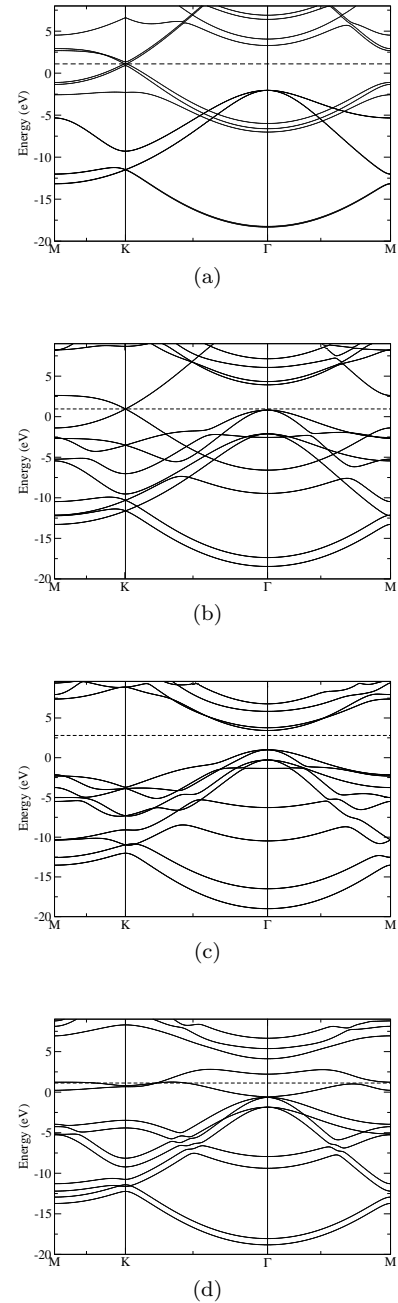


FIG. 6. The vdW-DF electronic band structure of c_1 (a); c_7 (b); c_8 (c); and c_{10} (d). The Fermi level is marked by the dotted line

C-H bond length on the electronic properties of configuration c_8 . Fig. 7 shows the variations in band gap for the six XC functionals as a function of the C-H bond length. At the equilibrium C-H bond length (1.10 Å), all six functionals consistently give maximum band gaps. We find that the vdW-DF yields higher band gaps for stretched C-H bonds while compressed C-H bonds yield low band gaps. By contrast, the LDA and GGA give an opposing trend because the compression (or stretching) of C-H bonds give rise to higher (or lower) energy gaps.

TABLE IV. The HOMO and LUMO eigenvalues (in meV) of structural configurations at high-symmetry points.

Electronic states	Configurations	k-point	vdW-DF	vdW-DF2	vdW-DF	C09 _x	vdW-DF2	C09 _x	vdW-DF2	C09 _x	LDA	GGA
	pristine	K_{1v}	1.26	1.38	1.21	1.28	1.21	1.28	1.09	1.32	1.04	1.32
	1	K_{1v}	1.10	1.09	1.07	1.09	1.07	1.09	0.89	1.19	0.89	1.19
	2	K_{1v}	0.67	0.75	0.85	0.86	0.85	0.86	0.69	0.95	0.69	0.95
	7	K_{1v}	0.65	0.71	0.83	0.84	0.83	0.84	0.71	0.95	0.71	0.95
HOMO level	8	Γ_{1v}	0.78	0.59	0.61	0.69	0.61	0.69	0.91	1.10	0.91	1.10
	pristine	K_{1c}	1.26	1.38	1.21	1.28	1.21	1.28	1.09	1.32	1.04	1.32
	1	K_{1c}	1.10	1.09	1.07	1.09	1.07	1.09	0.89	1.19	0.89	1.19
	2	K_{1c}	0.67	0.75	0.85	0.86	0.85	0.86	0.69	0.95	0.69	0.95
	7	K_{1c}	0.65	0.71	0.83	0.84	0.83	0.84	0.71	0.95	0.71	0.95
LUMO level	8	Γ_{1c}	3.58	3.20	3.52	3.59	3.52	3.59	3.78	4.19	3.78	4.19

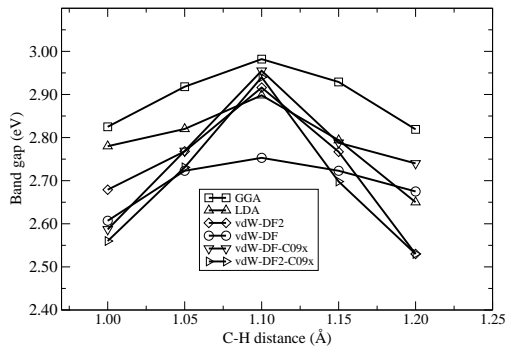


FIG. 7. Band gap of configuration c_8 as a function of C-H bond lengths predicted from six exchange-correlation functionals.

The GGA predicts larger band gaps in configuration c_8 for all C-H bond lengths. At the equilibrium C-H bond length vdW-DF yield the band gap. The vdW-DF2C09 $_x$ functional predicts the lowest band gaps when the C-H bond lengths are stretched and, or compressed maximally. Both vdW-DF2 and vdW-DF2C09 $_x$ give the same band gap (2.53 eV) when the bonds are fully stretched to 1.20 Å, but show a significant difference of 0.15 eV for compressed bonds.

IV. CONCLUSIONS

This paper predicts, and characterizes the possible structural configurations for the adsorption of hydrogen atoms on bilayer graphene. Using different exchange-correlation functionals, the relative stabilities and electronic properties of the hydrogen-adsorbed bilayer graphene are explored at 0 K. We find that the different forms of the vdW-interaction corrections perform best in relaxed configurations where the H₂ dimer is physisorbed, and the graphene bilayers are decoupled. On the other hand, the LDA performs best in configurations where the bilayer graphene is coupled in the relaxed state, and the hydrogen atoms are chemisorbed. Our analyses of the formation energies show that six of the configurations can form spontaneously. Because of the low, albeit

positive, heats of formation in the metastable configurations, we suggest that their formation can be achievable by activation. The spontaneous formation of the lowest energy configurations is strongly dependent on the arrangement of the adsorbed hydrogen atoms. It is noted that apart from configuration c_1 , this spontaneous formation only occurs when the top layer of carbon atoms is fully saturated, leaving the bottom layer completely unhydrogenated, or when both top and bottom layers are partially hydrogenated. The partial hydrogenation of both the top and bottom layers is found to result in a non-reversible transformation of the graphenic hexagonal structure to local diamond, tetrahedral, structure. This H-induced local reconstruction results in shortened C-H bonds and a considerable buckling of the tetrahedral structure. Relatively longer C-H bonds are obtained in configurations that display non-spontaneous formation, and their local structures are only slightly buckled.

We conclude that hydrogen atoms adsorbed on the top and bottom faces within the interlayer region causes considerable interlayer repulsion, which leads to increased interlayer distances (see Table III). This suggests hydrogen intercalation as a means of exfoliating graphene. The relatively more stable competing configurations exhibit either semi-metallic or insulating properties, whereas all the unstable configurations are metallic. We find that configuration c_8 results in an insulator, displaying a wide band gap. For this structure, the GGA yields the largest band gap. It is therefore concluded that no single exchange-correlation functional is able to describe the energetics, stability and local structure properties of all the configurations consistently.

ACKNOWLEDGMENTS

R.E.M. is grateful to the National Research Foundation (NRF) and the University of Pretoria for financial support. A.M.U. acknowledges financial support from the University of Pretoria under E2020 Project No. 5. N.C. thanks the University of Pretoria and National Institute of Theoretical Physics for financial support.

* aniekan.ukpong@up.ac.za

¹ K. S. Novoselov, A. K. Geim, S. V. Morozov, D. Jiang, Y. Zhang, S. V. Dubonos, I. V. Grigorieva, and A. A. Firsov, *Science* **306**, 666 (2004).

² A. K. Geim and K. S. Novoselov, *Nature Mater.* **6**, 183 (2007).

³ P. R. Wallace, *Phys. Rev.* **71**, 622 (1947).

⁴ K. S. Novoselov, A. K. Geim, S. V. Morozov, D. Jiang, Y. Zhang, M. I. Katsnelson, S. V. Dubonos, I. V. Grigorieva, and A. A. Firsov, *Nature (London)* **438**, 197 (2005).

⁵ Y. Zhang, Y. W. Tan, H. L. Stormer, and P. Kim, *Nature (London)* **438**, 201 (2005).

⁶ A. H. Castro, F. Guinea, N. M. R. Peres, K. S. Novoselov, and A. K. Geim, *Rev. Mod. Phys.* **81**, 109 (2009).

⁷ F. Schedin, A. K. Geim, S. V. Morozov, E. W. Hill, P. Blake, M. I. Katsnelson, and K. S. Novoselov, *Nature Mater.* **6**, 652 (2007).

⁸ M. Terrones, B. R. Botello-Mendez, J. Campos-Delgado, F. Lopez-Urias, Y. I. Vega-Cantu, F. J Rodriguez-Macias, A. L. Elias, E. Munoz-Sandoval, A. G. Cano-Marquez, J. C. Chalier, and H. Terrones, *Nano Today* **5**, 351 (2010).

⁹ J. A. Yan, L. Xian, and M. Y. Chou, *Phys. Rev. Lett.* **103**, 086802 (2009).

¹⁰ X. S. Wu, M. Sprinkle, X. B. Li, F. Ming, C. Berger, and

- W. A. de Heer, Phys. Rev. Lett. **101**, 026801 (2008).
- ¹¹ I. Jung, D. A. Dikin, R. D. Piner, and R. S. Ruoff, Nano Lett. **8**, 4283 (2008).
 - ¹² Z. Luo, P. M. Vora, E. J. Mele, A. T. C. Johnson, and J. M. Kikkawa, Appl. Phys. Lett. **94**, 111909 (2009).
 - ¹³ R. Balog, B. Jorgensen, L. Nilsson, M. Andersen, E. Rienks, M. Bianchi, M. Fanetti, E. Laegsgaard, A. Baraldi, S. Lizzit, Z. Sljivancanin, F. Besenbacher, B. Hammer, T. G. Pedersen, P. Hofmann, and L. Hornekaer. Nature Mater. **9**, 315 (2010).
 - ¹⁴ A. Savchenko, Science **323**, 589 (2009).
 - ¹⁵ D. C. Elias, R. R. Nair, T. M. G. Mohiuddin, S. V. Morozov, P. Blake, M. P. Halsall, A. C. Ferrari, D. W. Boukhvalov, M. I. Katsnelson, A. K. Geim, and K. S. Novoselov, Science. **323**, 610 (2009).
 - ¹⁶ Y. H. Lu, W. Chen, Y. P. Feng, and P. M. He, J. Phys. Chem. B **113**, 2 (2009).
 - ¹⁷ I. Zanella, S. Guerini, S. B. Fagan, J. MendesFilho, and A. G. SouzaFilho, Phys. Rev. B **77**, 073404 (2008).
 - ¹⁸ R. M. Ribeiro, N. M. R. Peres, J. Coutinho, and P. R. Briddon, Phys. Rev. B **78**, 075442 (2008).
 - ¹⁹ D. W. Boukhvalov, M. I. Katsnelson, and A. I. Lichtenstein, Phys. Rev. B **77**, 035427 (2008).
 - ²⁰ S. Lebegue, M. Klintonberg, O. Eriksson, and M. I. Katsnelson, Phys. Rev. B **79**, 245117 (2009).
 - ²¹ E. J. Duplock, M. Scheffler, and P. J. D. Lindan, Phys. Rev. Lett. **92**, 225502 (2004).
 - ²² D. W. Boukhvalov and M. I. Katsnelson, Phys. Rev. B **78**, 085413 (2008).
 - ²³ N. Z. Lu, Z. Y. Li, and J. L. Yang, J. Phys. Chem. C **113**, 16741 (2009).
 - ²⁴ J. O. Sofo, A. S. Chaudhari, and G. D. Barber, Phys. Rev. B **75**, 153401 (2007).
 - ²⁵ L. Sun, Q. X. Li, H. Ren, H. B. Su, Q. W. Shi, and J. L. Yang, J. Chem. Phys **129**, 074074 (2008).
 - ²⁶ Y. W. Son, M. L. Cohen, and S. G. Louie, Phys. Rev. Lett **97**, 216803 (2006).
 - ²⁷ M. Y. Han, B. Ozyilmaz, Y. Zhang, and P. Kim, Phys. Rev. Lett **98**, 206805 (2007).
 - ²⁸ F. Ding, Phys. Rev. B **72**, 245409 (2005).
 - ²⁹ G. D. Lee, C. Z. Wang, E. Yoon, N. M. Hwang, D. Y. Kim, and K. M. Ho, Phys. Rev. Lett. **95**, 205501 (2005).
 - ³⁰ M. T. Lusk and L. D. Carr, Phys. Rev. Lett. **100**, 175503 (2008).
 - ³¹ S. C Pradhan and J. K. Phadikar, Phys. Lett. A **373**, 1062 (2009).
 - ³² P. Lu, Z. Zhang, and W. Guo, Phys. Lett. **373**, 3354 (2009).
 - ³³ W. Choi, I. Lahiri, R. Seelaboyina, and Y. S. Kang, Crit. Rev. Solid State and Mater Sci. **35**, 52 (2010).
 - ³⁴ H. Min and A. H. MacDonald, Phys. Rev. B **77**, 155416 (2008).
 - ³⁵ T. Ohta, A. Bostwick, T. Seyller, K. Horn, and E. Rotenberg, Science **313**, 951 (2006).
 - ³⁶ Z. Q. Luo, T. Yu, K. J. Kim, Z. H. Ni, Y. M. You, S. H. Lim, Z. X. Shen, S. Z. Wang, and J. Y. Lin, ACSNANO **3**, 1781 (2009).
 - ³⁷ K. S. Subrahmanyam, P. Kumar, U. Maitra, A. Govindaraj, K. P. Hembaram, U. V. Waghmare, and C. N. R. Rao, Proc. Nat. Acad. Sci. (USA) **108**, 2677 (2011).
 - ³⁸ M. Jaiswal, C. H. Lim, Q. Bao, C. T. Toh, K. P. LOh, and B. Ozyilmaz, ACSNANO **5**, 888 (2011).
 - ³⁹ O. Leenaerts, B. Partoens, and F.M. Peeters, Phys. Rev. B **80**, 245422 (2009).
 - ⁴⁰ S. M. Choi, S. H. Jhi, and Y. W. Son, Nano. Lett. **10**, 3486 (2010).
 - ⁴¹ P. L. de Andres, R. Ramirez, and J. A. Verges, Phys. Rev. B **77**, 045403 (2008).
 - ⁴² P. Giannozzi, S. Baroni, N. Bonini, M. Calandra, R. Car, C. Cavazzoni, D. Ceresoli, G. L. Chiarotti, M. Cococcioni, I. Dabo, A. Dal Corso, S. Fabris, G. Gougoussis, A. Kokalj, M. Lazzeri, L. Martin-Samos, N. Marzari, F. Mauri, R. Mazzarello, S. Paolini, A. Pasquarello, L. Paulatto, C. Sbraccia, S. Scandolo, G. Sclauzero, A. P. Seitsonen, A. Smogunov, P. Umari, and R. M. Wentzcovitch, J. Phys. Condens. Matter **21**, 395502 (2009).
 - ⁴³ J. P. Perdew and A. Zunger, Phys. Rev. B **23**, 5048 (1981).
 - ⁴⁴ J. P. Perdew, K. Burke, and M. Ernzerhof, Phys. Rev. Lett. **77**, 3865 (1996).
 - ⁴⁵ G. Roman-Perez and J. M. Soler, Phys. Rev. Lett. **103**, 096102 (2009).
 - ⁴⁶ M. Dion, H. Rydberg, E. Schroder, D. C. Langreth, and B. I. Lundqvist, Phys. Rev. Lett. **92**, 246401 (2004).
 - ⁴⁷ K. Lee, E. D. Murray, L. Kong, B. I. Lundqvist, and D. C. Langreth, Phys. Rev. B **82**, 081101 (2010).
 - ⁴⁸ E. D. Murray, K. Lee, and D. C. Langreth, J. Chem. Theory Comput. **5**, 2754 (2009).
 - ⁴⁹ J. P. Perdew and Y. Wang, Phys. Rev. B **33**, 8800 (1986).
 - ⁵⁰ V. R. Cooper, Phys. Rev. B **81**, 161104 (2010).
 - ⁵¹ P. E. Blochl, Phys. Rev. B **50**, 17953 (1994).
 - ⁵² H. J. Monkhorst and J. D. Pack, Phys. Rev. B **13**, 5188 (1976).
 - ⁵³ M. Methfessel, and A. T. Paxton, Phys. Rev. B **40**, 3616 (1989).
 - ⁵⁴ I. Hamada and M. Otani, Phys. Rev. B **82**, 153412 (2010).
 - ⁵⁵ H. Rydberg, M. Dion, N. Jacobson, E. Schroder, P. Hyldgaard, S. I. Simak, D. C. Langreth, and B. I. Lundqvist, Phys. Rev. Lett. **91**, 126402 (2003).
 - ⁵⁶ This value of interlayer distance is obtained as half of the geometrical parameter from Table I of Ref. 55.
 - ⁵⁷ S. D. Chakarova-Kack, E. Schroder, B. I. Lundqvist, and D. C. Langreth, Phys. Rev. Lett. **96**, 146107 (2006).
 - ⁵⁸ Y. Baskin and L. Mayer, Phys. Rev **100**, 544 (1955).
 - ⁵⁹ R. Zacharia, H. Ulbricht, and T. Hertel, Phys. Rev. B **69**, 155406 (2004).
 - ⁶⁰ L. X. Benedict, N. G. Chopra, M. L. Cohen, A. Zettl, S. G. Louie, and V. Crespie, Chem. Phys. Lett. **286**, 490 (1998).
 - ⁶¹ See Table SIV in the supplementary material of Ref. 54. Available online at: <http://link.aps.org/supplemental/10.1103/PhysRevB.82.153412>
 - ⁶² Note that this GGA-PBE data is obtained from dispersion-corrected atom-centred potential (DCAP) calculations.
 - ⁶³ J. S. Bunch, S. S. Verbridge, J. S. Alden, A. M. van der Zande, J. M. Parpia, H.G. Craighead, and P. L. McEuen, Nano Lett. **8**, 2458 (2008).
 - ⁶⁴ O. Leenaerts, B. Partoens, and F. M. Peeters, Appl. Phys. Lett. **93**, 193107 (2008).
 - ⁶⁵ A. Nourbakhsh, M. Cantoro, A. V. Klekachev, G. Pourtois, T. Vosch, J. Hofkens, M. H. van der Veen, M. M. Heyns, S. DeGendt, and B. F. Sels, J. Phys. Chem. C **115**, 16619 (2011).

Chapter 5

Van der Waals density-functional study of 100% hydrogen coverage on bilayer graphene

The work presented in this chapter has been published: R. E. Mapasha, R.C. Andrew and N. Chetty, *Computational Materials Science* 78 (2013) 1-8.

In this chapter, we use the newly developed exchange-correlation functionals to study various hydrogen configurations on bilayer graphene at 100% coverage. As mentioned earlier, previous studies only focused on hydrogenating the top and bottom external faces of the bilayer graphene, in this study, we consider also the hydrogenation of the interlayer faces. Detailed information for this study is given in the attached publication. This publication outlines the computational details used and the results that were obtained together with the conclusions that were drawn from the study.

Van der Waals density-functional study of 100% hydrogen coverage on bilayer graphene

R.E. Mapasha,^{1,*} R.C. Andrew,^{1,†} and N. Chetty^{1,2}

¹*Physics Department, University of Pretoria, Pretoria 0002, South Africa*

²*National Institute for Theoretical Physics, Johannesburg, 2000, South Africa*

(Dated: September 10, 2013)

We investigate all hydrogen configurations that exist in a 1×1 unit cell of bilayer graphene at 100% coverage to find the low energy competing configurations using density functional theory (DFT). Other unique configurations, obtained from a 2×1 supercell, are also investigated. The GGA-PBE functional and four variants of non-local van der Waals density functionals namely, vdW-DF, vdW-DF2, vdW-DF-C09_x, and vdW-DF2-C09_x are used to account for the exchange correlation effects. Ten unique hydrogen configurations are identified for 1×1 unit cell bilayer graphene, and nine of these structures are found to be energetically stable with three low energy competing configurations. One arrangement found to exist in both 1×1 and 2×1 cell sizes is the most energetically stable configuration of all considered. For some of the configurations identified from the 2×1 supercell, it is found that the effect of hydrogenation results in greatly distorted hexagonal layers resulting in unequal bond distances between the carbon atoms. Also, interaction between the hydrogen-decorated planes greatly affects the energetics of the structures. The vdW-DF-C09_x functional is found to predict the shortest interlayer distances for all the configurations, whereas the GGA-PBE functional predicts the largest. For the most energetically favorable configuration, hydrogenation is found to reduce the elastic properties compared with pristine bilayer graphene.

PACS numbers: 68.43.Bc, 68.43.Fg, 73.22.Pr

I. INTRODUCTION

Density functional theory (DFT) is one of the most reliable and widely used electronic structure methods. Its ability to correctly describe a wide range of condensed materials has attracted the attention of a large number of scientists and engineers. The well known local density approximation and generalized gradient approximation functionals (LDA and GGA-PBE) accurately describe covalent and ionic bonded networks, but fail to completely capture the effects of van der Waals (vdW) forces in complex systems. For the graphite structure, LDA gives a relatively good interlayer distance between layers but a poor binding energy, whereas GGA-PBE gives physically meaningless values.

To resolve these issues, scientists have made significant efforts in developing new exchange correlation functionals that are compatible with the Kohn Sham equations while incorporating the long-range effects of van der Waals forces.¹⁻⁷ One such functional was developed by Dion *et al.*¹ in 2004 and is known as the van der Waals density functional (vdW-DF). The vdW-DF functional consists of three exchange correlation energy terms, viz. (1) a non-local correlation energy E_c^{nl} given by

$$E_c^{nl} = \frac{1}{2} \int \int n(\mathbf{r})n(\mathbf{r}')\phi(\mathbf{r}, \mathbf{r}')d^3rd^3r', \quad (1)$$

where $\phi(\mathbf{r}, \mathbf{r}')$ is the vdW-DF kernel which depends on the distance $|\mathbf{r} - \mathbf{r}'|$, the charge density and its gradient, (2) the local-density approximation correlation term E_c^{LDA} and (3) the revised Perdew Burke and Enzerhof⁸ (revPBE) exchange energy term E_x^{revPBE} . Using the algorithm developed by Soler *et al.*,⁹ vdW-DF shows its

efficiency in describing a wide range of systems without demanding too much computational cost. Calculations for graphite indicate that vdW-DF correctly predicts the weak binding energy between layers but overestimates the interlayer distance when compared to experimental results. This overestimation is due to the repulsive nature of the revPBE exchange term. In 2010, Klimes *et al.*¹⁰ and Cooper¹¹ constructed a new exchange functional (C09_x) to replace the strongly repulsive revPBE exchange term. The resulting vdW-DF-C09_x functional shows an improvement in the calculated interlayer distance but an overestimation in the binding energy of graphitic systems, i.e. graphite and bilayer graphene.¹² In 2010, Lee *et al.*¹³ improved the non-local correlation term of vdW-DF to obtain better binding energies. This improved functional is called vdW-DF2 and contains a re-fitted Perdew-Wang PW86R exchange functional term.¹⁴ They later combined vdW-DF2 with C09_x to develop vdW-DF2-C09_x which addressed the overestimated interlayer distances and binding energies obtained with vdW-DF and vdW-DF-C09_x, respectively.^{12,13}

In this study, we investigate the performance of the vdW-DF2-C09_x functional to describe the energetics and structural properties of hydrogenated bilayer graphene and compare its performance to that of the GGA-PBE, vdW-DF, vdW-DF2, and vdW-DF-C09_x functionals. Bilayer graphene consists of two stacked graphene layers bonded together by vdW forces. Graphene, a free standing layer of graphite, has drawn the attention of many researchers following its synthesis by Novoselov *et al.* in 2004.¹⁵ Graphene and bilayer graphene are fascinating materials because of their unique electronic properties. The energy bands of single layer graphene at low energies

are described by a two dimensional Dirac equation with a linear energy-momentum dispersion near the K point of the Brillouin zone.^{16–22} The electrons are comparable to quasi-particles with an effective speed of 10^6 m/s, giving graphene excellent properties such as an anomalous quantum Hall effect (QHE) at room temperature and the ballistic transport of massless Dirac Fermions.^{17,19} In bilayer graphene, the π linear dispersion splits into two parabolic bands near the K point.^{23,24} This split is a result of the strong interlayer coupling between the stacked layers, and demonstrates the possibility of easily tuning the band structure.^{23–25} These novel structures form the backbone of future carbon based electronic devices.

The semi-metallic nature of these two materials limits their direct technological applications in as much as the fabrication of carbon based electronic devices is concerned. This issue of zero band gap has attracted much attention leading to efforts to engineer the band gap. Several methods have been employed to alter the electronic properties of these materials^{26–34,37,40} with adsorption^{35–50} being the most commonly used technique and hydrogen as the favored adatom. A wide band gap of about 3.5 eV has been observed experimentally⁴⁹ and calculated theoretically.^{38,41,50} Numerous studies have already been conducted on hydrogen atoms adsorbed on single layer graphene but there is little information about hydrogen on bilayer graphene. A possible reason for this could be the failure of the standard GGA-PBE functional to correctly describes the vdW forces binding the layers of the bilayer graphene structures.

Subrahmanyam *et al.*⁵¹ conducted some experimental studies of the adsorption of hydrogen on monolayer and few-layer graphene. Their spectroscopic studies revealed the existence of sp^3 re-hybridization bonding in the hydrogenated few-layer graphene. Jaiswal *et al.*⁵² used a combination of charge transport and Raman spectroscopy experiments to study the adsorption of hydrogen on bilayer graphene. Different degrees of hydrogenation were considered to examine the electronic properties of hydrogenated monolayer and bilayer graphene. They deduced that partially hydrogenated structures have weak insulating behavior and also that bilayer graphene is quite susceptible to adsorption of hydrogen atoms compared to single layer graphene. Lately, Wang *et al.*⁵³ performed experimental studies of the physisorption of H_2 molecules on graphene at low and high surface coverages. Their calculated heats of adsorption indicated that high surface coverage was favored leading them to conclude that graphene has a high hydrogen storage capability. Several theoretical studies on the hydrogenation of bilayer graphene have been considered at low coverages.^{41,54,55} Recently, Rohrer *et al.*⁵⁶ performed van der Waals density functional (vdW-DF) studies on the adsorption of hydrogen atoms on bilayer graphene and bulk graphite at 100% coverage. Their results demonstrated that vdW interactions can alter the electronic behavior in the Brillouin zone. They also found that the engineered band gap is caused by two geometry-induced

effects, viz. (1) the hybridization between unoccupied wavefunctions in the lowest conduction band, and (2) the modification of the electrostatic interaction between hybrid wavefunctions and the total density.

It is known that hydrogenation of single layer graphene at 100% coverage only allows for two hydrogen configurations, i.e. (1) all the hydrogen atoms are adsorbed above the layer, (2) half of the hydrogen atoms are above and the remaining half is adsorbed below arranged in an alternating pattern. This is true for a 1×1 unit cell that contains only two atoms, but when the cell is made larger there are many other possible configurations. In this study, we use the GGA-PBE, vdW-DF, vdW-DF2, and vdW-DF-C09_x, vdW-DF2-C09_x functionals to examine the structural properties for all the hydrogen configurations that can possibly exist in a 1×1 unit cell of bilayer graphene with 100% coverage and find the lowest energy competing configurations. Thereafter, we increase the size of the cell to 2×1 to show other energetically stable configurations at 100% that are not possible in the 1×1 cell. Lastly, the effect of hydrogen on the elastic properties of one of the most energetically favorable configurations is examined.

This paper is organized as follows: In section II we present the computational methodology and the parameters used. In section III, we discuss our results, and we summarize these results and draw conclusions in section IV.

II. METHODOLOGY

Our calculations were carried out using a plane-wave basis set and the projector augmented wave (PAW)⁵⁷ pseudopotential method as implemented in the PWscf code included in the QUANTUM ESPRESSO package.⁵⁸ The calculations were performed using the GGA-PBE,⁵⁹ vdW-DF, vdW-DF2, vdW-DF-C09_x and vdW-DF2-C09_x functionals. For the expansion of the wavefunctions, an energy cut-off of 500 eV was set for the plane wave basis. We used the Monkhorst-Pack scheme⁶⁰ with a grid of size $10 \times 10 \times 1$ to sample the Brillouin zone. For SCF self-consistency, an energy convergence threshold was set at 10^{-7} eV. The atoms were allowed to relax, using the conjugate gradient algorithm, until the forces were less than 0.002 eV/Å. We employed a 1×1 and 2×1 cell for the construction of the bilayer graphene structures, with a vacuum spacing of 30 Å to reduce the interactions between periodic, vertical bilayer graphene images. The equilibrium lattice constants and interlayer distances for pristine bilayer graphene were obtained using all the above mentioned functionals, and were found to be in agreement with previous results.^{55,61}

III. RESULTS AND DISCUSSION

A. Identification of possible hydrogen adatoms configurations on bilayer graphene

Fig. 1 shows (a) a 1×1 unit cell and (b) a 2×1 supercell for AB (Bernal) stacked bilayer graphene that we have used to identify possible hydrogen configurations. The labels (a, b, a' and b') show the possible distinct carbon atoms on the bilayer graphene. The symbols a_a and a_b show the hydrogen adsorbed at position x above and below the carbon atoms labelled a, etc. Since we consider 100% coverage, all the carbon atoms in each identified configuration are hydrogenated. By relaxing the ten unique configurations identified from the 1×1 unit cell (listed in Table I), we see that the relaxed configurations, apart from configurations C₇-C₉, appear to be completely different from their initial unrelaxed state because of the formation of H₂ dimers.

Hydrogen dimers occur for configurations where two hydrogen atoms are placed, on the same side, on top of the two distinct carbon atoms at positions x (in the unrelaxed state). Such configurations are severely energetically unstable in their unrelaxed state but are stabilized by the H₂ dimer effect after relaxation. During relaxation, these hydrogen atoms simultaneously detach from the layer and attract each other resulting in the formation of a H₂ dimer. Configurations C₃-C₆ yield interesting geometries because of the mixture of chemisorption and physisorption. We therefore perform a thorough investigation of these structures.

We further constructed the 2×1 supercell that contains four atoms per plane (layer) to examine the properties of other configurations that are not possible in a 1×1 unit cell. The configurations identified are referred to as C₁₁-C₁₆, also presented in Table I. Some of these configurations were first studied by Leenearns *et. al.*⁶² considering single layer graphene. In C₁₁-C₁₃, the chair, zigzag and boat conformers are observed as shown on Fig. 4, respectively. It must be mentioned that configurations C₁₄-C₁₆ contain combinations of pairs of the various conformers as presented in Table I. The energetics of these configurations are examined and discussed in the next section.

B. Stability analysis and structural properties

To examine the relative stabilities of the identified configurations, the formation energy of each configuration is calculated. The formation energy (E_f), is defined as the energy per atom of the hydrogenated bilayer graphene with respect to intrinsic graphene and the corresponding H₂ dimer, i.e. $E_f = [E_{H-b} - N_C \times E_G - N_H \times E_{H_2}] / N_C$, where E_{H-b} , E_G and E_{H_2} are the energies per atom of relaxed, hydrogenated bilayer graphene, intrinsic graphene, and a H₂ dimer, respectively. N_C and N_H denote the total number of carbon and hydrogen atoms in the 1×1

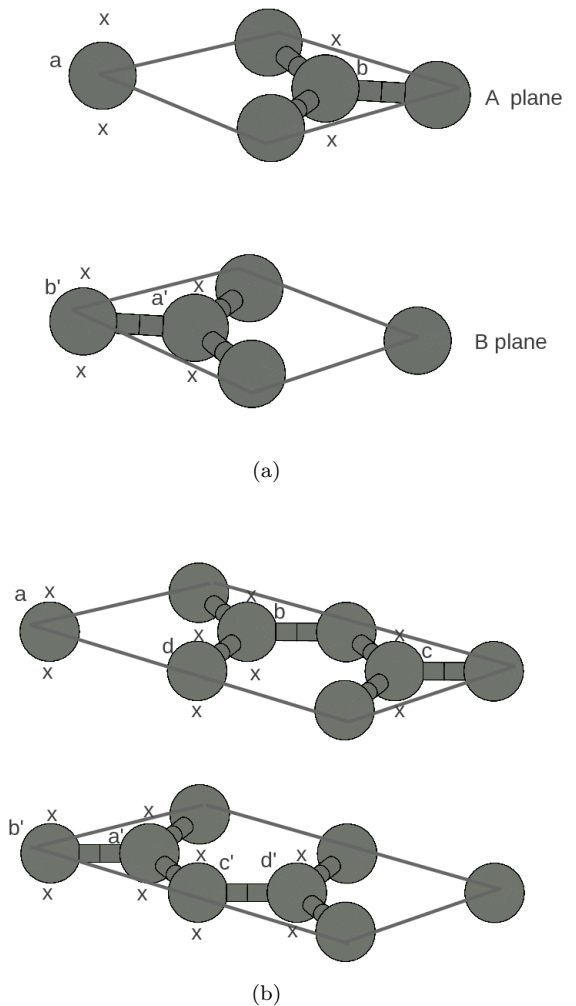


FIG. 1: The adsorption sites for hydrogen atoms on (a) 1×1 and (b) 2×1 cells of bilayer graphene. The labels on top and bottom layers depict the distinct carbon atoms on the AB stacked bilayer graphene. The letter x shows the exact positions of hydrogen atoms before relaxation.

unit cell respectively. Fig. 2 shows the formation energies per carbon for all identified hydrogen configurations on bilayer graphene using all five exchange correlation functionals. It is observed that for all identified configurations, the GGA-PBE functional predicts the highest formation energies as compared to those functionals with the non-local vdW density functional corrections.

Out of the ten uniquely identified configurations from 1×1 unit cell, Fig. 2 shows that, nine of these structures, C₁-C₉ are energetically favorable while C₁₀ is not. The relaxed local structure of C₁₀ shows that only one carbon atom on each plane is hydrogenated (see Fig. 3(e)). This configuration has the highest formation energy of 0.968 eV/atom (GGA-PBE), 0.865 eV/atom (vdW-DF), 0.699 eV/atom (vdW-DF2), 0.508 eV/atom (vdW-DF-C09_x) and 0.705 eV/atom (vdW-DF2-C09_x). It is there-

TABLE I: The hydrogen configurations on 1×1 and 2×1 supercell bilayer graphene at 100% coverage in the unrelaxed states. The subscripts a and b refer to positions above and below the adsorption sites, respectively, and B_u and B_n represent uniform and non-uniform buckled configurations.

Cell size	Index	Hydrogen configurations				Structural distortion		Formation of H_2
		PlaneA	PlaneB	PlaneA	PlaneB	PlaneA	PlaneB	
1×1	C ₁	$a_a b_a$	$a'_a b'_a$	Flat	Flat	Formed	Formed	
	C ₂	$a_a b_a$	$a'_b b'_b$	Flat	Flat	Formed	Formed	
	C ₃	$a_b b_a$	$a'_a b'_a$	B_u	Flat	Formed	Formed	
	C ₄	$a_a b_b$	$a'_a b'_a$	B_u	Flat	Formed	Formed	
	C ₅	$a_b b_a$	$a'_b b'_b$	B_u	Flat	Formed	Formed	
	C ₆	$a_a b_b$	$a'_b b'_b$	B_u	Flat	Formed	Formed	
	C ₇	$a_b b_a$	$a'_b b'_b$	B_u	B_u	None	None	
	C ₈	$a_b b_a$	$a'_a b'_b$	B_u	B_u	None	None	
	C ₉	$a_a b_b$	$a'_a b'_b$	B_u	B_u	None	None	
	C ₁₀	$a_b b_b$	$a'_a b'_a$	B_n	B_n	Formed	Formed	
2×1	C ₁₁	$a_b b_a c_a d_b$	$b'_b a'_a c'_b d'_a$	B_u	B_u	None	None	
	C ₁₂	$a_a b_b c_a d_b$	$b'_a a'_a c'_b d'_b$	B_n	B_n	None	None	
	C ₁₃	$a_b b_b c_a d_a$	$b'_b a'_a c'_a d'_b$	B_n	B_n	None	None	
	C ₁₄	$a_a b_b c_a d_b$	$b'_b a'_a c'_b d'_a$	B_n	B_u	None	None	
	C ₁₅	$a_a b_b c_a d_b$	$b'_b a'_a c'_a d'_b$	B_n	B_n	None	None	
	C ₁₆	$a_b b_a c_a d_b$	$b'_b a'_a c'_a d'_b$	B_u	B_n	None	None	

fore energetically expensive to experimentally synthesis C_{10} . The effects of the vertically oriented H_2 dimer physisorbed between the two planes does not reduce the formation energy of this structure. It is suggested that under conditions of finite temperature, structures similar to C_{10} may become energetically favorable.³⁸

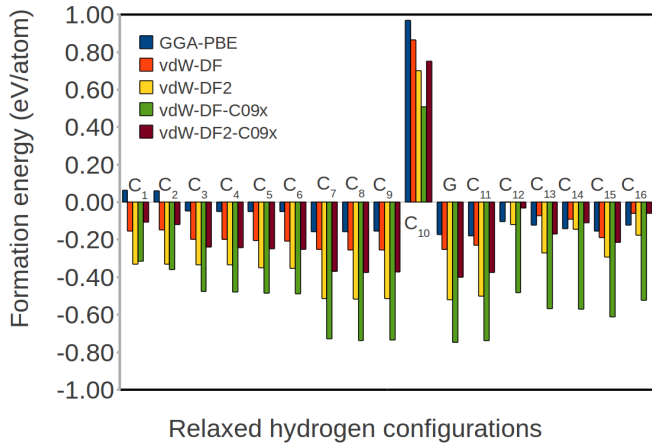


FIG. 2: The variation of formation energies with respect to identified configurations from 1×1 and 2×1 cells predicted by GGA-PBE, vdW-DF, vdW-DF2, vdW-DF-C09_x and vdW-DF2-C09_x functionals. The letter G stands for 1×1 graphane.

Fig. 2 shows that amongst all energetically favorable configurations, the employed exchange correlation functionals predict C_1 and C_2 to be less stable than C_3 - C_9 . It is observed that the adsorption occurring in configurations C_1 and C_2 is the physisorption of H_2 dimers as seen in Fig. 3 (a and b) whereas that in C_3 - C_9 is either chemisorption or both. The observed low formation energies in C_3 - C_9 arise from the planes where chemisorption has occurred. For configurations C_1 and C_2 , GGA-PBE gives the small, positive formation energies of 0.062 eV/atom and 0.059 eV/atom respectively whereas the non-local vdW density functional corrections give negative formation energies of -0.150 eV/atom (vdW-DF), -0.331 eV/atom (vdW-DF2), -0.314 eV/atom (vdW-DF-C09_x) and -0.106 eV/atom (vdW-DF2-C09_x) for C_1 and -0.156 eV/atom (vdW-DF), -0.331 eV/atom (vdW-DF2), -0.364 eV/atom (vdW-DF-C09_x) and -0.120 eV/atom (vdW-DF2-C09_x) for C_2 . These values indicate viable metastability of these two structures. Based on these formation energies, C_2 is more energetically favorable than C_1 . The presence of the H_2 dimer between the two graphene layers in C_1 , decouples the structure leading to a large interlayer separation of 7.92 Å (GGA-PBE), 6.55 Å (vdW-DF), 6.38 Å (vdW-DF2), 6.27 Å (vdW-DF-C09_x) and 6.31 Å (vdW-DF2-C09_x). The significant variation between the GGA-PBE functional and the vdW variants is attributed to the vdW force interaction arising between the observed H_2 dimer and the decoupled layers. In C_2 , the interlayer separation of 4.11 Å (GGA-PBE),

3.51 Å (vdW-DF), 3.49 Å (vdW-DF2), 3.28 Å (vdW-DF-C09_x) and 3.29 Å (vdW-DF2-C09_x) still retains the pristine (graphitic) value (see Fig. 5). The relative equilibrium interlayer distances Δd (calculated with respect to pristine bilayer graphene) of C_2 is effectively zero. We conclude that the H_2 dimers physisorbed outside the bilayer have no effect on the vdW forces holding the layers together.

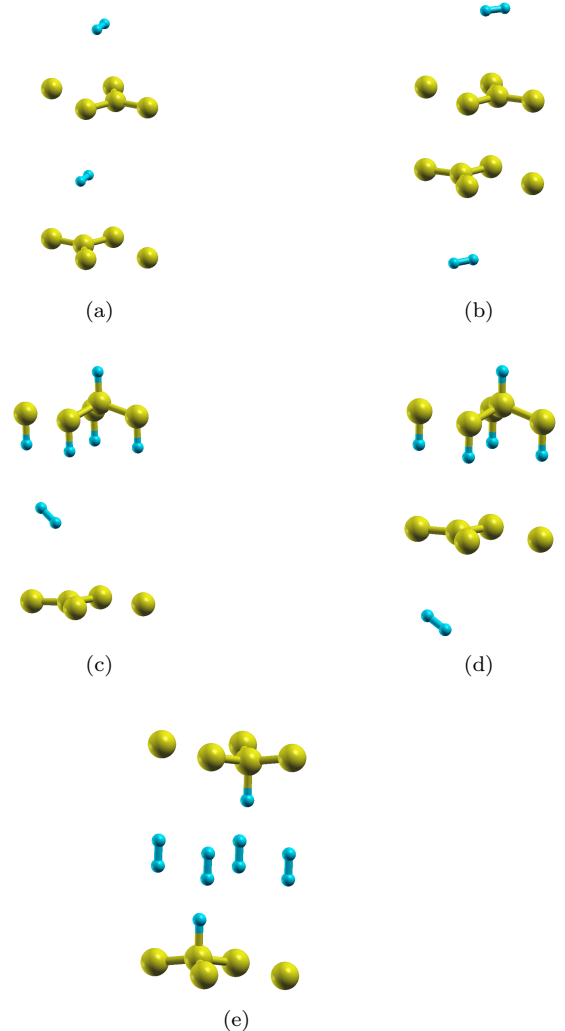


FIG. 3: The selected relaxed configurations showing the H_2 dimers physisorbed and atomic hydrogen chemisorbed on 1×1 unitcell bilayer graphene: (a) C_1 , (b) C_2 , (c) C_3 , (d) C_5 , (e) C_{10} .

In Fig. 2, it is observed that configurations C_3 - C_6 have less formation energies than C_1 and C_2 but higher than C_7 - C_9 . These configurations, i.e. C_3 - C_6 are grouped together because they have both chemisorption and physisorption. The strong covalent bond between the carbon and hydrogen atoms that causes a complete depuckering in plane A, and the weak vdW interactions between H_2 dimer and the flat plane B seen in Fig. 3(c and d) are responsible for the intermediate stabilities of these con-

figurations. It is important to note that configurations C_3 is equivalent to C_4 with the hydrogen adsorption sites on plane A swapped (see Table I). The three functionals vdW-DF, vdW-DF-C09_x and vdW-DF2-C09_x show that C_3 is 0.002eV/atom lower in formation energy than C_4 . Configuration C_5 is 0.001 eV/atom (GGA-PBE), 0.003 eV/atom (vdW-DF), 0.003 eV/atom (vdW-DF2), 0.004 eV/atom (vdW-DF-C09_x), 0.003 eV/atom (vdW-DF2-C09_x) lower in formation energy than C_6 . We therefore give a detailed discussion of the difference in properties between C_3 and C_5 .

From our calculated formation energy values, we observe that the energy of C_3 is higher than that of C_5 by 0.001 eV/atom (GGA-PBE), 0.006 eV/atom (vdW-DF), 0.015eV/atom (vdW-DF2), 0.006eV/atom (vdW-DF-C09_x), 0.005 eV/atom (vdW-DF2-C09_x). This difference in formation energy is not significant whereas the major difference is observed in the interlayer separations. Configuration C_3 is a decoupled structure with large interlayer separations of 12.67 Å (GGA-PBE), 7.86 Å (vdW-DF), 8.64 Å (vdW-DF2), 6.44 Å (vdW-DF-C09_x) and 6.75 Å (vdW-DF2-C09_x), caused by the effect of atomic hydrogen bonded to plane A and a physisorbed H_2 dimer between the layers. Configuration C_5 has an interlayer separation of 4.68 Å (GGA-PBE), 4.16 Å (vdW-DF), 3.98 Å (vdW-DF2), 3.97 Å (vdW-DF-C09_x) and 3.91 Å (vdW-DF2-C09_x). The relative interlayer distance Δd in configuration C_5 shows that the effect of atomic hydrogen adsorbed on plane A, within the interlayer region, increases the interlayer separation by only 0.58 Å (GGA-PBE), 0.65 Å (vdW-DF), 0.47 Å (vdW-DF2), 0.69 Å (vdW-DF-C09_x) and 0.62 Å (vdW-DF2-C09_x). We suggest that C_5 is still coupled, and therefore more stable than the decoupled configuration C_3 . This is also indicated by the coupled configuration C_2 being more stable than the decoupled C_1 . It suffices to mention that the effect of vdW interactions within bilayer graphene greatly affect the energetics of these systems.

In Table II, we present the variations in the distances between the H_2 dimers and the planes. The GGA-PBE functional predicts that the H_2 dimer binds at a distance of about 3.90 Å away from the layer (measured either inside (I) or outside (O) the bilayer). This value suggests that the dimer is further away from the layer compared to that predicted by non-local vdW corrections where the dimer is about 2.80 Å (which is in agreement with LDA results⁶³). It must be noted that the LDA results were obtained when a H_2 dimer was physisorbed on single layer graphene. Since it is well known that the H_2 dimer interacts with graphitic structures through a typical π -involved weak interaction, we expect the vdW functionals to predict better distances, particularly the recently developed vdW-DFs with the exchange functional (C09_x) of Cooper, namely, (vdW-DF-C09_x) and (vdW-DF2-C09_x). It has been observed that, in general, vdW-DF-C09_x and vdW-DF2-C09_x predict small distances.¹² These small values are attributed to the use of the exchange functional C09_x, since the vdW-DF correlation with in place

TABLE II: The calculated equilibrium distances d_{C-H_2} (in Å) between the hexagonal layers of 1×1 bilayer graphene and H_2 dimer for the selected configurations. The distance d_{C-H_2} is considered to be measured when the H_2 dimer is either inside (I) or outside (O) the bilayer graphene.

Functionals	Position	C_1	C_2	C_3	C_5	C_{10}
GGA-PBE	I	3.93		3.91		3.86
	O	3.98	3.96		3.99	
vdW-DF	I	3.00		3.01		3.50
	O	3.05	3.08		3.09	
vdW-DF2	I	2.86		2.90		3.31
	O	2.98	3.02		2.97	
vdW-DF-C09 _x	I	2.78		2.82		2.98
	O	2.86	2.85		2.86	
vdW-DF2-C09 _x	I	2.81		2.81		2.73
	O	2.87	2.87		2.85	

of the repulsive revPBE exchange term overestimates interlayer separations.¹² It is also observed in Table II that all the functionals predict the separation d_{C-H_2} measured inside the layers (I) to be less than the d_{C-H_2} measured outside (O). This is not surprising since at position (I), both layers are attempting to reach their equilibrium separation and are hindered by the presence of the dimer whereas at (O), the dimer is free to adjust its position away from the outer layer.

Fig. 2 shows that configurations C_7 - C_9 are the lowest energy competing geometries as compared to others. Atomic arrangements of these configurations show that all the hydrogen atoms are covalently bonded with the carbon atoms after relaxations. We also compare the formation energies of these configurations with that of graphane (a fully hydrogenated graphene monolayer where hydrogen atoms are arranged in an alternating pattern). It is noted in Fig. 2 that their formation energies are nearly the same. We further construct a 2×1 supercell of bilayer graphene to show that there are several physically interesting configurations that are not possible for a 1×1 unit cell. Six unique energetically favorable configurations are identified and presented in Table I. It is noted that configuration C_{11} has a similar hydrogen arrangement (chair-like) as C_7 - C_9 (see Fig. 4). All of these configurations have the same buckling, presented in Table I, and they are uniformly distorted (see Fig. 4). It is revealed that for the 1×1 unit cell, only one conformer (chair-like) of hydrogen is possible. It is clear that only C_{11} can be represented by both 1×1 unit cell and 2×1 supercell sizes. We also see in Fig. 2 that these configurations (C_7 - C_9 and C_{11}) have nearly the same formation energies per atom. As presented in Fig. 5, all the functionals predict that these configurations also have nearly

the same interlayer distance. When comparing the functionals, it is noted that GGA-PBE gives the highest interlayer spacing, whereas the vdW-DF2-C09_x yields the lowest.

When comparing configurations C₁₁-C₁₆, it is seen in Fig. 2 that C₁₁ is more energetically favorable whereas C₁₂ has the highest formation energies. We therefore suggest that configuration C₁₁ represents a possible template that can be used for hydrogen storage. The formation energies of configurations C₁₄-C₁₆ are between those for C₁₁ and C₁₂. This is due to the fact that they are made up of pair combinations of the conformers. The highest formation energy found for C₁₂ is in contrast with the findings of Leenaerts *et al.*⁶² for their studies of a similar kind of hydrogen arrangement on 2×1 single layer graphene. They found that a structure similar to configuration C₁₂ is lower in formation energy compared to that of C₁₃. In this work, we have examined similar configurations on 2×1 single layer graphene, and our results show the same trend as theirs⁶². When 2×1 bilayer graphene is considered, the trend alters. Interestingly, when the interlayer distance of configurations C₁₁-C₁₃ is fixed at 7 Å, analysis of the formation energies shows the same trend as the hydrogenated single layer graphenes (C₁₃>C₁₂>C₁₁). When the structures are allowed to relax to their equilibrium interlayer distance the trend changes to C₁₂>C₁₃>C₁₁, which tells us that there is a possible interaction between the hydrogen decorated planes that greatly affects the energetics of the structures.

The stability observed in C₁₁-C₁₆ is ascribed to the hydrogen induced puckering mechanism on both layers which was also observed by Sofo *et al.*⁵⁰ The relaxed structures show that all the carbon atoms are hydrogenated and the graphene layers are buckled (moved up and down out of the planes). Mainly, this buckling occurs during the wavefunction overlap between the carbon and hydrogen atoms resulting in all the carbon atoms having *sp*³ re-hybridization. It is noted in configurations C₁₁-C₁₃ that the hydrogen atoms are differently aligned after relaxation, and it is also shown in Table I that C₁₁ is uniformly distorted whereas C₁₂ and C₁₃ are non-uniformly distorted (see Fig. 4).

To quantify the distortions induced by hydrogen adatoms on the 2×1 supercell of bilayer graphene, the distances (l_a, l_s) and angles (θ_a, θ_s) between the carbon atoms are measured, and presented in Table III. Since l_s and θ_s are not measurable in C₁₁, this tells us that the structural properties deviate constantly for the entire structure unlike in C₁₂ and C₁₃. We see in C₁₂ that all the exchange correlation functionals predict that l_a stretches more than l_s , which is a confirmation that the hydrogen atoms are responsible for the non-uniform distortions in the structure. This observation is not always the case for all configurations because in C₁₃ the distance l_s is more than l_a . This implies that the different arrangements of hydrogen atoms result in different deviations in structural parameters, where we suspect the possible hydrogen-hydrogen interactions that lead to

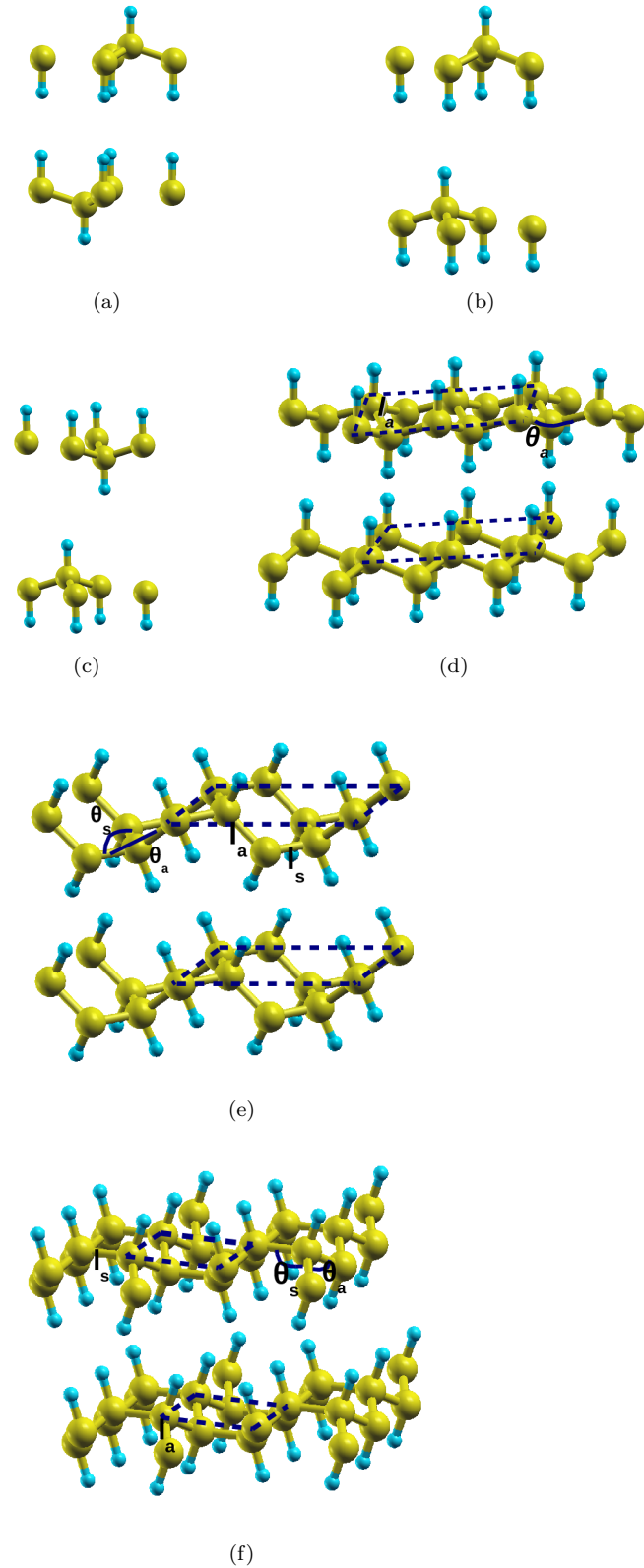


FIG. 4: The relaxed geometries of the three lowest energy competing configurations identified from a 1×1 unit cell: (a) C₇, (b) C₈, (c) C₉. Configurations (d) C₁₁, (e) C₁₂, and (f) C₁₃ are selected geometries that are only possible for a 2×1 supercell. The dashed parallelograms show the 2×1 supercell that contains four carbon atoms per plane. The distances l_s and l_a are the distinct distances between the carbon atoms with the hydrogen atoms adsorbed on the same side or in an alternating patterns, respectively. Similar for the angles.

TABLE III: The calculated structural properties of the selected configurations obtained from 2×1 supercell bilayer graphene using the five exchange correlation functionals. The distances l_s and l_a are the distinct distances between the carbon atoms where the hydrogen atoms are adsorbed on the same side or in an alternating patterns, respectively. Similar for the angles.

Functionals	C ₁₁		C ₁₂		C ₁₃		C ₁₁		C ₁₂		C ₁₃	
	l_a	l_s	l_a	l_s	l_a	l_s	θ_a	θ_s	θ_a	θ_s	θ_a	θ_s
GGA-PBE	1.53	1.59	1.54	1.52	1.52	1.57	110.8	117.3	106.9	109.4	112.5	112.5
vdW-DF	1.51	1.59	1.54	1.53	1.53	1.57	109.9	116.7	106.0	108.4	116.8	116.8
vdW-DF2	1.51	1.60	1.55	1.52	1.52	1.56	110.1	117.2	106.4	108.6	112.5	112.5
vdW-DF-C09 _x	1.51	1.58	1.55	1.52	1.52	1.56	110.1	117.5	106.2	108.8	112.65	112.65
vdW-DF2-C09 _x	1.51	1.58	1.54	1.52	1.52	1.55	110.1	117.5	106.6	108.6	112.9	112.9

bending of hydrogen atoms in C_{12} and C_{13} but not in C_{11} (see Fig. 4). It is important to note in Table III that each distance stretches towards a value that is close to that of cubic diamond value (1.53 \AA) and their corresponding angle deviates towards the ideal tetrahedral internal angle.

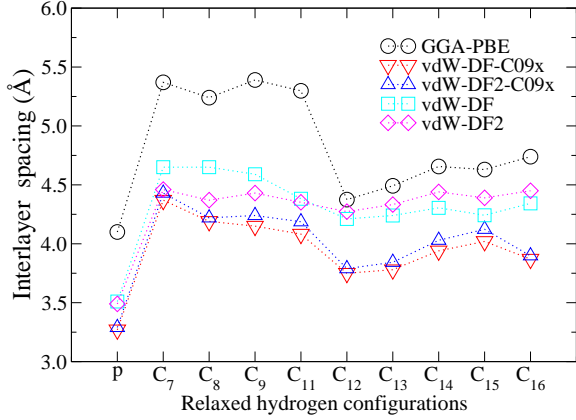


FIG. 5: The calculated equilibrium interlayer distances d_0 (in \AA) for the lowest energy competing configurations identified from 1×1 and 2×1 cells. The letter P stands for pristine bilayer graphene.

Even if it is known that in configurations C_{11} - C_{16} , all the carbon atoms are saturated resulting in the minimal π - π interactions between the hydrogen layers, it is seen on Fig. 5 that all the functionals vary in predicting the equilibrium interlayer distances (d_0). GGA-PBE gives the largest d_0 whereas vdW-DF-C09 $_x$ gives the lowest. It is also observed on Fig. 5 that the d_0 greatly depends on the arrangement of hydrogen adatoms. We see that configuration C_{12} , which is greatly distorted by the hydrogen atoms, has the shortest d_0 compared to the other configurations.

C. Elastic properties

We now look at the elastic properties of the most energetically favorable configuration C_9 . The values for the elastic constants and derived elastic moduli for all four functionals considered are given in Table. IV as well as those for graphene, bilayer graphene and graphane. Since these structures are all isotropic, they only have two independent elastic constants, namely c_{11} and c_{12} which can be calculated by separately applying an isotropic bi-axial strain and an area conserving strain.

From these the following elastic properties are defined

$$Y = c_{11} - \frac{c_{12}^2}{c_{11}}$$

$$G = c_{66} = \frac{c_{11} - c_{12}}{2} \quad (2)$$

$$\nu = \frac{c_{12}}{c_{11}}$$

where Y is the 2D Young's modulus (in-plane stiffness), G is the 2D shear modulus and ν is the Poisson ratio.

The results in Table. IV show that in the case of graphane and C_{11} , the elastic constants and modulus values increase from vdW-DF \rightarrow GGA-PBE \rightarrow vdW-DF2-C09 $_x$ \rightarrow vdW-DF-C09 $_x$. The Poisson ratios remain more or less constant for all four functionals. The results of Cadelano *et al.*⁶⁴ are comparable to our values for graphane and graphane with a slight discrepancy in c_{12} for graphane which results in a lower value of 0.08 for the Poisson ratio. The bilayered structures have values for the elastic constants and moduli which are approximately twice that of their monolayer counterparts. This is expected since the two layers are very weakly bound. The effect of hydrogenation is too reduce the elastic values of the pristine structures. For the elastic constants, c_{11} approximately reduces by a factor of 0.7 whereas c_{12} reduces by 0.40~0.43. This results in the moduli reducing by approximately 0.70~0.78. The effect of the added adatoms is to significantly reduce the strength of the pristine structures.

TABLE IV: Elastic properties for pristine and hydrogenated single and bi-layered graphene (Elastic constants c_{ij} , shear modulus G and in-plane stiffness Y in Nm^{-1} , Poisson ratio ν (dimensionless)).

		c_{11}	c_{12}	G	Y	ν
Graphene	GGA-PBE	354.4	62.1	146.2	343.5	0.175
	vdW-DF	346.0	58.2	143.9	336.2	0.168
	vdW-DF-C09x	355.7	64.9	145.4	343.8	0.182
	vdW-DF2-C09x	354.5	63.9	145.3	343.0	0.180
	GGA-PBE-PW91 ^a	354	60	147 ^b	344 ^b	0.17 ^b
bilayer graphene	GGA-PBE	708.3	126.0	291.2	685.9	0.178
	vdW-DF	690.5	117.1	286.7	670.6	0.170
	vdW-DF-C09x	707.1	134.2	286.5	681.6	0.190
	vdW-DF2-C09x	702.5	134.8	283.9	676.6	0.180
Graphane (100%)	GGA-PBE	245.4	25.0	110.2	242.9	0.102
	vdW-DF	236.4	23.0	106.7	234.2	0.097
	vdW-DF-C09x	251.4	27.8	111.8	248.3	0.111
	vdW-DF2-C09x	248.3	28.1	110.1	245.1	0.113
	GGA-PBE-PW91 ^a	248	20	114 ^b	246 ^b	0.08 ^b
C ₉	GGA-PBE	489.9	51.2	219.4	484.5	0.105
	vdW-DF	473.3	44.5	214.4	469.1	0.094
	vdW-DF-C09x	502.5	55.6	223.5	496.3	0.111
	vdW-DF2-C09x	497.0	55.1	221.0	490.9	0.111

^a Reference⁶⁴

^b Elastic properties derived from their elastic constants

D. Electronic properties of H configurations on bilayer graphene at 100% coverage

To examine the electronic nature of the identified configurations, electronic band dispersions are plotted along the selected high-symmetry points (M, K, Γ). As discussed earlier, the vdW-DF C09_x functional accurately predicts the correct interlayer separation and also gives the lowest formation energy as compared to other functionals. We therefore, discuss the band structures of selected configurations obtained using the vdW-DF C09_x functional. The calculated band gaps obtained from all five functionals are presented in Table V.

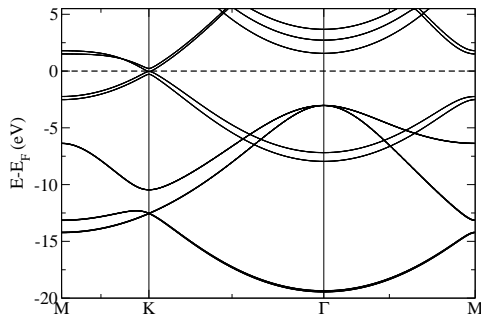


FIG. 6: The electronic band structures of pristine bilayer graphene. The Fermi level is marked by the dotted line.

In this discussion, the emphasis is on the K and Γ points since this is where the most drastic changes occur. Fig. 6 shows the band structure of pristine bilayer graphene. It is observed that there are double bands aligned towards the K point, appearing both on the valence and conduction bands. We also notice that the two bands from the valence band join the other two from the conduction band at the Fermi level (exactly at the K point), with a slight separation between the two bands in each pair. The reason for the split is attributed to electronic coupling from one layer to the other. Nevertheless pristine bilayer graphene is semimetallic in nature. Fig. 7(a) illustrates the band structure of configuration c_1 . Even though it is known that the physisorption of the H_2 dimer does not alter the physical properties of the system, it is observed that the four bands that nearly meet at K point in the pristine band structure are superimposed on top of each other in c_1 . Also, splitting of the bands is no longer visible as is seen in Fig. 6. This is attributed to the fact that the layers (plane A and plane B) in c_1 are no longer bonded by vdW forces. In contrast to configuration c_1 , the band structure of c_2 shows visible splitting of the bands at the vicinity of the K point (see Fig. 7(b)), which indicates that c_2 still retains the properties of the pristine bilayer structure. All the functionals predict that configurations c_1 and c_2 are zero band gap materials.

Simple electron counting reveals that c_3 , c_4 , c_5 and

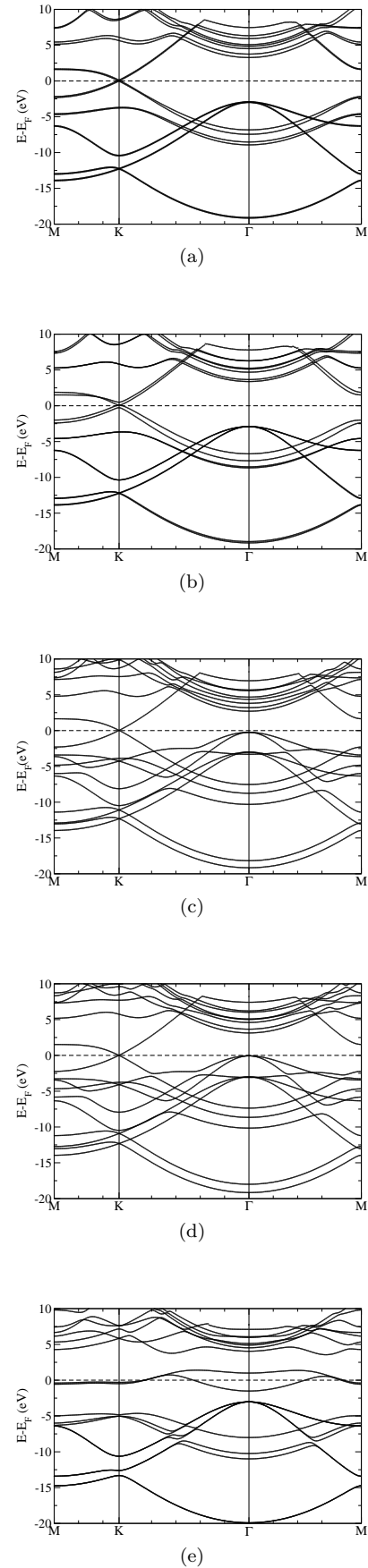


FIG. 7: The electronic band structures of: (a) c_1 , (b) c_2 , (c) c_3 , (d) c_5 and (e) c_{10} . The Fermi level is marked by the dotted line.

c_6 have similar electronic properties. We only show the band structures of c_3 and c_5 since they are the most energetically favourable ones of their group, as discussed earlier. Fig. 7(c) depicts that the band structure of c_3 has two linearly dispersed bands that meet at the K point, instead of the four bands seen in the pristine band structure. The disappearance of the other two bands in the band structure of c_3 is attributed to the fully saturated network of σ bonding occurring in plane A, and the wavefunction overlap between carbon and hydrogen orbitals. The remaining two linearly dispersed bands arise from the original π network structure that exists in Plane B. The same features also appear in the band structure of c_5 (see Fig. 7(d)). The band gap, measured at the Γ point, is reduced from 6.68 eV (GGA), 5.96 eV (vdW-DF), 6.07 eV (vdW-DF2), 6.02 eV (vdW-DF C09_x) and 6.19 eV (vdW-DF C09_x) in the pristine structure to 3.04 eV (GGA), 2.67 eV (vdW-DF), 2.90 eV (vdW-DF2), 2.83 eV (vdW-DF C09_x) and 2.77 eV (vdW-DF2 C09_x) in c_4 . This reduction might be caused by the additional bands from the atomic hydrogen. Nevertheless, configurations c_3 and c_5 are still semimetallic in nature. In the band structure of configuration c_{10} (see Fig. 7(e)), we observe the bands randomly crossing the Fermi level. This tells us that electrons are free to move from the valence to the conduction band. During hydrogenation, the original π -bond network breaks and the hydrogenated carbon atoms have σ -bonds; therefore the unhydrogenated carbon atoms have an excess of de-localized electrons which causes c_{10} to be metallic.

TABLE V: The calculated energy band gaps (in eV) of the lowest energy competing configurations and graphane. Five exchange-correlation functionals are used to illustrate the variations.

Functionals	C7	C8	C9	Graphane
vdW-DF C09 _x	2.99	3.00	3.08	3.04
vdW-DF2 C09 _x	2.87	2.94	2.94	3.04
vdW-DF	2.86	2.77	2.90	2.95
vdW-DF2	2.69	2.72	2.86	2.80
GGA-PBE	3.28	3.26	3.32	3.39

Fig. 8(a, b, c) illustrate the band structures of the three lowest energy competing configurations (c_7 , c_8 and c_9). These band structures exhibit sufficiently large band gaps of about 10 eV measured at the K point. It is clearly noted that the symmetries of the π bands on both layers (plane A and Plane B) have completely vanished, leaving all the carbon atoms in the sp^3 hybridized state (carbon atoms σ bonded with hydrogen atoms). It must be noted that in these configurations, the conduction band minimum (CBM) and valence band maximum (VBM) are

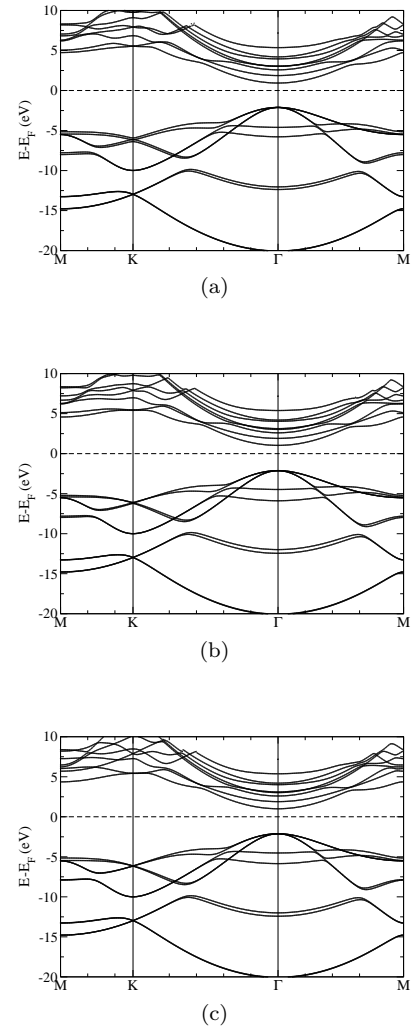


FIG. 8: The electronic band structures of: (a) c_7 , (b) c_8 and (c) c_9

separated by an energy band gap at the vicinity of the Γ point. The band structure of graphane also exhibits the same features. This result is not strange because graphane resembles each of the planes in configurations c_7 , c_8 and c_9 .

Table V indicates that the GGA functional gives large band gap values of 3.28 eV, 3.26 eV, 3.32 eV for c_7 , c_8 and c_9 , respectively. These values reveal that these configurations are wide band gap systems. The non-local functional vdW-DF C09_x predicts the largest band gaps as compared to the other three non-local variants, even though these values are still underestimated. In general, we suggest that in this respect, these implementations for vdW corrections still need to be improved.

IV. CONCLUSIONS

In this study, we investigated all hydrogen configurations that can possibly exist on a 1×1 unit cell of bilayer graphene at 100% coverage where each carbon contains an hydrogen adatom in the unrelaxed state. Thereafter the cell was increased to a 2×1 supercell to show other configurations that are not possible for a 1×1 unit cell. All the exchange correlation functionals predict that, of the ten identified configurations obtained from the 1×1 unit cell, nine are energetically favorable. The three lowest energy competing geometries (configurations C_7 - C_9) are identified. We notice that in the case of physisorbed H_2 dimer, the coupled structures are more energetically stable than the decoupled configurations.

In the case of a 2×1 supercell, only the six energetically favorable configurations are presented in this work. In these configurations, it is found that all hydrogen atoms are attached to the substrate after relaxation. In some of the configurations, it is found that the arrangement of hydrogen atoms greatly distort the hexagonal layer to such an extent, the $C - C$ bond distances are unequal. We notice that one of the identified configurations (C_{11}) exists both in 1×1 and 2×1 cells, and is the most energetically stable structure. We therefore suggest that this configuration represents a possible template that can be used for hydrogen storage.

Our results tells us that there is a possibility of interaction between the hydrogen decorated planes that greatly affects the energetics of the structures. The effect of the hydrogen adatoms greatly reduces the strength of the bilayer graphene structures. We found that the electronic properties greatly depend on the hydrogen configuration, whereby the three lowest energy competing structures are wide band gap systems.

In conclusion, it is seen that the functionals vary in predicting the various properties. The vdW-DF- $C09_x$ functional predicts the lowest formation energies and shortest interlayer distances for all configurations considered, whereas the GGA-PBE functional predicts highest formation energies and largest interlayer distances. In the case of the moduli results, vdW-DF gives the smallest values, whereas the vdW-DF- $C09_x$ gives the largest values.

ACKNOWLEDGMENTS

The authors would like to thank the University of Pretoria for computational resources and financial support. REM acknowledges the financial support from the National Research Foundation (NRF). NC and RCA are grateful to the National Institute of Theoretical Physics for financial support.

* edwin.mapasha@up.ac.za

† richard.andrew@up.ac.za

- ¹ M. Dion, H. Rydberg, E. Schroder, D. C. Langreth, and B. I. Lundqvist, Phys. Rev. Lett. **92**, 246401 (2004).
- ² O. A. von Lilienfeld, I. Tavernelli, U. Rothlisberger, D. Sebastiani, Phys. Rev. Lett. **93**, 153004 (2004).
- ³ J. Antony, and S. Grimme, Phys. Chem. Chem. Phys. **8**, 5287 (2006).
- ⁴ A. D. Becke, and E. R. Johnson, J. Chem. Phys. **127**, 154108 (2007).
- ⁵ S. Grimme, J. Antony, T. Schwabe, and C. Muck-Lichtenfeld, Org. Biomol. Chem. **5**, 741 (2007).
- ⁶ T. Sato, T. Tsuneda, and K. Hirao, J. Chem. Phys. **126**, 234114 (2007).
- ⁷ A. Tkatchenko and M. Scheffler, Phys. Rev. Lett. **102**, 073005 (2009).
- ⁸ Y. Zhang and W. Yang, Phys. Rev. Lett. **80**, 890 (1998).
- ⁹ G. Roman-Perez and J. M. Soler, Phys. Rev. Lett. **103**, 096102 (2009).
- ¹⁰ J. Klimes, D. R. Bowler, and A. Michaelides, J. Phys. Condens. Matter **22**, 022201 (2010).
- ¹¹ V. R. Cooper, Phys. Rev. B **81**, 161104 (2010).
- ¹² I. Hamada and M. Otani, Phys. Rev. B **82**, 153412 (2010).
- ¹³ K. Lee, E. D. Murray, L. Kong, B. I. Lundqvist, and D. C. Langreth, Phys. Rev. B **82**, 081101 (2010).
- ¹⁴ E. D. Murray, K. Lee, and D. C. Langreth, J. Chem. Theory Comput. **5**, 2754 (2009).
- ¹⁵ K. S. Novoselov, A. K. Geim, S. V. Morozov, D. Jiang, Y. Zhang, S. V. Dubonos, I. V. Grigorieva, and A. A. Firsov, Science **306**, 666 (2004).
- ¹⁶ A. K. Geim and K. S. Novoselov, Nature Mater. **6**, 183 (2007).
- ¹⁷ P. R. Wallace, Phys. Rev. **71**, 622 (1947).
- ¹⁸ K. S. Novoselov, A. K. Geim, S. V. Morozov, D. Jiang, Y. Zhang, M. I. Katsnelson, S. V. Dubonos, I. V. Grigorieva, and A. A. Firsov, Nature (London) **438**, 197 (2005).
- ¹⁹ K. S. Novoselov, Z. Jiang, Y. Zhang, S. V. Morozov, H. L. Stormer, U. Zeitler, J. C. Maan, G. S. Boebinger, P. Kim, and A. K. Geim, Science **315**, 1379 (2007).
- ²⁰ Y. Zhang, Y. W. Tan, H. L. Stormer, and P. Kim, Nature (London) **438**, 201 (2005).
- ²¹ A. H. Castro, F. Guinea, N. M. R. Peres, K. S. Novoselov, and A. K. Geim, Rev. Mod. Phys. **81**, 109 (2009).
- ²² F. Schedin, A. K. Geim, S. V. Morozov, E. W. Hill, P. Blake, M. I. Katsnelson, and K. S. Novoselov, Nature Mater. **6**, 652 (2007).
- ²³ W. Choi, I. Lahiri, R. Seelaboyina, and Y. S. Kang, Crit. Rev. Solid State and Mater. Sci. **35**, 52 (2010).
- ²⁴ H. Min and A. H. MacDonald, Phys. Rev. B **77**, 155416 (2008).
- ²⁵ T. Ohta, A. Bostwick, T. Seyller, K. Horn, and E. Rotenberg, Science **313**, 951 (2006).
- ²⁶ L. Sun, Q. X. Li, H. Ren, H. B. Su, Q. W. Shi, and J. L. Yang, J. Chem. Phys. **129**, 074074 (2008).
- ²⁷ Y. W. Son, M. L. Cohen, and S. G. Louie, Phys. Rev. Lett. **97**, 216803 (2006).
- ²⁸ M. Y. Han, B. Ozyilmaz, Y. Zhang, and P. Kim, Phys. Rev. Lett. **98**, 206805 (2007).
- ²⁹ F. Ding, Phys. Rev. B **72**, 245409 (2005).
- ³⁰ G. D. Lee, C. Z. Wang, E. Yoon, N. M. Hwang, D. Y. Kim,

- and K. M. Ho, Phys. Rev. Lett. **95**, 205501 (2005).
- ³¹ M. T. Lusk and L. D. Carr, Phys. Rev. Lett. **100**, 175503 (2008).
- ³² S. C Pradhan and J. K. Phadikar, Phys. Lett. A **373**, 1062 (2009).
- ³³ P. Lu, Z. Zhang, and W. Guo, Phys. Lett. **373**, 3354 (2009).
- ³⁴ Z. Q. Luo, T. Yu, K. J. Kim, Z. H. Ni, Y. M. You, S. H. Lim, Z. X. Shen, S. Z. Wang, and J. Y. Lin, ACSNANO **3**, 1781 (2009).
- ³⁵ Y. H. Lu, W. Chen, Y. P. Feng, and P. M. He, J. Phys. Chem. B **113**, 2 (2009).
- ³⁶ I. Zanella, S. Guerini, S. B. Fagan, J. MendesFilho, and A. G. SouzaFilho, Phys. Rev. B **77**, 073404 (2008).
- ³⁷ R. M. Ribeiro, N. M. R. Peres, J. Coutinho, and P. R. Briddon, Phys. Rev. B **78**, 075442 (2008).
- ³⁸ D. W. Boukhvalov, M. I. Katsnelson, and A. I. Lichtenstein, Phys. Rev. B **77**, 035427 (2008).
- ³⁹ S. Lebegue, M. Klintonberg, O. Eriksson, and M. I. Katsnelson, Phys. Rev. B **79**, 245117 (2009).
- ⁴⁰ E. J. Duplock, M. Scheffler, and P. J. D. Lindan, Phys. Rev. Lett. **92**, 225502 (2004).
- ⁴¹ D. W. Boukhvalov and M. I. Katsnelson, Phys. Rev. B **78**, 085413 (2008).
- ⁴² N. Z. Lu, Z. Y. Li, and J. L. Yang, J. Phys. Chem. C **113**, 16741 (2009).
- ⁴³ J. A. Yan, L. Xian, and M. Y. Chou, Phys. Rev. Lett. **103**, 086802 (2009).
- ⁴⁴ X. S. Wu, M. Sprinkle, X. B. Li, F. Ming, C. Berger, and W. A. de Heer, Phys. Rev. Lett. **101**, 026801 (2008).
- ⁴⁵ I. Jung, D. A. Dikin, R. D. Piner, and R. S. Ruoff, Nano Lett. **8**, 4283 (2008).
- ⁴⁶ Z. Luo, P. M. Vora, E. J. Mele, A. T. C. Johnson, and J. M. Kikkawa, Appl. Phys. Lett. **94**, 111909 (2009).
- ⁴⁷ R. Balog, B. Jorgensen, L. Nilsson, M. Andersen, E. Rienks, M. Bianchi, M. Fanetti, E. Laegsgaard, A. Baraldi, S. Lizzit, Z. Sljivancanin, F. Besenbacher, B. Hammer, T. G. Pedersen, P. Hofmann, and L. Hornekaer. Nature Mater. **9**, 315 (2010).
- ⁴⁸ A. Savchenko, Science **323**, 589 (2009).
- ⁴⁹ D. C. Elias, R. R. Nair, T. M. G. Mohiuddin, S. V. Morozov, P. Blake, M. P. Halsall, A. C. Ferrari, D. W. Boukhvalov, M. I. Katsnelson, A. K. Geim, and K. S. Novoselov, Science. **323**, 610 (2009).
- ⁵⁰ J. O. Sofo, A. S. Chaudhari, and G. D. Barber, Phys. Rev. B **75**, 153401 (2007).
- ⁵¹ K. S. Subrahmanyam, P. Kumar, U. Maitra, A. Govindaraj, K. P. Hembram, U. V. Waghmare, and C. N. R. Rao, Proc. Nat. Acad. Sci. (USA) **108**, 2677 (2011).
- ⁵² M. Jaiswal, C. H. Lim, Q. Bao, C. T. Toh, K. P. LOh, and B. Ozyilmaz, ACSNANO **5**, 888 (2011).
- ⁵³ L. Wang, N. R. Stuckert, and R. T. Yang, AIChE, **57**, 10 (2011).
- ⁵⁴ O. Leenaerts, B. Partoens, and F.M. Peeters, Phys. Rev. B **80**, 245422 (2009).
- ⁵⁵ R. E. Mapasha, A.M. Ukpong, and N. Chetty, Phys. Rev. B **85**, 205402 (2012).
- ⁵⁶ J. Rohrer, and P. Hyltdgaard, Phys. Rev. B **83**, 165423 (2011).
- ⁵⁷ P. E. Blochl, Phys. Rev. B **50**, 17953 (1994).
- ⁵⁸ P. Giannozzi, S. Baroni, N. Bonini, M. Calandra, R. Car, C. Cavazzoni, D. Ceresoli, G. L. Chiarotti, M. Cococcioni, I. Dabo, A. Dal Corso, S. Fabris, G. Gougoussis, A. Kokalj, M. Lazzeri, L. Martin-Samos, N. Marzari, F. Mauri, R. Mazzarello, S. Paolini, A. Pasquarello, L. Paulatto, C. Sbraccia, S. Scandolo, G. Sclauzero, A. P. Seitsonen, A. Smogunov, P. Umari, and R. M. Wentzcovitch, J. Phys. Condens. Matter **21**, 395502 (2009).
- ⁵⁹ J. P. Perdew, K. Burke, and M. Ernzerhof, Phys. Rev. Lett. **77**, 3865 (1996).
- ⁶⁰ H. J. Monkhorst and J. D. Pack, Phys. Rev. B **13**, 5188 (1976).
- ⁶¹ See Table SIV in the supplementary material of¹². Available online at: <http://link.aps.org/supplemental/10.1103/PhysRevB.82.153412>
- ⁶² O. Leenaerts, H. Peelaers, A. D. Hernandez-Nieves, B. Partoens, F. M. Peeters, Phys. Rev. B **82**, 195436 (2010)
- ⁶³ D. Henwood and J. D. Carey, Phys. Rev **75**, 245413 (2007).
- ⁶⁴ E. Cadelano, P. L. Palla, S. Giordano and L. Colombo, Phys. Rev. B. **82**, 235414 (2010).

Chapter 6

Comparative investigations of lithium adatoms on AA and AB stackings of bilayer graphene : a van der Waals density functional study

The work presented in this chapter has been accepted for publication: R. E. Mapasha and N. Chetty, Computational and theoretical nanoscience.

In this chapter, we use the newly developed exchange-correlation functionals to investigate the effects of lithium (Li) on bilayer graphene. Since it is known that Li prefers to be sandwiched between the layers, it is important to examine how the interlayer separation changes, using these functionals that do not neglect the effects of van der Waals forces. Detailed information for this study is given in the attached publication. This publication outlines the computational details used and the results

that were obtained together with the conclusions that were drawn from the study.

Comparative investigations of lithium adatoms on AA and AB stackings of bilayer graphene : a van der Waals density functional study

R. E. Mapasha*

Department of Physics, University of Pretoria, Pretoria 0002, South Africa

N. Chetty¹,

National Institute for Theoretical Physics, Johannesburg, 2000, South Africa

(Dated: September 2, 2013)

We have systematically investigated the effects of lithium (Li) on AA and AB stacking sequences of bilayer graphene using density functional theory (DFT). To accurately describe the bonding that occurs in bilayer graphene, the following van der Waals corrected exchange correlation functionals were used, namely, vdW-DF revPBE, vdW-DF C09_x and vdW-DF2 C09_x. Several configurations that contain two Li atoms were considered to examine the effects of the Li-Li interaction on bilayer graphene. For all configurations considered, we observe a variation in formation energies predicted by these functionals. The vdW-DF revPBE consistently predicts the highest formation energies, and vdW-DF2 C09_x gives the lowest. One of the Li-configurations ($c_{10(AB)}$) undergoes a spontaneous translation from the AB to AA stacking, and is found to be the most energetically stable configuration compared to the other configurations. It is found that the change in the interlayer distance caused by Li intercalation greatly depends on the exchange correlation functional used. The GGA-PBE shows a reduction in the interlayer distance while the van der Waals corrected exchange correlation functionals show an expansion. In the case of Li intercalated configurations, GGA gives nearly the same interlayer distances as vdW-DF revPBE, unlike in the pristine structures. The agreement of these two functionals is explicitly discussed. Even if the construction of these van der Waals corrected exchange correlation functionals was based on the energetics (stability) and structural properties, our calculated workfunction for pristine bilayer graphene obtained using, i.e. vdW-DF2 C09_x agrees very well with the experimental data compared to GGA-PBE.

I. INTRODUCTION

The isolation of free standing graphene from graphite was first performed by Novoselov *et al.*¹ in 2004. Graphene has attracted a lot of interest because of its fascinating properties, which include its charge carriers that behave as massless Dirac fermions at the corner of the Brillouin zone, the observed anomalous quantum Hall effect, ballistic transport at room temperature, the relatively high thermal conductivity and high specific surface area.²⁻⁸ The latter property gives graphene the potential of being used in a rechargeable lithium ion battery (LIB), enabling the LIB to charge and discharge within a small volume.⁹⁻¹¹ For the past years, LIB have been used in portable electronic devices applying graphite as the anode material.¹²⁻¹⁶ Graphite has more advantages than plane metallic Li which was previously used. One example is for safety reasons since metallic Li is highly reactive while graphite is not.¹⁷ Moreover, graphite is commercially more easily available.¹⁸

The performance of graphite as an anode has however become limited. For instance it is not capable of being used in electric vehicles because of its low Li storage capacity.¹⁹ Graphite has a Li storage capacity of about 372 mAhg^{-1} .²⁰ Recent studies have shown that single and few layered graphene structures have larger Li storage capacities compared to graphite, and therefore can overcome the shortcomings of graphite in the context of energy storage.^{19,21-23} Few layered graphene structures refer to bilayer and trilayer graphene systems which have

more advantages compared to single layer graphene because of the possibility of sandwiching the Li atoms between the layers. This makes the processes of charging and discharging in the LIB more easily controlled by the intercalation and de-intercalation mechanism of Li ions between the layers. Several authors have made a good contribution in understanding the various properties of these pristine layered systems before the defects can be included.^{6-8,24,25} Theoretical²⁶⁻²⁹ and experimental³⁰⁻³² studies have been performed on Li intercalated few layered graphene. Results obtained thus far give an insight into how Li affects the electronic, structural, and other properties including the intrinsic strength. It was found that Li donates an electron to graphite through ionic charge transfer. The transferred electron fills the empty carbon orbitals, resulting in a shift of Fermi level into the conduction band. This, in turn, transforms the structure from semimetallic to metallic. The same behaviour was also revealed in recent studies of Li adsorption on single layer graphene.³³⁻³⁶

Recently, Sugawara *et al.*³⁰ probed the Li intercalated bilayer graphene experimentally. Using low-energy electron diffraction (LEED), it was found that the effects of Li atoms between the layers increase the interlayer distance as compared to the pristine structure.³⁰ Their³⁰ angle-resolved photo emission spectroscopy (ARPES) measurements revealed that the Li atoms that are intercalated between the layers are fully ionized. Furthermore, the ARPES spectra indicated that the Dirac point shifted from the Fermi level into the valence bands

by 1.4 eV. Watcharinyanon *et al.*³¹ conducted experimental studies of intercalated Li in hydrogenated bilayer graphene. Low energy electron microscopy indicated that the deposited Li atoms form islands of defects which disappear during annealing. It was found that the workfunction of the sample decreases after deposition of Li ions. Similar to the observation of Sugawara *et al.*³⁰, Watcharinyanon *et al.*³¹ conducted the ARPES measurements on the Li deposited sample and found that the Dirac point also shifted from the Fermi level to the valence bands by 1.25 eV. Virojanadara *et al.*³² used low-energy electron microscopy (LEEM), photo electron spectroscopy, angle-resolved photo emission spectroscopy (ARPES) and micro-low-energy electron diffraction (μ -LEED) to probe the influence of Li deposition on monolayer graphene grown on a silicon-terminated SiC (0001) surface. They noted the occurrence of a carbon interface (buffer) layer between the graphene and induced bulk SiC. Their results showed that the Li penetrates through the graphene and carbon buffer layer. The LEEM measurements deduced that the workfunction of the sample was reduced after Li deposition. Their angle-resolved photo emission spectroscopy (ARPES) measurements also confirmed the Li intercalation by showing the lowering of the Dirac point from the Fermi level.³²

Denis²⁸ examined the chemical reactivity of Li doped monolayer and bilayer graphene using density functional methods. For the description of the exchange correlation interaction, GGA-PBE and LDA functionals were used in the Li adsorbed single layer graphene and bilayer graphene, respectively. The LDA functional was employed ostensibly to take into account the effect of the van der Waals forces. It was found that these Li doped structures are metallic in nature. It was revealed that the metallic character of Li-adsorbed single layer graphene can be easily affected by the attachment of radicals (OH, CH₃, H, etc) resulting in an observable band gap, but in Li-doped bilayer graphene, the metallicity is always retained after the attachment of radicals. Zhou *et al.*²⁷ employed the LDA functional to probe the Li intercalated AA and AB stacking bilayer graphene. They found that for each Li concentration, the Li intercalated AA stacking is lower in total energy compared to Li intercalated AB stacking. Interestingly, for the intercalation of one Li atom, both stackings have the same interlayer spacing but differ when the Li concentration increases. They also revealed that due to an increase in the Li concentration, the AB stacking translates to AA stacking. Kaloni *et al.*²⁹ conducted a DFT study of the intrinsic charge carrier densities in Li intercalated bulk graphite, bilayer and trilayer graphene using the GGA functional. Firstly, it was observed that for all systems under study, Li induces a metallic character and enhances the intrinsic charge carrier densities. They also deduced that Li-intercalated bilayer graphene has higher charge carrier densities than Li intercalated bulk graphite and trilayer graphene.

Kganyago²⁶ and Imai³⁷ considered standard DFT functionals (GGA and LDA) in their description of lithi-

ated graphitic structures. There is, therefore, a need to apply more accurate functionals in the study of these systems. Lately, various theoretically developed methods can adequately describe a wide range of systems including these graphitic related materials.³⁸⁻⁴⁴ In our paper, we systematically investigate the effects of lithium (Li) on AA and AB stacking sequences of bilayer graphene. To accurately describe the bonding that occurs in bilayer graphene, the following van der Waals corrected exchange correlation functionals were used, namely, vdW-DF revPBE⁴⁵, vdW-DF C09_x⁴⁶ and vdW-DF2 C09_x^{46,47} and we compare our results with GGA-PBE.⁴⁸ In the next section we present our computational methodology, and in Section III we give the details of the various configurations that we considered together with a discussion of our results. We provide a brief set of conclusions in Section IV.

II. COMPUTATIONAL DETAILS

Our *ab initio* calculations were performed using the plane wave self-consistent field (PWSCF) code included in the Quantum ESPRESSO package.⁴⁹ For the description of the exchange-correlation interaction, our calculations were done using the following functionals: generalized gradient approximation parameterization of Perdew, Burke and Ernzerhof (GGA-PBE)⁴⁸, the non-local van der Waals density functional (vdW-DF revPBE)⁴⁵ and the recently improved non-local van der Waals density functionals employing the Cooper exchange functional (vdW-DF C09_x and vdW-DF2 C09_x)^{46,47}. These functionals were implemented using the efficient algorithm developed by Roman-Perez and Soler.⁵⁰ For the electronic core interaction, the projector augmented wave (PAW) pseudopotentials were used.⁵¹

The converged kinetic energy cutoff was set at 500 eV for the plane wave expansion of the wavefunctions. For the sampling of the Brillouin zone using the Monkhorst-Pack scheme, convergence was tested for total energy differences and we concluded that the grid size of 10x10x1 is sufficient.⁵² The conjugate gradient method was used for the atomic relaxation until the forces on the ions were less than 0.002 eV/Å. The energy convergence threshold was set at an accuracy of 10⁻⁷ eV for self-consistency. In order to be able to study many different Li configurations, a (2x2) supercell of bilayer graphene was constructed with a vacuum spacing of 30 Å to avoid spurious interlayer interactions between the periodic graphene images.

III. RESULTS AND DISCUSSION

A. Identification of Li configurations with AB and AA stacked bilayer graphene

Fig. 1 depicts the AA (simple) and AB (Bernal) stacking sequences that are used to identify all the possi-

ble Li configurations on the (2x2) bilayer graphene supercell which are listed in Table I. Comparing these stackings, our results show that AA stacking is 0.02 eV/atom (GGA), 0.04 eV/atom (vdW-DF revPBE), 0.13 eV/atom (vdW-DF C09_x) and 0.12 eV/atom (vdW-DF C092_x) higher in total energy compared than AB stacking. These results are in agreement with previous findings.^{53,54} Experimental investigations reveal that bilayer graphene is realisable in both stacking sequences.⁵⁵⁻⁵⁷ In contrast to pristine structures, it was previously found that the Li intercalated AA stacking is energetically more favourable than Li-AB stacking.²⁷ In this work, the systematic study of the adsorption of Li atoms on both stacking sequences is conducted to compare the energies and structural properties of all the Li configurations, using different exchange correlation functionals, and in so doing we also investigate the competing low energy configurations.

There is already abundant, extensive experimental and theoretical evidence that suggests that Li prefers to be adsorbed above the hollow (centre of hexagon) site rather than above the carbon or bridge sites in single layer, bilayer and few-layers graphene.

Our results for bilayer graphene demonstrate that the adsorption of a Li atom above the hollow site is 0.27 eV/atom (GGA-PBE), 0.19 eV/atom (vdW-DF revPBE), 0.27 eV/atom (vdW-DF C091_x) and 0.26 eV/atom (vdW-DF C092_x) lower in energy compared to above the carbon atom site. Also, we found that the hollow site is 0.21 eV/atom (GGA-PBE), 0.15 eV/atom (vdW-DF revPBE), 0.20 eV/atom (vdW-DF C091_x) and 0.23 eV/atom (vdW-DF C092_x) lower in energy compared to above the bridge site.

For all these identified Li configurations, the Li atoms were placed at an optimal distance of 1.80 Å above the identified site outside the bilayer in the unrelaxed state before determining the fully self consistent, relaxed final state. We considered all the ordered structures of Li atoms (α) on bilayer graphene (β), namely $\alpha\beta\beta$, $\beta\alpha\beta$, $\alpha\alpha\beta\beta$, $\alpha\beta\alpha\beta$, $\alpha\beta\beta\alpha$, and $\beta\alpha\alpha\beta$. The positions labelled 1, 2, 3, 4, (top layer) and 1', 2', 3', and 4' (bottom layer) in Fig. 1 identify each hollow site present in the (2x2) supercell, and are used to label distinct configurations in Table I. The labels *a* and *b* denote whether the Li atom is above or below the layer, respectively. For instance, configuration c_1 is named 1_a which denotes that the Li atom is adsorbed above hollow site number one.

In the case of single Li atom adsorption, only two unique configurations are possible (see Table I). Two Li atoms are considered to study all the Li ordered structures in (2x2) bilayer graphene and to examine the effect of Li-Li interactions in this system. In order to avoid double counting when identifying the Li configurations, the periodicity of the lattice is taken into consideration. For instance configuration 1_a2_a is periodically equivalent to 1_a4_a and 2_a3_a , and therefore we only present configu-

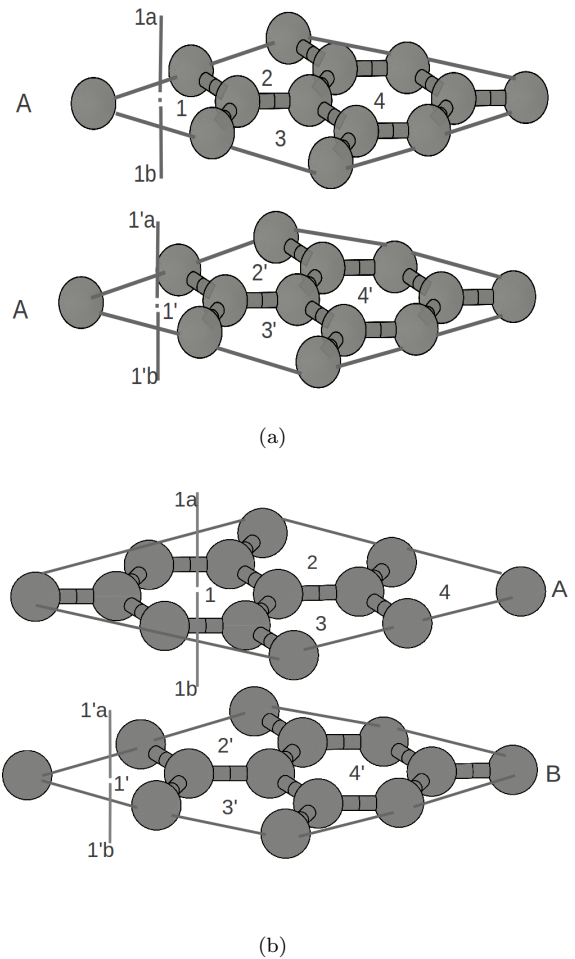


FIG. 1. Li adsorption sites for (a) AA and (b) AB stacking sequences (2x2) supercell of bilayer graphene in the unrelaxed states. The symbols 1_a and 1_b depict the adsorbed Li above and below the hollow site, respectively.

ration 1_a2_a in Table I. It must be mentioned that in some cases, a single ordered structure can contain several different configurations, i.e. configurations $1_a1'_b$ and $1_a2'_b$ have the same Li ordered structure $\alpha\beta\beta\alpha$.

A total of 12 unique configurations for AB and 9 for AA stackings were identified. We observed that some configurations are energetically equivalent after relaxation in spite of the uniqueness of their initial unrelaxed states. One Li configuration ($c_{10(AB)}$) undergoes spontaneous translation from AB to AA stacking. This configuration has the Li ordered structure $\beta\alpha\alpha\beta$. Configuration $c_{9(AA)}$ has the ordered structure $\beta\alpha\alpha\beta$ but is not energetically equivalent to $c_{10(AB)}$. This is because the vertically arranged Li atoms in $c_{9(AA)}$ break the symmetry of the bilayer by moving the layers far apart from each other, while in $c_{10(AB)}$ the horizontally arranged Li atoms slide one layer over another, translating the structure from AB to AA stacking. The energetics of these configurations are discussed in more detail in the next

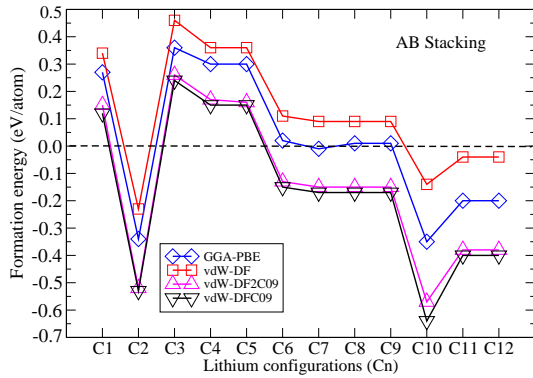
TABLE I. The identified Li configurations obtained from AA and AB stacking sequences in a (2×2) supercell that contains eight carbon atoms per layer. The Li ordered structure gives an indication of how the Li adsorbed geometries are arranged. The letters α , β denote the Li atom and graphene layer, respectively

Index	AB stacking		AA stacking		Li ordered structure	Ratio of adsorption	% Coverage
	Configuration	Index	Configuration	Index			
$C_1(AB)$	1_a	$C_1(AA)$	1_a	$C_1(AA)$	$\alpha\beta\beta$	1/16	6.25
$C_2(AB)$	1_b	$C_2(AA)$	1_b	$C_2(AA)$	$\beta\alpha\beta$	1/16	6.25
$C_3(AB)$	$1_a 2_a$	$C_3(AA)$	$1_a 2_a$	$C_3(AA)$	$\alpha\alpha\beta\beta$	2/16	12.50
$C_4(AB)$	$1_a 1'_b$	$C_4(AA)$	$1_a 1'_b$	$C_4(AA)$	$\alpha\beta\beta\alpha$	2/16	12.50
$C_5(AB)$	$1_a 2'_b$	$C_5(AA)$	$1_a 2'_b$	$C_5(AA)$	$\alpha\beta\beta\alpha$	2/16	12.50
$C_6(AB)$	$1_a 1_b$	$C_6(AA)$	$1_a 1_b$	$C_6(AA)$	$\alpha\beta\alpha\beta$	2/16	12.50
$C_7(AB)$	$1_a 2_b$	$C_7(AA)$	$1_a 2_b$	$C_7(AA)$	$\alpha\beta\alpha\beta$	2/16	12.50
$C_8(AB)$	$1_a 2'_a$				$\alpha\beta\alpha\beta$	2/16	12.50
$C_9(AB)$	$1_a 1'_a$				$\alpha\beta\alpha\beta$	2/16	12.50
$C_{10}(AB)$	$1_b 2_b$	$C_8(AA)$	$1_b 2_b$	$C_8(AA)$	$\beta\alpha\alpha\beta$	2/16	12.50
$C_{11}(AB)$	$1_b 2'_a$	$C_9(AA)$	$1_b 1'_a$	$C_9(AA)$	$\beta\alpha\alpha\beta$	2/16	12.50
$C_{12}(AB)$	$1_b 1'_a$				$\beta\alpha\alpha\beta$	2/16	12.50

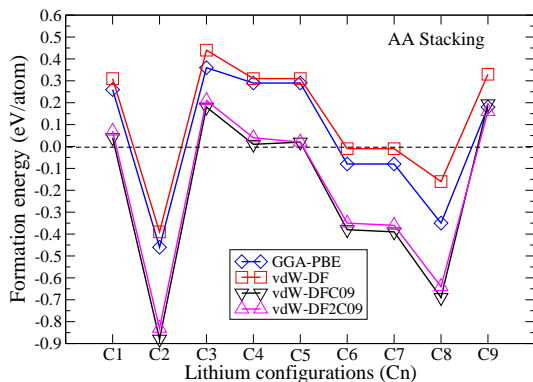
subsection.

B. Stability analysis and structural properties

We present our calculated formation energies for the various Li configurations in Fig. 2 for both stackings. The formation energy is defined as the energy per Li atom of the lithiated bilayer graphene with respect to pristine graphene and metallic Li in the BCC structure. In all configurations, we observe a variation of the functionals in predicting the formation energies, showing a decreasing trend from vdW-DF revPBE \rightarrow GGA-PBE \rightarrow vdW-DF C09_x \rightarrow vdW-DF2 C09_x. Even if it is expected that the usage of van der Waals corrected functionals, more especially vdW-DF revPBE, should stabilize the structure, it is noted in this work that the effect of the ionic origin induced by Li alters the situation.



(a)



(b)

FIG. 2. The variation in formation energies for different Li configurations obtained from (a) *AB* and (b) *AA* stacking sequences.

This unexpected observed largest formation energy in

vdW-DF revPBE, is mainly because the revPBE exchange is too repulsive to describe these Li induced ionic systems. It is interesting to note in Fig. 2 that for lithiated bilayer graphene, GGA-PBE gives comparable results to the other functionals, unlike in the case of the pristine structure.

We first compared the formation energies of configurations c_1 and c_2 , since both contain one Li atom. All the functionals give negative formation energies for c_2 and positive values for c_1 in both the *AA* and *AB* stackings. Imai *et al.*³⁷ studied similar structures and found that when the Li atom is adsorbed on unit cells that contain two carbon atoms per layer, the structures have positive formation energies but when the number of carbon atoms increases the formation energies drop to negative values. Our results obtained using (2x2) supercells that contain eight carbon atoms per layer reveal that the Li atom prefers to be sandwiched between the layers (see Fig. 3). When comparing the effect of Li on the two stackings, Fig. 2 shows that configuration $c_{1(AA)}$ is lower in energy than $c_{1(AB)}$, and that $c_{2(AA)}$ is more favourable than $c_{2(AB)}$. It is clear that Li prefers *AA* stacked bilayer graphene regardless of its position. The fact that $c_{2(AA)}$ is more energetically stable than $c_{2(AB)}$ is due to the Li atom preferring to be adsorbed over the hollow site. Fig. 3 shows that in configuration $c_{2(AA)}$, the Li atom faces two hollow sites whereas in $c_{2(AB)}$ the Li atom faces a hollow above and an on-top site below.

We further investigated the stability of all the configurations that contain two Li atoms on (2x2) bilayer graphene to examine the effects of the Li-Li interaction. Considering *AB* stacking, configurations $c_{3(AB)}$, $c_{4(AB)}$ and $c_{5(AB)}$ have higher (positive) formation energies compared to $c_{6(AB)}$ to $c_{12(AB)}$. For *AA* stacking we see that $c_{3(AA)}$, $c_{4(AA)}$, and $c_{5(AA)}$ have higher formation energies compared to $c_{6(AA)}$, $c_{7(AA)}$ and $c_{8(AA)}$. We therefore conclude that it is energetically less favourable to create configurations $c_{3(AB)}$, $c_{4(AB)}$, $c_{5(AB)}$, $c_{3(AA)}$, $c_{4(AA)}$ and $c_{5(AA)}$ that fall under the ordered structure $\alpha\alpha\beta\beta$ and $\alpha\beta\beta\alpha$. It is seen in Table I that in all these configurations, the Li atoms are attached outside the bilayer. In both stackings, Fig. 2 shows that c_3 is the least energetically stable structure compared to all others. This structure contains covalently bonded Li atoms adsorbed on the same side of the layer as shown in Fig. 3. The observed instability of c_3 is rather surprising because

it is expected that the ionic charge distribution between the Li atoms and the substrate could result in the spontaneous formation of this dimer structure. It is seen in Fig. 2 that the formation energies for configurations $c_{4(AB)}$, $c_{5(AB)}$, $c_{4(AA)}$ and $c_{5(AA)}$ are almost equal to those for c_1 in both stackings. In these configurations, one Li atom is placed above the top layer while the second Li atom is below the bottom layer. Therefore this finding should not be unexpected since the Li-Li interaction is considered to be minimal.

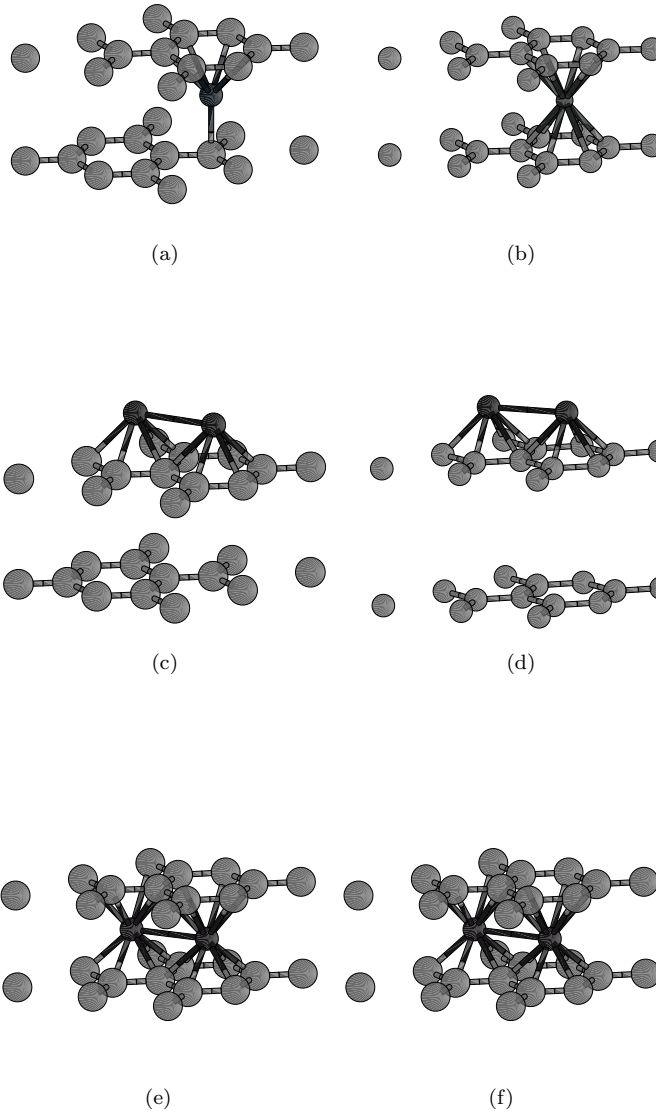


FIG. 3. The selected relaxed geometries showing the Li atoms adsorbed either outside or within the bilayer graphene: the intercalation of single Li atom in (a) AB stacking $c_{2(AB)}$ and (b) AA stacking $c_{2(AA)}$, the adsorbed Li dimer outside the (c) AB stacking $c_{3(AB)}$ and (d) AA stacking $c_{3(AA)}$, and the intercalation of Li dimer in; (e) AB stacking $c_{10(AB)}$ and (f) AA stacking $c_{8(AA)}$. Note that $c_{10(AB)}$ translate to $c_{8(AA)}$ during relaxation.

Configurations $c_{6(AB)}$, $c_{7(AB)}$, $c_{8(AB)}$, $c_{9(AB)}$, $c_{6(AA)}$ and $c_{7(AA)}$ have one Li atom adsorbed on the outside of the top layer while the other is intercalated, and therefore fall under the ordered structure $\alpha\beta\alpha\beta$ (see Table I). Apart from vdW-DF revPBE, Fig. 2 shows that all the other functionals give negative formation energies for these configurations. We suggest that the spontaneous formation of these configurations arises from the effect of the intercalated Li atom, since the nature of bonding

within the bilayer graphene is no longer van der Waals but Li-induced ionic. Therefore, these configurations are energetically stabilized by this complete change of bonding, unlike in configurations $c_{4(AB)}$, $c_{5(AB)}$, $c_{4(AA)}$ and $c_{5(AA)}$ where the bonding outside is ionic while on the inside is the weak, distorted van der Waals interaction. Fig. 2 shows that the formation energies for configurations $c_{6(AB)}$, $c_{7(AB)}$, $c_{8(AB)}$ and $c_{9(AB)}$ are the same irrespective of the arrangement of Li atoms in the intercalated region. These configurations have not been experimentally investigated but our results show that they are energetically realisable.

Fig. 2 depicts that all the functionals give negative formation energies for configurations $c_{10(AB)}$, $c_{11(AB)}$, $c_{12(AB)}$ and $c_{8(AA)}$, indicating that they are more energetically favourable compared to configurations $c_{6(AB)}$, $c_{7(AB)}$, $c_{8(AB)}$, $c_{9(AB)}$, $c_{6(AA)}$ and $c_{7(AA)}$. It is shown in Table I that all the Li atoms are intercalated in configurations $c_{10(AB)}$, $c_{11(AB)}$, $c_{12(AB)}$ and $c_{8(AA)}$, but not in configurations $c_{6(AB)}$, $c_{7(AB)}$, $c_{8(AB)}$, $c_{9(AB)}$, $c_{6(AA)}$ and $c_{7(AA)}$. It is obvious that the low formation energies for configurations $c_{10(AB)}$, $c_{11(AB)}$, $c_{12(AB)}$ and $c_{8(AA)}$, arise from the effects of the two intercalated Li atoms. The intercalated Li atoms break the symmetry of the AB stacking only in configuration $c_{10(AB)}$, which in turn induces AA stacking after relaxation. This translation makes $c_{10(AB)}$ structurally equivalent to $c_{8(AA)}$, with both having the same formation energy, and where the two intercalated Li atoms are covalently bonded to each other as shown in Fig. 3.

In configurations $c_{11(AB)}$ and $c_{12(AB)}$, we see that the symmetry of the AB stacking is still preserved after relaxation, which reveals that the $AB \rightarrow AA$ translation critically depends on the position of the Li atoms within the bilayer graphene. The high formation energy observed for configuration $c_{9(AA)}$ shows that the intercalated Li atoms do not prefer to be vertically arranged between the layers. This kind of arrangement breaks the symmetry of bilayer graphene, resulting in a large interlayer distance which implies that the layers are decoupled and no longer equivalent to coupled bilayer graphene.

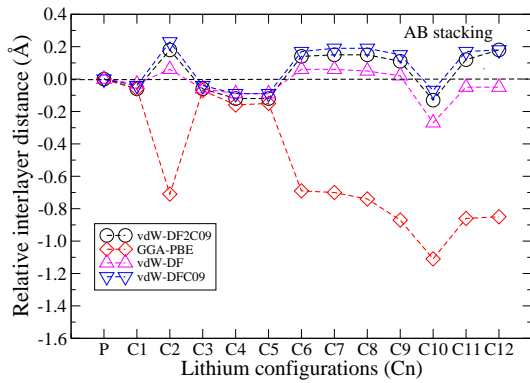
Next we investigate the effect of Li on the interlayer spacing of bilayer graphene. Table II summarizes the interlayer distances for pristine and lithiated bilayer graphene obtained using the different exchange correlation functionals. In the case of pristine bilayer graphene, the functionals vary in predicting the interlayer distance with decreasing order from GGA-PBE \rightarrow vdW-DF revPBE \rightarrow vdW-DF2 C09_x \rightarrow vdW-DF C09_x. This observation is in agreement with previous studies.^{54,58} The results for the functionals vdW-DF C09_x and vdW-DF2 C09_x show an underestimation compared with the experimental value⁵⁹ of 3.40 Å, whereas GGA-PBE and vdW-DF revPBE show an overestimation. We found that the interlayer distances given by the two functionals vdW-DF C09_x and vdW-DF2 C09_x are within 3% of the experimental value.

Fig. 4 presents the variation of the relative interlayer

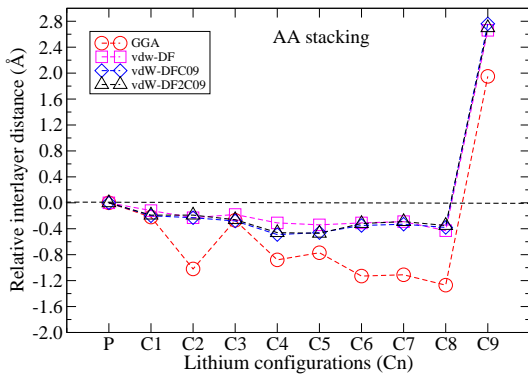
TABLE II. The calculated equilibrium interlayer distance (in Å) for pristine and Li configurations identified from *AA* and *AB* stacking bilayer graphene. The results presented are for GGA-PBE, vdW-DF revPBE, vdW-DF C09_x and vdW-DF2 C09_x functionals.

Index	AB stacking				AA stacking				
	GGA-PBE	vdW-DF	revPBE	vdW-DF2 C09 _x	Pristine	GGA-PBE	vdW-DF	revPBE	vdW-DF2 C09 _x
Pristine	4.36	3.61	3.25	3.32	Pristine	4.51	3.76	3.51	3.57
<i>c</i> ₁ (<i>AB</i>)	4.30	3.58	3.21	3.26	<i>c</i> ₁ (<i>AA</i>)	4.29	3.64	3.32	3.37
<i>c</i> ₂ (<i>AB</i>)	3.65	3.67	3.48	3.50	<i>c</i> ₂ (<i>AA</i>)	3.49	3.53	3.32	3.34
<i>c</i> ₃ (<i>AB</i>)	4.29	3.55	3.21	3.26	<i>c</i> ₃ (<i>AA</i>)	4.24	3.58	3.25	3.29
<i>c</i> ₄ (<i>AB</i>)	4.20	3.52	3.16	3.20	<i>c</i> ₄ (<i>AA</i>)	3.69	3.45	3.05	3.08
<i>c</i> ₅ (<i>AB</i>)	4.21	3.52	3.16	3.20	<i>c</i> ₅ (<i>AA</i>)	3.74	3.42	3.04	3.11
<i>c</i> ₆ (<i>AB</i>)	3.67	3.67	3.42	3.46	<i>c</i> ₆ (<i>AA</i>)	3.38	3.40	3.19	3.22
<i>c</i> ₇ (<i>AB</i>)	3.66	3.67	3.44	3.47	<i>c</i> ₇ (<i>AA</i>)	3.40	3.43	3.22	3.24
<i>c</i> ₈ (<i>AB</i>)	3.65	3.66	3.44	3.47	<i>c</i> ₈ (<i>AA</i>)	3.29	3.30	3.16	3.19
<i>c</i> ₉ (<i>AB</i>)	3.61	3.63	3.40	3.43	<i>c</i> ₉ (<i>AA</i>)	6.46	6.42	6.27	6.27
<i>c</i> ₁₀ (<i>AB</i>)	3.29	3.31	3.18	3.19					
<i>c</i> ₁₁ (<i>AB</i>)	3.50	3.53	3.42	3.44					
<i>c</i> ₁₂ (<i>AB</i>)	3.51	3.50	3.43	3.44					

distance (calculated as the difference between the lithiated and pristine bilayer interlayer separations) for all the Li configurations considered. It is seen that for configurations $c_{1(AB)}$, $c_{3(AB)}$, $c_{4(AB)}$, $c_{5(AB)}$, $c_{1(AA)}$, $c_{3(AA)}$, $c_{4(AA)}$, and $c_{5(AA)}$, the relative interlayer distance is very small and negative. This indicates that when the Li atoms are adsorbed outside the layers, a slight reduction in the interlayer separation occurs, and therefore the van der Waals forces are only marginally distorted.



(a)



(b)

FIG. 4. The variation of the relative interlayer distances calculated with respect to Li configurations predicted by all the functionals (calculated as the difference between the lithiated and pristine bilayer interlayer separations) for (a) AB and (b) AA stacking.

We see in Fig. 4 that for configurations $c_{2(AB)}$, $c_{6(AB)}$, $c_{7(AB)}$, $c_{8(AB)}$, $c_{9(AB)}$, $c_{11(AB)}$ and $c_{12(AB)}$, GGA-PBE predicts that the layers move close to each other during intercalation, whereas the vdW-DF revPBE, vdW-DF C09_x and vdW-DF2 C09_x functionals predict that the layers move slightly apart from each other. It was

also observed in Table II that in these seven configurations, GGA-PBE and vdW-DF revPBE functionals give approximately the same interlayer distance. When the Li atoms are intercalated, the van der Waals bonding gets greatly distorted and becomes overshadowed by the ionic bonding between the Li atoms on the one hand and the cloud of π -electrons on the carbon layers on the other. Since the nature of the bonding in these configurations is no longer simply van der Waals but Li-induced ionic bonding, the agreement between GGA-PBE and vdW-DF revPBE is not unexpected.

The relative interlayer distance for $c_{10(AB)}$ deviates from that for $c_{2(AB)}$, $c_{6(AB)}$, $c_{7(AB)}$, $c_{8(AB)}$, $c_{9(AB)}$, $c_{11(AB)}$ and $c_{12(AB)}$ due to the structural translation from AB to AA stacking in configuration $c_{10(AB)}$. It is shown in Fig. 3 that configuration $c_{10(AB)}$ has the same configuration as $c_{8(AA)}$ after relaxation. All functionals predict that $c_{10(AB)}$ has the same interlayer spacing as $c_{8(AA)}$ after relaxation. This structure is also predicted to be the most energetically favourable for all functionals considered. We therefore conclude that Li favours the AA stacking, and that $c_{8(AA)}$ represents a feasible template for experimentally synthesizing and characterizing a Li-based anode material.

As presented in Table II, vdW-DF revPBE gives larger interlayer separations compared to the other two van der Waals corrected functionals. This large separation originates from the repulsive nature of the revPBE exchange term.⁶⁰ Such an overestimation was previously observed in many systems, and several methods^{46,61–63} were subsequently developed to address these shortcomings. Cooper⁴⁶ proposed a new exchange term (C09_x) that showed a noticeable improvement in predicting the bonding for a wide range of systems that have short and long range interactions. Not surprising for C09_x, for the graphite, the interlayer spacing is within 2% of the experimental value.

Table III lists the equilibrium distances between Li and graphene (Li-h) measured at the hollow site for all the Li configurations using the different forms of exchange correlation functionals. The letters O and I in Table III indicate whether the distance Li-h is measured outside or within the bilayer respectively. Our calculated values agree well with the results obtained from others^{34–36,64} who studied Li atoms on graphite and graphene using the GGA-PBE and LDA functionals. We see in Table III that the intercalated Li atoms slightly overbind within the layers compared to the ones that are adsorbed outside the layers. The intercalated Li atoms relax to the middle of the layers in AA stacking since the value for Li-h measured at position I is almost twice the interlayer distance. This is not the case for AB stacking since the Li atom faces a hollow site on the top layer and an on-top site on the bottom layer. We therefore expect the distances not to be the same.

TABLE III. The equilibrium distance between Li and the hollow site (Li-h in Å) for lithiated AB and AA stacking sequences. The letters O and I stand for the distance Li-h measured outside and within the bilayer graphene, respectively.

Stacking Index	GGA-PBE		vdW-DF		revPBE		vdW-DF C09		vdW-DF2 C09	
	O	I	O	I	O	I	O	I	O	I
<i>AB</i>	$c_{1(AB)}$	1.74	1.75	1.69	1.74	1.69	1.74	1.67	1.74	1.67
	$c_{2(AB)}$		1.65	1.77	1.76		1.76		1.76	
	$c_{3(AB)}$	1.79		1.76		1.74		1.74	1.74	
	$c_{4(AB)}$	1.75		1.76		1.74		1.74	1.74	
	$c_{5(AB)}$	1.75		1.76		1.74		1.74	1.74	
	$c_{6(AB)}$	1.78	1.68	1.74	1.69	1.74	1.68	1.74	1.74	1.69
	$c_{7(AB)}$	1.78	1.68	1.75	1.69	1.74	1.68	1.75	1.75	1.68
	$c_{8(AB)}$	1.73	1.67	1.74	1.69	1.78	1.66	1.76	1.76	1.70
	$c_{9(AB)}$	1.74	1.68	1.74	1.68	1.76	1.66	1.75	1.75	1.68
	$c_{10(AB)}$		1.63		1.67		1.60		1.61	
	$c_{11(AB)}$		1.65		1.66		1.67		1.67	
	$c_{12(AB)}$		1.65		1.65		1.68		1.68	
<i>AA</i>	$c_{1(AA)}$	1.74	1.75	1.77	1.75	1.66	1.74	1.67	1.74	1.67
	$c_{2(AA)}$		1.74	1.75		1.74		1.74		1.67
	$c_{3(AA)}$	1.74		1.75		1.74		1.74	1.74	
	$c_{4(AA)}$	1.73				1.74		1.74	1.74	
	$c_{5(AA)}$	1.74		1.75		1.74		1.75	1.75	
	$c_{6(AA)}$	1.74	1.71	1.75	1.73	1.74	1.62	1.75	1.75	1.59
	$c_{7(AA)}$	1.73	1.70	1.74	1.70	1.74	1.61	1.74	1.74	1.63
	$c_{8(AA)}$		1.63		1.67		1.59		1.60	
	$c_{9(AA)}$		1.67		1.64		1.64		1.65	

C. Electronic properties

To examine the influence of Li on the electronic properties of bilayer graphene, the total density of states (TDOS) plots is presented in Fig. 5. Since it is known that Li alters the graphene structure from semimetallic to pure metallic, there is no need to present DOS plots for all identified configurations. Fig. 5 depicts the vdW-DF2 C09_x TDOS of the most stable configurations c_2 and c_{10} for the ordered structures $\beta\alpha\beta$ and $\beta\alpha\alpha\beta$ from both stackings respectively. We note that the Dirac point for these configurations shifts into the valence states. This occurs²⁶ when the localized electron from the Li atom becomes delocalized on the graphene bonding network, resulting in the partial filling of π^* unoccupied orbitals.

The Dirac shift was found to be 1.38 eV (GGA-PBE), 1.52 eV (vdW-DF revPBE), 1.50 eV (vdW-DF C09_x) and 1.49 eV (vdW-DF2 C09_x) for $c_{2(AB)}$, and 1.37 eV (GGA-PBE), 1.55 eV (vdW-DF revPBE), 1.59 eV (vdW-DF C09_x) and 1.59 eV (vdW-DF2 C09_x) for $c_{2(AA)}$. The GGA-PBE value is in good agreement with the experimental value of 1.40 eV obtained by Sugawara *et al.*³⁰ but greater than the value of 1.25 eV obtained by Watcharinyanon *et al.*³¹ The results show that the vdW corrected functionals overestimate the experimental Dirac shift of configuration c_2 .

In the case of two Li bonded adatoms, the Dirac shift was found to be 1.65 eV (GGA-PBE), 1.71 eV (vdW-DF revPBE), 1.83 (vdW-DF C09_x) and 1.85 eV (vdW-DF2 C09_x) for fully relaxed $c_{10(AB)}$ and $c_{8(AA)}$. The Dirac shift is greater in c_{10} compared to c_2 . This is attributed to the addition of an extra valence electron into the system from the second Li atom. The first van Hove singularity appears exactly in the vicinity of the Fermi level for the $c_{10(AB)}$ and $c_{8(AA)}$ as shown in Fig. 5.

To quantify the interaction between the ionized Li atom and the cloud of π electrons in the graphene bonding network, the charge transfer (q) and workfunction (Φ) are calculated. We extract the charge transfer by manipulating the total density of states plots. This is the same technique used by Chan *et al.*³⁶ in their study of metal atom adsorption on graphene and by Titantah *et al.*⁶⁵ in their study of Li-intercalated graphite. The method is based on the integration of the pristine bilayer graphene TDOS plots from E_{Dirac} to $E_{Dirac} + \Delta E_{Fermi}$. It is known that the interaction between the adatom and the substrate alters the Fermi level; therefore the amount of charge transfer depends on the Fermi level shift ΔE_{Fermi} which is calculated by:

$$\Delta E_{Fermi} = E_{Fermi} - E_{Dirac}, \quad (1)$$

where E_{Dirac} and E_{Fermi} are obtained from the lithiated bilayer total density of states.

Table IV summarizes the charge transfer for configurations c_2 and c_{10} as predicted by the GGA-PBE, vdW-DF revPBE, vdW-DF C09_x and vdW-DF2 C09_x functionals. In agreement with previous studies,^{36,65} the charge transfer is positive, which indicates a flow of electronic charge

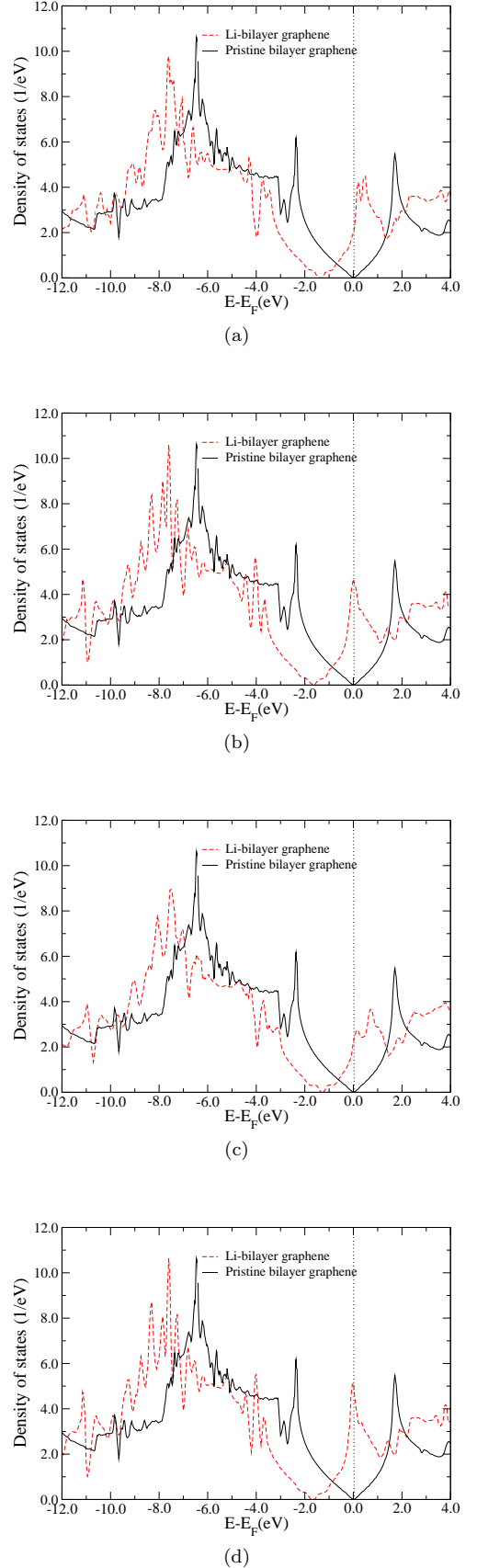


FIG. 5. The total densities of states for the most stable Li configurations on AA and AB stacking bilayer graphene: (a) $c_{2(AB)}$, (b) $c_{10(AB)}$, (c) $c_{2(AA)}$ and (d) $c_{10(AA)}$. The Fermi level is marked by the dotted line.

from the Li atoms to the substrate. In configuration c_2 , it is noted that about 0.92 e of charge flows from the Li atom to bilayer graphene, which suggests strong ionic bonding between the Li atom and the substrate. Recently, Valencia *et al.*⁶⁴ used the Bader charge analysis to obtain 1.00 e (LSDA) and 0.89 e (GGA-PBE) in the study of Li-intercalated graphite.

In the case of two Li bonded adatoms in configurations $c_{10(AB)}$ and $c_{8(AA)}$, we found that only a fraction of about 0.3 e charge flows from the Li to bilayer graphene. This suggests that the majority of the electronic charge distribution is located in the Li-Li covalent bond that is formed (Table IV). We therefore conclude that the intercalated Li dimer weakly interacts with the graphene layers compared to the intercalated isolated Li atom.

The workfunction is calculated by:

$$\Phi = E_{vacuum} - E_{Fermi}, \quad (2)$$

where the vacuum energy (E_{vacuum}) is obtained by calculating the macroscopic average of the electrostatic potential along the z-direction. In our case, we calculated E_{vacuum} about 50 Å away from the structure. Our calculated workfunctions for pristine AA and AB stacked bilayer graphene are presented in Table IV. Our GGA-PBE results are in good agreement with previously calculated values of 4.26 eV (GGA-PBE) for pristine single layer graphene but lower than the experimental value of 4.65 eV obtained by Yu *et al.*⁶⁶ and the graphite experimental value of 4.60 eV obtained by Takahashi *et al.*⁶⁷ There are no existing results obtained with van der Waals corrected functionals to compare our results with.

It is seen in Table IV that GGA-PBE gives the lowest values for Φ whereas vdW-DF C09_x gives the highest value for pristine bilayer graphene structures. The vdW-DF C09_x and GGA-PBE values for both stackings are 4.95% and 8.80% within the experimental value reported by Yu *et al.*⁶⁶ respectively. Murata *et al.*⁶⁸ obtained values of about 4.42 eV from LEED patterns considering different orientations of the graphene layers. It has already been discussed that the vdW-DF C09_x gives shorter interlayer distances than GGA-PBE and agrees very well with the experimental value. Based on this, we conclude that the better agreement of the calculated workfunction using the vdW-DF C09_x with the experiment is due to the interlayer distance. Therefore, the workfunction is clearly affected by the strength of electronic coupling between the layers.

We see in Table IV that the intercalation of the Li atoms results in a decrease in the workfunction compared to pristine bilayer graphene. Our GGA-PBE value for c_2 is slightly larger than the value of 2.79 eV obtained by Chan *et al.*³⁶ in their studies of the adsorption of a single Li atom on single layer graphene. Configuration c_{10} has a workfunction which is 0.36 eV (GGA-PBE), 0.26 eV (vdW-DF revPBE), 0.40 eV (vdW-DF C09_x), 0.43 eV (vdW-DF C09_x) larger than that of c_2 . This indicates that it is easier to remove an electron from configuration c_2 than from c_{10} . Electronic charge is readily ionized from the Li atom in c_2 , which results in the small value of Φ while in c_{10} more energy is needed to break the Li-Li covalent bond first to isolate the electrons before moving an electron to the vacuum level.

TABLE IV. The calculated amount of charge transfer q (e) and work function Φ (eV) for the most energetically stable Li configurations obtained from AB and AA stacking sequences. The results presented are for all the exchange correlation functionals used.

Stacking structure		GGA-PBE vdW-DF		revPBE vdW-DF		C09 vdW-DF		C09 vdW-DF2		C09	
	q	Φ	q	Φ	q	Φ	q	Φ	q	Φ	
AB	Pristine	4.24	4.31	4.42	4.41						
	$c_{2(AB)}$	0.94	2.98	0.91	3.16	0.92	3.13	0.93	3.12		
	$c_{10(AB)}$	0.32	3.34	0.33	3.42	0.31	3.53	0.29	3.55		
AA	Pristine	4.25	4.35	4.42	4.41						
	$c_{2(AA)}$	0.94	3.00	0.94	3.21	0.92	3.22	0.96	3.23		
	$c_{8(AA)}$	0.30	3.35	0.33	3.42	0.31	3.53	0.31	3.54		

IV. CONCLUSIONS

In summary, we have systematically investigated the possible configurations of two Li adatoms on the *AA* and *AB* stacking sequences of bilayer graphene using density functional methods. Employing different forms of exchange correlation functionals that correctly describe the interlayer interaction within the bilayer graphene, the relative stabilities, structural and electronic properties of the identified configurations were explored. For all configurations considered, we record a variation in formation energies predicted by these functionals. The vdW-DF revPBE consistently predicts the highest formation energies, while vdW-DF C09_x consistently gives the lowest. One of the Li-configurations ($c_{10(AB)}$) undergoes spontaneous translation from *AB* to *AA* stacking, and is found to be the most energetically stable configuration compared to the other configurations. It is found that the change in interlayer distance caused by Li intercalation greatly depends on the exchange correlation functional used: the GGA-PBE shows a reduction while the van der Waals corrected exchange correlation functionals show an expansion in the interlayer distance. In the case of Li intercalated configurations, GGA gives nearly the same interlayer distances as vdW-DF revPBE, unlike in the pristine structures. We suggest that since Li induced ionic bonding between the layers is considered to be dominant, both vdW-DF revPBE and GGA-PBE are treated locally. In order to avoid double counting, the corrected non-local correlation term in vdW-DF revPBE vanishes (because the non-local correlation part is treated within

full potential approximation (FPA))⁴⁵ because the Li induced ionic bonding between the layers is considered to be dominant. It is found that the inclusion of the C09_x exchange term in vdW-DF predicts shorter interlayer distances both in pristine and lithiated structures than the revPBE exchange term in the vdW-DF functional. Even if it is known that the construction of these van der Waals corrected exchange correlation functionals is basically in terms of the energetics (stability) and structural properties, our calculated workfunction for pristine bilayer graphene using the C09_x terms agrees very well with the experimental value compared to GGA-PBE.

In general, this article specifically describes the electronic interactions between the Li atoms and graphene layers, where the effects of van der Waals forces are not neglected in our quantum mechanical model DFT. To accurately describe the bonding that occurs in bilayer graphene, we use the van der Waals corrected exchange correlation functionals on the basis of quantum mechanical theory. Various review papers such as Refs^{69–72} reveal coulomb aspects that still require thorough investigations. Another challenging but interesting topic arises from Ref⁷², on methodological development.

ACKNOWLEDGMENTS

The authors would like to thank the University of Pretoria, the National Research Foundation (NRF) and the National Institute for Theoretical Physics (NITheP) for support. We are grateful to the Center for High Performance Computing (CHPC) for the use of excellent computing resources.

* edwin.mapasha@up.ac.za

- ¹ K. S. Novoselov, A. K. Geim, S. V. Morozov, D. Jiang, Y. Zhang, S. V. Dubonos, I. V. Grigorieva, and A. A. Firsov, *Science* **306**, 666 (2004).
- ² A. K. Geim and K. S. Novoselov, *Nature Mater.* **6**, 183 (2007).
- ³ P. R. Wallace, *Phys. Rev.* **71**, 622 (1947).
- ⁴ K. S. Novoselov, A. K. Geim, S. V. Morozov, D. Jiang, Y. Zhang, M. I. Katsnelson, S. V. Dubonos, I. V. Grigorieva, and A. A. Firsov, *Nature (London)* **438**, 197 (2005).
- ⁵ K. S. Novoselov, Z. Jiang, Y. Zhang, S. V. Morozov, H. L. Stormer, U. Zeitler, J. C. Maan, G. S. Boebinger, P. Kim, and A. K. Geim, *Science* **315**, 1379 (2007).
- ⁶ Y. Zhang, Y. W. Tan, H. L. Stormer, and P. Kim, *Nature (London)* **438**, 201 (2005).
- ⁷ A. H. Castro, F. Guinea, N. M. R. Peres, K. S. Novoselov, and A. K. Geim, *Rev. Mod. Phys.* **81**, 109 (2009).
- ⁸ F. Schedin, A. K. Geim, S. V. Morozov, E. W. Hill, P. Blake, M. I. Katsnelson, and K. S. Novoselov, *Nature Mater.* **6**, 652 (2007).
- ⁹ X. Li, X. Wang, L. Zang, S. Lee, and H. Dai, *Science* **319**, 1229 (2008).
- ¹⁰ X. Wang, L. Zhi, and K. Mullen, *Nano. Lett.* **8**, 323 (2008).
- ¹¹ S. Gilje, S. Han, M. Wang, K. L. Wang, and R. B. Kaner, *Nano. Lett.* **7**, 3394 (2007).

- ¹² M. S. Dresselhaus, G. Dresselhaus, *Adv. Phys.* **51**, 1 (2002).
- ¹³ P. V. C. Medeiros, F. de Brito Mota, A. J. S. Mascarenhas, C. M. C. de Castilho, *Nanotechnology.* **21**, 115701 (2010).
- ¹⁴ C. K. Yang, *Appl. Phys. Lett.* **94**, 163115 (2009).
- ¹⁵ X. Wang, *Appl. Phys. Lett.* **95**, 183103 (2009).
- ¹⁶ K. Persson, Y. Hinuma, Y. S. Men, A. V. Van der Ven, G. Ceder, *Phys. Rev. B* **82**, 125416 (2010).
- ¹⁷ T. Piao, S. M. Park, C. H. Doh, S. I. Moon, *J. Electrochem. Soc.* **146**, 2794 (1999).
- ¹⁸ M. Noel, V. Suryanarayanan, *J. Power Sources* **111**, 193 (2002).
- ¹⁹ <http://www.gizmag.com/graphene-paper-battery-anodes/23881/> (20/11/2012).
- ²⁰ D.Y. Pan, S. Wang, B. Zhao, M.H. Wu, H.J. Zhang, Y. Wang, Z. Jiao, *Chem. Mater.* **21** (2009).
- ²¹ T. Wei, F. Wang, J. Yan, J. Cheng, Z. Fan, H. Song, *J. Electroanal. Chem.* **653** (2011).
- ²² E. Pollak, B. Geng, K. J. Jeon, I. T. Lucas, T. J. Richardson, F. Wang, R. Kostecki, *Nano. Lett.* **10**, (2010).
- ²³ J. Antony, and S. Grimme, *Phys. Chem. Chem. Phys.* **8**, 5287 (2006).
- ²⁴ Y. Zhang, X. L. Lu, Y. Jiang, B. Teng, J. Q. Lu, *J. Comput. Theor. Nanosci.* **8**, (2011).
- ²⁵ S. P. Wang, J. G. Guo, Y. Jiang, *J. Comput. Theor.*

- Nanosci. **10**, 1 (2013).
- ²⁶ K. R. Kganyago, and P. E. Ngoepe, Phys. Rev. B **68**, 205111 (2003).
- ²⁷ J. J. Zhou, W. W. Zhou, C. M. Guan, J.Q. Shen, C. Y. Ouyang, M. S. Lei, S.Q. Shi and W.H. Tang, Sci. China-Phys. Mech. Astron. **55**, 8 (2012).
- ²⁸ P. A Denis, J. Phys. Chem. C **115**, 27 (2011).
- ²⁹ T. P. Kaloni, Y. C. Cheng, M. Upadhyay Kahaly, U. Schwingenschogl, Chem. Phys. Lett. **534**, (2012).
- ³⁰ K. Sugawara, K. Kanetani, T. Sato, and T. Takahashi, AIP. Adv. **1**, 022103 (2011).
- ³¹ S. Watcharinyanon, L. I. Johansson, A. A. Zakharov, and C. Virojanadara, Surf. Sci. **606**,3 (2012).
- ³² C. Virojanadara, S. Watcharinyanon, A. A. Zakharov, and L. I. Johansson, Phys. Rev. B **82**, 205402 (2010).
- ³³ M. Khantha, N. A. Cordero, L. M. Molina, J. A. Alonso, and L. A. Girifalco, Phys. Rev. B **70**, 125422 (2004).
- ³⁴ R. E. Mapasha, and N. Chetty, Comput. Mat. Sci. **49**, (2010).
- ³⁵ A. M. Garay-Tapia, A. H. Romero, and V. Barone, J. Chem. Theory Comput. **8**, (2012).
- ³⁶ K. T. Chan, J. B. Neaton, M. L. Cohen, Phys. Rev. B **77**, 235430 (2008).
- ³⁷ Y. Imai, and A. Watanabe, J. Alloys Compd. **439**, (2007).
- ³⁸ S. Grimme, Comput. Mol. Sci, J. Alloys Compd. **1**, 211 (2011).
- ³⁹ A. Tkatchenko, L. Romaner, O. T. Hofmann, E. Zojer, C. Ambrosch-Draxl, M. Scheffler, MRS Bull, **35**,435 (2010).
- ⁴⁰ E. R. Johnson, I. D. Mackie, and G. A. DiLabio, J. Phys. Org. Chem **22**,1127 (2009).
- ⁴¹ L. A. Burns, A. Vazquez-Mayagoitia, B. G. Sumpter, D. C. Sherrill, J. Phys. Chem **134**, 084107 (2011).
- ⁴² T. Ono, Y. Fujimoto, S. Tsukamoto, Quantum Matter **1**, 4 (2012).
- ⁴³ B. Tuzun, C. Erkok, Quantum Matter. **1**, 136 (2012).
- ⁴⁴ M. Narayanan, A. J. Peter, Quantum Matter **1**, 153 (2012).
- ⁴⁵ M. Dion, H. Rydberg, E. Schroder, D. C. Langreth, and B. I. Lundqvist, Phys. Rev. Lett. **92**, 246401 (2004).
- ⁴⁶ V. R. Cooper, Phys. Rev. B **81**, 161104 (2010).
- ⁴⁷ J. Klimes, D. R. Bowler, and A. Michaelides, J. Phys. Condens. Matter **22**, 022201 (2010).
- ⁴⁸ J. P. Perdew, K. Burke, and M. Ernzerhof, Phys. Rev. Lett. **77**, 3865 (1996).
- ⁴⁹ P. Giannozzi, S. Baroni, N. Bonini, M. Calandra, R. Car, C. Cavazzoni, D. Ceresoli, G. L. Chiarotti, M. Cococcioni, I. Dabo, A. Dal Corso, S. Fabris, G. Gougoussis, A. Kokalj, M. Lazzeri, L. Martin-Samos, N. Marzari, F. Mauri, R. Mazzarello, S. Paolini, A. Pasquarello, L. Paulatto, C. Sbraccia, S. Scandolo, G. Sciauzero, A. P. Seitsonen, A. Smogunov, P. Umari, and R. M. Wentzcovitch, J. Phys. Condens. Matter **21**, 395502 (2009).
- ⁵⁰ G. Roman-Perez and J. M. Soler, Phys. Rev. Lett. **103**, 096102 (2009).
- ⁵¹ P. E. Blochl, Phys. Rev. B **50**, 17953 (1994).
- ⁵² H. J. Monkhorst and J. D. Pack, Phys. Rev. B **13**, 5188 (1976).
- ⁵³ P. L. de Andres, R. Ramirez, and J. A. Verges, Phys. Rev. B **77**, 045403 (2008).
- ⁵⁴ R. E. Mapasha, A.M. Ukpong, and N. Chetty, Phys. Rev. B **85**, 205402 (2012).
- ⁵⁵ A. C. Ferrari, J. C. Meyer, V. Scardaci, C. Casiraghi, M. Lazzeri, F. Mauri, S. Piscanec, D. Jiang, K. S. Novoselov, S. Roth, A. and K. Geim, Phys. Rev. Lett. **97**, 187401 (2006).
- ⁵⁶ S. Horiuchi, T. Gotou, M. Fujiwara, R. Sotoaka, M. Hirata, T. Asaka, T. Yokosawa, Y. Matsui, K. Watanabe, and M. Sekita, Jpn. J. Appl. Phys. **42**, (2003).
- ⁵⁷ Z. Liu, K. Suenaga, P. J. F. Harris, and P. J. F. Iijima, Phys. Rev. Lett. **102**, 015501 (2009).
- ⁵⁸ I. Hamada and M. Otani, Phys. Rev. B **82**, 153412 (2010).
- ⁵⁹ T. Ohta, A. Bostwick, T. Seyller, K. Horn, and E. Rotenberg, Science **313**, 951 (2006).
- ⁶⁰ Y. Zhang, and W. Yang, Phys. Rev. Lett. **80**, 890 (1998).
- ⁶¹ A. Puzder, M. Dion, and D. C. Langreth, J. Chem. Phys. **124**, 164105 (2006).
- ⁶² O. A. Vydrov, Q. Wu, and T. van Voorhis, J. Chem. Phys. **129**, 014106 (2008).
- ⁶³ F. O. Kannemann and A. D. Becke, J. Chem. Theory Comput. **5**, 719 (2009).
- ⁶⁴ F. Valencia, A. O. Romero, F. Ancilotto, and P. L. Silvestrelli, J. Phys. Chem. B **110**, (2006).
- ⁶⁵ J. T. Titantah, D.Lamoen, M. Schowalter, A. Rosenauer, Carbon **47**, (2009).
- ⁶⁶ Y. J. Yu, Y. Zhao, S. Ryu, L. E. Brus, K. S. Kim, P. Kim, Nano Lett. **9**, 10 2009 Phys. Rev. B **85**, 205443 (2012).
- ⁶⁷ T. Takahashi, H. Tokailin, T. Sagawa, Phys. Rev. B **32**, 12 (1985).
- ⁶⁸ Y. Murata, S. Nie, A. Ebnonnasir, E. Starodub, B. B. Kappes, K. F. McCarty, C. V. Ciobanu and S. Kodambaka, Phys. Rev. B **85**, 205443 (2012).
- ⁶⁹ A Herman, Rev. Theor. Sci **1**, 3-33 (2013).
- ⁷⁰ E. L. Pankratov and E. A. Bulaeva, Rev. Theor. Sci. **1**, 58-82 (2013).
- ⁷¹ Q. Zhao, Rev. Theor. Sci. **1**, 83-101 (2013).
- ⁷² A. Khrennikov, Rev. Theor. Sci. **1**, 34-57 (2013).

Chapter 7

Summary and general conclusions

Conclusions for each specific theoretical result are provided at the end of every chapter. In this chapter a summary and general concluding remarks on the overall results are presented.

The study involved first principles DFT investigations of pristine, hydrogenated and lithiated bilayer graphene material systems. Previous DFT investigations of these materials have to date, not intensely included the effects of the vdW forces. The data reported in this thesis was calculated using exchange-correlation functionals that take these effects into account. For hydrogenated materials, the study was motivated by the contradictory literature results for the electronic properties, wherein some revealed that hydrogenated bilayer graphene exhibits metallic, whereas others reported insulating behaviour. Therefore, we carried out extensive calculations to address these discrepancies.

We were interested in finding all the possible configurations at 50% and 100% coverage on a 1×1 cell. The aim was to identify and predict the lowest energy competing configurations that may exist at 50% and 100% hydrogenation coverage, based on the formation energies calculated using the newly developed four variants of the non-local van der Waals density functionals (vdW-DF, vdW-DF2, vdW-DF C09_x and vdW-DF2

C09_x). We compared these energies with GGA PBE and LDA. The obtained results give an extensive set of data, which could be referenced in future studies.

7.1 Test of exchange-correlation functionals on bulk bilayer graphene and graphite

The test of these exchange-correlation functionals on pristine bulk bilayer graphene and graphite was conducted by calculating the structural properties and binding energies. As expected, it was found that GGA PBE gives relatively meaningless values for these structures. The interlayer spacings predicted by LDA were found to be in good agreement with the experimental data for both graphite and bilayer graphene. However, the calculated LDA interlayer binding energy for graphite is nearly half the experimental value. It is clear that the standard DFT exchange-correlation functionals are not able to accurately describe all the properties for structures that are bound together by van der Waals forces.

We also tested the four variants of the non-local van der Waals density functionals on the structural properties of graphite and bilayer graphene. Using the first proposed non-local van der Waals density functional (vdW-DF), a significant improvement on the description of graphite and bilayer graphene was established as compared to GGA PBE. In agreement with the previous studies, it was found that this functional drastically overestimates the interlayer separation. It was suggested that this could be attributed to the use of the revPBE exchange term which is repulsive in nature. The use of the Cooper exchange functional (C09_x), i.e vdW-DF C09_x and vdW-DF2 C09_x, predicted the interlayer separation values to within $\pm 3\%$ of the experimental data. These findings verified C09_x as a suitable exchange functional for graphitic material systems.

7.2 Hydrogen adatoms on bilayer graphene at 50% coverage

For 50% hydrogen coverage, a total of 24 non-unique configurations were identified for cases where two H atoms are adsorbed at on-top sites on two different carbon atoms in a 1×1 unit cell. After correcting for double counting, only 16 unique configurations were found in the unrelaxed state. By means of formation energy analysis, we identified six energetically favourable configurations. We found that some configurations are energetically equivalent after relaxation in spite of the uniqueness of their initial unrelaxed states. For instance, three distinct cases are identified for formation of molecular H after relaxation. We suggested that dimer formation indicates that structures are energetically unstable (unfavourable) in their unrelaxed states. The dimer formed above the coupled bilayer in configuration c_1 , and within the interlayer region in configurations c_{12} , c_{14} and c_{15} . In both configurations c_{12} and c_{14} , the dimer is oriented horizontally and they are energetically equivalent. On the other hand, the dimer in configuration c_{15} is oriented vertically and is not energetically equivalent, compared to configurations c_{12} and c_{14} . It was noted that the dimer formation within the interlayer region in configurations c_{12} , c_{14} and c_{15} decouples the layers by doubling the interlayer separation, thereby breaking the symmetry of bilayer graphene along the z -axis. We therefore suggest H_2 intercalation as a means of exfoliating graphene layers. A comparison of the functionals on the description of these structures (c_{12} , c_{14} and c_{15}), showed a variation of the interlayer distance with decreasing order from GGA PBE \rightarrow vdW-DF revPBE \rightarrow vdW-DF2 revPBE \rightarrow vdW-DF C09_x \rightarrow vdW-DF2 C09_x \rightarrow LDA.

The results have demonstrated that configuration c_1 still preserves the two dimensional hexagonal symmetry, and we concluded that the formation of a H dimer above the bilayer does not have a significant effect on the van der Waals forces holding the layers together. Our LDA calculation gives a small positive formation energy in config-

uration c_1 , whereas vdW-DF, vdW-DF2, vdW-DF C09_x and vdW-DF2 C09_x predict negative values. We suggested that the low formation energies from these newly developed four variants of the non-local van der Waals density functionals vdW-DF for c_1 reveal that the binding force between the molecular H and the bilayer graphene arises from van der Waals interaction because the H₂ dimer is physisorbed above the top layer.

The results have indicated that configurations c_2 , c_7 and c_8 , retain the coupled bilayer structure in the relaxed state and are low-energy competing structures at 0 K. It is noted that apart from configuration c_1 , this spontaneous formation only occurs when the top layer of carbon atoms is fully saturated, leaving the bottom layer completely unhydrogenated (c_2 and c_7), or when both top and bottom layers are partially hydrogenated in c_8 . Configuration c_8 has been shown to undergo a hydrogen-induced phase transformation from hexagonal to tetrahedral geometry with a reduction in interlayer separation from 3.29 Å (vdW-DF2C09_x) to 1.56 Å (vdW-DF2C09_x). It was found that both external faces of bilayer graphene have to be exposed to H for the transformation to occur because graphene is hard to penetrate. In configuration c_8 , vdW-DF and vdW-DF2 gave the highest formation energies, whereas vdW-DF C09_x and vdW-DF2 C09_x predicted the lowest. The variation of these functionals is attributed to the use of the repulsive revPBE exchange in vdW-DF and vdW-DF2, and the attractive C09_x exchange in vdW-DF C09_x and vdW-DF2 C09_x.

These low-energy competing configurations (c_2 and c_7) exhibited semimetallic behaviour except for configuration c_8 , where a wide direct energy gap is observed. Although DFT functionals are known to incorrectly predict the band gap, it is important to determine the variation of the newly developed four variants of the non-local van der Waals density functionals. The calculated band gap in configuration c_8 is found to be 2.80 eV (vdW-DF), 2.61 eV (vdW-DF2), 2.91 eV (vdW-DF C09_x), 2.90 eV (vdW-DF2 C09_x), 2.89 eV (LDA), and 3.09 eV (GGA PBE), respectively. We therefore conclude

that the use of the Cooper exchange functional (C09_x) in vdW-DF and vdW-DF2 has a very minimal influence on the band gap of configuration c_8 . It can be argued that vdW interaction is not significant in configuration c_8 because of the formation of strong interlayer carbon bonds. Finally, we conclude that configuration c_8 represents a viable template for synthesizing nanodiamonds from graphene by hydrogenation.

7.3 Van der Waals density-functional study of 100% hydrogen coverage on bilayer graphene

At 100% coverage, ten unique H configurations were identified from a 1×1 unit cell. After relaxation, all exchange-correlation functionals predicted nine of the structures to have negative formation energies, with the three coupled low-energy competing structures (c_7 - c_9) at 0 K. The vdW-DF C09_x functional predicted the lowest formation energies and shortest interlayer distances for all configurations considered, whereas the GGA PBE functional gave the highest formation energies and largest interlayer distances. The behaviour of these exchange-correlation functionals is attributed to the nature of exchange functionals used. In general, we noticed that in the case of a physisorbed H₂ dimer, the coupled structures are more energetically stable than the decoupled configurations. It was noted that configurations that contain the physisorbed H₂ dimer have similar properties to those identified in 50% coverage. In configuration c_1 , it was revealed that the H₂ dimers physisorbed outside the layers are furthest away from the layer as compared to the sandwiched ones. This is not surprising because both layers are attempting to reach their equilibrium separation through a typical π -involved weak interaction but are hindered by the presence of the dimer between layers, whereas outside, the dimer is free to adjust its position away from the outer layer.

The relaxed configurations c_7 - c_9 show that all the carbon atoms are hydrogenated, and the graphene layers are buckled (moved up and down out of the planes). It is con-

cluded that the stability observed in these configurations is ascribed to the H induced puckering mechanism on both layers. Mainly, this buckling occurs during the wavefunction overlap between the carbon and H atoms, resulting in all the carbon atoms having sp^3 rehybridization. All functionals predicted that configurations c_7 - c_9 are relatively wide band gap semiconductors, whereas other configurations exhibit either semimetallic or metallic character, revealing the unsaturation of the structures. The band gap values for configurations c_7 - c_9 were found to be very comparable to c_8 identified in 50% coverage since for these materials, all atoms have strong covalent tetrahedral bonding (sp^3 hybridizations).

The cell size was increased to 2×1 , which contains four atoms per plane (layer), to examine the properties of other low-energy configurations that are not possible in a 1×1 cell. The configurations identified are referred to as c_{11} - c_{16} and show physically interesting H arrangements such as chair-like (c_{11}), zigzag-like (c_{12}) and boat-like (c_{13}) conformers. Although the 1×1 unit-cell is able to present a clear picture for interaction of H and graphene, our results reveal that it limits the occurrence of other interesting physics. We noted that configuration c_{11} is the only configuration that can exist in both 2×1 and 1×1 cells. By analyzing the formation energy per atom, we deduce that c_{11} is the most energetically stable configuration in the 2×1 cell, and is almost nearly the same as that for c_7 - c_9 . Interestingly, configuration c_{11} shows uniform buckling (perfect tetrahedral bonding), unlike in c_{12} - c_{16} where greatly distorted tetrahedral bonding is realized. We concluded that the different arrangements of H atoms in these configurations are responsible for great variation in bond distances and angles. We therefore suggest that configuration c_{11} represents a viable template that can be used for H storage. When comparing the elastic properties of pristine and hydrogenated structures, results revealed that the effect of hydrogenation is to reduce the elastic values of the pristine structures. In the case of the moduli results, vdW-DF gave the smallest values, whereas the vdW-DF-C09_x predicted the largest values.

In general, it was concluded that no single exchange-correlation functional is able to describe the energetics, local structure and electronic properties of all the configurations consistently. The energetics, structural and electronic properties greatly depend on the H configuration. Some H configurations on bilayer graphene present viable templates for H storage and microelectronics applications.

7.4 Comparative investigations of lithium adatoms on AA and AB stackings of bilayer graphene : a van der Waals density functional study

We further performed a systematic investigation of the effects of lithium (Li) on *AA* and *AB* stacking sequences of bilayer graphene, using these newly developed variants of the non-local van der Waals density functionals. Two Li atoms were considered to examine the effects of the Li-Li interaction on bilayer graphene. A total of 12 unique configurations for *AB* and 9 for *AA* stackings were identified. The results have shown that the energetics and structural properties depend on the Li configuration. For instance, all exchange-correlation functionals predicted that the Li intercalation configuration has negative formation energy, whereas the Li adsorbed at the external faces of the bilayer graphene exhibited a positive value from both *AB* and *AA* stackings. The vdW-DF consistently predicts the highest formation energies, and vdW-DF2 C09_x the lowest. The unexpected observed largest formation energy in vdW-DF is mainly because the revPBE exchange is too repulsive to describe these Li induced ionic systems. Our results have demonstrated that for lithiated bilayer graphene, GGA PBE gives comparable results to the other functionals, unlike in the case of the pristine structure. One of the Li intercalated configurations undergoes a spontaneous translation from the *AB* to *AA* stacking, and is found to be the most energetically stable configuration compared to the other configurations. We therefore conclude that Li favours the *AA*

stacking. In the case of Li intercalated configurations, it was found that GGA PBE yields nearly the same interlayer distances as vdW-DF, unlike in the pristine structures. The agreement of these two functionals was explicitly discussed. We noted that the Dirac point of these Li configurations shifted from the Fermi level into the valence states. This mainly occurs when the localized electron from the Li atom becomes delocalized on the graphene bonding network, resulting in the partial filling of π^* unoccupied orbitals; hence the structure becomes metallic.

To quantify the interaction between the ionized Li atom and the cloud of π electrons in the graphene bonding network, the charge transfer (q) and workfunction (Φ) were calculated. In the case of single Li adsorption, it was noted that about $0.92 e$ of charge flows from the Li atom to bilayer graphene, which suggests strong ionic bonding between the Li atom and the substrate. In the case of the two covalently bonded Li adatoms configuration, only a fraction of about $0.3 e$ charge transfer was measured. This suggests that the majority of the electronic charge distribution is located in the Li-Li covalent bond that is formed. We therefore conclude that the intercalated Li dimer weakly interacts with the graphene layers compared to the intercalated isolated Li atom. Even if the construction of these van der Waals corrected exchange correlation functionals is based on the energetics (stability) and structural properties, our calculated workfunction for pristine bilayer graphene obtained using vdW-DF2 C09_x agrees very well with the experimental data compared to GGA-PBE. The results reveal that the effect of Li is to reduce the workfunction of the pristine structures.

In general, all the exchange-correlation functionals are comparable in the lithiated structures, unlike in the description of the pristine ones. It was also found that all the various lithium configuration structures are always metallic. The clustered Li atoms weakly interact with the graphene substrate. Unlike in hydrogenated bilayer graphene, the effects of intercalated Li strongly couple the structure. We conclude that Li prefers to be intercalated within the AA stacking, and represents a feasible template for ex-

perimentally synthesizing and characterizing a Li-based anode material.

Possible future work will involve the following: we will investigate the response of these newly developed variants of the non-local van der Waals density functionals on topologically defected bilayer graphene material systems. We lack information about the interlayer spacings and binding energies of these defected systems. The random phase approximation will also be employed in these systems and compared with these newly non-local developed functionals. Lastly we will study the effects of substitutional doping on the various properties of bilayer graphene.